LIF INSTRUMENT DEVELOPMENT, IN SITU MEASUREMENT AT SOUTH POLE AND 1D AIR-SNOWPACK MODELING OF ATMOSPHERIC NITROUS ACID (HONO)

A Dissertation
Presented to
The Academic Faculty

by

Wei Liao

In Partial Fulfillment
of the Requirements for the Degree
Doctor of Philosophy in the
School of Earth & Atmospheric Sciences

Georgia Institute of Technology
April 2008

LIF INSTRUMENT DEVELOPMENT, IN SITU MEASUREMENT AT SOUTH POLE AND 1D AIR-SNOWPACK MODELING OF ATMOSPHERIC NITROUS ACID (HONO)

Approved by:

Dr. David Tan, Advisor
School of Earth & Atmospheric Sciences
Georgia Institute of Technology

Dr. Robert Black
School of Earth & Atmospheric Sciences
Georgia Institute of Technology

Dr. Paul Wine
School of Earth & Atmospheric Sciences
Georgia Institute of Technology

Dr. Marc Stieglitz
School of Earth & Atmospheric Sciences
School of Civil and Environmental Engineering
Georgia Institute of Technology

Dr. Greg Huey
School of Earth & Atmospheric Sciences
Georgia Institute of Technology

Date Approved: [Jan 14th, 2008]

To my loving wife, Dr. Peng Liu, with whom all things are possible
To my parents for their love and support

ACKNOWLEDGEMENTS

I would like to first thank my advisor Dr. David Tan for his support, guidance, patience and encouragement for my graduate career. He gives me the most freedom in academic and in my future career to find my interests and strengths. The critical thinking skills will benefit me life long. I also would thank my committee members, Dr. Paul Wine, Dr. Greg Huey, Dr. Robert Black and Dr. Marc Stieglitz for supervising me over the years and help me through the thesis.

This thesis would not have been possible without the assistance of many individuals. I would like to acknowledge Mr. Joe Mastromarino who has the wealth of information about the laser and the expertise to tune the laser to the optimum status. I would also like to thank Ms. Arsineh Hecobian and Ms. Anne Case for their assistance. In addition, special mention should go to Dr. Jack Dibb from University of New Hemisphere, who provides me many unpublished data and constructive suggestions; Dr. Gao Chen from National Aeronautics and Space Administration (NASA), who merges the ANTCI 2003 data and provide his gas phase model results as a reference; Dr. Detlev Helmig from University of Colorado, who share me his metrology data and analysis; Dr. Julia Lee-Taylor and Dr. Sasha Madronich from National Center for Atmospheric Research (NCAR), who not only share their actinic flux model codes but also take time to explain the concept to me; Dr. Kenjiro Toyota from York University, whose AGU presentation inspires me to incorporate the windpumping model component; Dr. Tao Zeng from Georgia Institute of Technology, who patiently help me through the model building.

Lastly, I would like to extend my deepest appreciation to my parents Zhongqin Yu and Yulan Liao along with my wife Dr. Peng Liu, without whom none of this would have been possible. I deeply cherish every day we shared together.

Funds for this research were provided by the NSF foundation.

TABLE OF CONTENTS

LIST OF TABLES

LIST OF FIGURES

LIST OF ABBREVIATIONS

AAS	atomic absorption spectrometry
ANTCI	Antarctic troposphere chemistry investigation
ARO	atmospheric research observatory
BBO	beta barium borate
ECC	electrochemical concentration cell
EQ	electronic quenching
DAS	data acquisition system
DNPH	2, 4-dinitrophenylhydrazone derivatization
DOAS	differential optical absorption spectroscopy
FD	frequency doubling
FID	flame ionization detector
FTIR	Fourier transform infrared spectroscopy
GC/ECD	gas chromatography with electron capture detection
HA	humic acid
HPLC	high performance liquid chromatography
HR	high reflector
ICP-MS	inductively-coupled plasma mass spectrometry
ISCAT	investigation of sulfur chemistry in the Antarctic troposphere
LIF	laser-induced fluorescence
LOPAP	long path absorption photometer
MC/IC	mist chamber/ion chromatography
MOPO	master oscillator / power oscillator
NCAR	national center for atmospheric research
NOAA	national oceanic and atmospheric administration

PAN	peroxyacetyl nitrate
PF-LIF	photo fragmentation/laser-induced fluorescence
PMT	photomultiplier tube
SICIMS	selected ion chemical ionization mass spectrometry
TF	transmission filter
UV/VIS	Ultraviolet-visible spectroscopy
VET	vibrational energy transfer
VOCs	volatile organic compounds
OC	output coupler
OPO	optical parametric oscillator
XTL	crystal

SUMMARY

Atmospheric nitrous acid (HONO) is a significant and sometimes dominant OH source in Polar Regions. In the polar atmosphere, measurements of HONO are an important part of understanding the dynamics of snow-air chemistry and atmospheric photochemistry. The low levels of HONO present in such regions necessitate the development of instrumentation with low detection limits. An improved method of detecting HONO is developed using photo-fragmentation and laser-induced fluorescence. The detection limit of this method is 2-3 pptv for ten-minute integration time with 35% uncertainty.

The ANTCI 2003 measurements confirm the high N oxides observed previously in ISCAT 1998 and 2000. The median LIF observed mixing ratio of HONO 10m above the snow was 5.8 pptv (mean value 6.3 pptv) with a maximum of 18.2pptv on Nov 30th, Dec 1st, 3rd, 15th, 17th, 21st, 22nd, 25th, 27th and 28th. The LIF HONO observations are compared to concurrent HONO observations performed by mist chamber/ion chromatography (MC/IC). Both the LIF and MC/IC techniques observed enhanced HONO; however, the MC/IC observations were higher than the LIF observations by a factor of 7.2±2.3 in the median. It is suggested that the MC/IC technique might suffer from interference from HNO_4. As in ISCAT 2000, the abundance of both HONO measurements exceeds the pure gas phase model predictions, with LIF higher than the pure gas phase model by a factor of 1.92±0.67, which implies snow emission of HONO must occur. The LIF measured HONO concentrations are not high enough to significantly influence the NO_x budget during ANTCI 2003, but will increase the

modeled HO_x over-prediction by 28%±15% and lead to a dramatic over-prediction of measured OH by 157%±35%. Given the short lifetime of HONO, these differences are hard to reconcile with observed low OH levels unless there is a missing HO_x sink. It appears, however, that HONO competes with O_3 and HCHO as the dominant source of OH at South Pole during ANTCI 2003.

Since pure gas phase chemistry cannot account for the measured high concentration of HONO, a 1D air-snowpack model of HONO was developed and constrained by observed chemistry and meteology data. The 1D model includes pure gas phase chemical mechanisms, molecular diffusion and mechanical dispersion, windpumping in snow, gas phase to quasi-liquid layer phase HONO transfer and quasi-liquid layer nitrate photolysis. Photolysis of nitrate is important as a dominant HONO source inside the snowpack, however, the observed HONO emission from the snowpack is triggered mainly by the equilibrium between quasi liquid layer nitrite and firn air HONO deep down in the snow surface (i.e. 30 cm below snow surface). The high concentration HONO in the firn air is subsequently transported above the snowpack by diffusion and windpumping. Given the limited ANTCI 2003 field measurements of pH and nitrite snowpack concentrations, snow emission of HONO is highly likely and will be transported to 10 meters above the snow, where GT LIF measured high HONO concentration. The pH and thickness of the quasi liquid layer along with continuous nitrite measurement are key factors to calibrate and validate the air snowpack model.

CHAPTER 1

INTRODUCTION

1.1 Overview

The atmosphere is an oxidizing medium. Understanding the important oxidizing processes and rates is crucial to the knowledge of atmospheric composition. Changes in the oxidizing power of the atmosphere would influence air pollution, aerosol formation, greenhouse radiative forcing, and stratospheric ozone depletion (Jacob, 2003). HO_x (OH and HO_2) and NO_x (NO and NO_2) chemistry play pivotal roles in photochemical processes. HO_x radicals initiate nearly all the oxidation paths in the troposphere. In the troposphere, ozone is produced by oxidation of CO and hydrocarbons in the presence of NO_x and HO_x radicals. The conversion between OH and HO_2 is closely linked with the partitioning of NO and NO_2. OH is a key reactive species in the troposphere chemistry and ozone formation, initiating the oxidation of CO, SO_2 and volatile organic compounds (VOCs). The primary source of OH is the photolysis of O_3 to produce an excited state of atomic oxygen, which then reacts with water vapor. OH oxidizes a large number of reduced atmospheric species and has a lifetime of ~1 s. Its main sinks in the troposphere are CO and CH_4.

Nitrous acid (HONO) is a dominant source of OH in the morning in some urban areas (Harris et al., 1982; Pitts Jr. et al., 1994; Andres-Hernandez et al., 1996). In a model study, Jenkin et al. (1988) showed that the photolysis of HONO in the early morning could account for a fivefold increase in OH, a 14% increase at noon and a 16% increase in net photochemical ozone production in the atmospheric boundary layer over the Greater London extensive urban areas. The contribution of HONO to the total OH

budget during the day has long been underestimated in photochemical models. However, more recent measurements show that up to 20% of the total OH is produced by HONO photolysis in a 24-hour period in July/August 1998 at Berlin, Germany (Alicke et al., 2003). Forty two percent of integrated photolytic HO_x formation is attributable to HONO photolysis over the entire day at the Meteorological Observatory Hohenpeissenberg, Germany in summer 2002 and 2004, measured by a coupled wet denuder sampling/ion chromatography analysis technique (Acker et al., 2006). In addition, HONO is considered to be an indoor pollutant (Rasmussen et al, 1995). The reaction of HONO on surfaces can produce N_2O, a climatically important greenhouse gas that also contributes to stratospheric ozone cycles (Crutzen, 1970; Prather et al, 1996).

The following are the sources (1-1 to 1-10) and sinks (1-11 to 1-14) of gas phase HONO:

$$NO + OH + M \rightarrow HONO + M \quad (1\text{-}1)$$

$$HO_2 + NO_2 \rightarrow HONO + O_2 \quad (1\text{-}2)$$

$$2NO_2 + H_2O_{(aq)} \rightarrow HNO_3 + HNO_2 \quad (1\text{-}3)$$

$$NO + NO_2 + H_2O_{(aq)} \rightarrow 2HNO_2 \quad (1\text{-}4)$$

$$2(NO_2)_g \Leftrightarrow (N_2O_4)_g \Leftrightarrow (N_2O_4)_s \xrightarrow{H2O} (ONONO_2)_s \longrightarrow (NO^+NO_3^-)_s \xrightarrow{H_2O} (HONO)_s \longrightarrow (HONO)_g \quad (1\text{-}5a)$$

g : *GasPhase*

s : *SurfaceFilm*

$$2HONO \xrightarrow{surface} NO + NO_2 + H_2O \quad (1\text{-}5b)$$

$$HONO + NO_2^+ \xrightarrow{surface} H^+ + 2NO + O_2 \quad (1\text{-}5c)$$

$$HONO_{(surface)} + HNO_{3(surface)} \rightarrow 2NO_g + H_2O_{(surface)} + O_{2(g)} \quad (1\text{-}5d)$$

$$NO_2 + HO_2 \Leftrightarrow HNO_{4(g)} \quad (1\text{-}6a)$$

$$HNO_{4(g)} \Leftrightarrow HNO_{4(aq)} \quad (1\text{-}6b)$$

$$HNO_{4(aq)} \Leftrightarrow H^+ + NO_4^- \quad (1\text{-}6c)$$

$$NO_4^- \rightarrow O_2 + NO_2^- \quad (1\text{-}6d)$$

$$H^+ + NO_2^- \Leftrightarrow HONO_{(aq)} \quad (1\text{-}6e)$$

$$HONO_{(aq)} \Leftrightarrow HONO_{(g)} \quad (1\text{-}6f)$$

$$HA + h\nu \rightarrow A^{red} + X \quad (1\text{-}7a)$$

$$A^{red} + X \rightarrow A' \quad (1\text{-}7b)$$

$$A^{red} + NO_2 \rightarrow A'' + HONO \quad (1\text{-}7c)$$

$$NO_3^-{}_{(aq)} + h\nu \rightarrow [NO_3^-]^*_{(aq)} \quad (1\text{-}8a)$$

$$[NO_3^-]^*_{(aq)} \rightarrow NO_2^-{}_{(aq)} + O\,(^3P) \quad (1\text{-}8b)$$

$$NO_2^-{}_{(aq)} + h\nu \rightarrow NO + O^-_{(a\,q)} \quad (1\text{-}8b\_1)$$

$$NO_2^-{}_{(aq)} + OH \rightarrow NO_2 + OH^-_{(a\,q)} \quad (1\text{-}8b\_2)$$

$$[NO_3^-]^*_{(aq)} \rightarrow NO_2 + O^-_{(a\,q)} \quad (1\text{-}8c)$$

$$O^-_{(a\,q)} + H_2O \rightarrow OH + OH^-_{(a\,q)} \quad (1\text{-}8d)$$

$$2NO_2 + H_2O_{\,(aq)} \rightarrow NO_2^-{}_{(aq)} + NO_3^-{}_{(aq)} + 2H^+_{\,(aq)} \quad (1\text{-}8e)$$

$$2NO_{2\,(gas)} \leftrightarrow N_2O_{4\,(gas)} \quad (1\text{-}9a)$$

$$N_2O_{4\,(gas)} \leftrightarrow N_2O_{4\,(surface)} \quad (1\text{-}9b)$$

$$N_2O_{4\,(surface)} \rightarrow ONONO_{2\,(surface)} \quad (1\text{-}9c)$$

$$ONONO_{2\,(surface)} + h\nu \rightarrow NO^+_{(aq)} + NO_3^-{}_{(aq)} \quad (1\text{-}9d)$$

$$NO^+_{(aq)} + H_2O_{(aq)} \rightarrow \{(H_2O)NO\}^+_{\,(aq)} \quad (1\text{-}9e)$$

$$\{(H_2O)NO\}^+_{\,(aq)} + H_2O_{\,(aq)} \rightarrow HONO_{\,(aq)} + H_3O^+_{\,(aq)} \quad (1\text{-}9f)$$

$$H_3O^+_{(aq)} + NO_3^-_{(aq)} \rightarrow \{H_3O^+NO_3^-\}_{(aq)} \quad (1\text{-}9g)$$

$$NO+NO_2 \rightarrow ONNO_2 \quad (1\text{-}10a)$$

$$ONNO_2 + H_2O \rightarrow 2HONO \quad (1\text{-}10b)$$

$$HONO + h\nu \rightarrow NO + OH \quad (1\text{-}11)$$

$$OH + HONO \rightarrow H_2O + NO_2 \quad (1\text{-}12)$$

$$O_3 + HNO_2 \rightarrow O_2 + HNO_3 \quad (1\text{-}13)$$

$$HONO + HNO_3 \rightarrow 2NO_2 + H_2O \quad (1\text{-}14)$$

Nitrous acid is produced homogeneously by reactions 1-1 and 1-2 (Calvert et al, 1991; Pagsberg et al., 1997). The bulk of urban HONO is suspected to form either from reaction 1-2 or 1-3 (Winer and Biermann, 1994; Kirchstetter et al., 1996). Measurements at Milan, Italy by Stutz et al. (2002) indicate that one HONO molecule is released into the gas phase for every 33 NO_2 molecules deposited, which shows that direct emission of HONO is an important source in strongly polluted areas. The $HONO/NO_x$ ratio typically reaches a few percent in rural and urban environments and there is clear evidence that the formation of HONO is governed by heterogeneous reactions (Lammel and Cape, 1996).

Finlayson-Pitts et al. (2003) considered N_2O_4 to be a key intermediate in the heterogeneous hydrolysis of NO_2 to form HONO in the atmosphere (reaction 1-5a). By isomerization, the adsorbed dinitrogen tetroxide forms its asymmetric form of $ONONO_2$, which autoionizes generating $NO^+NO_3^-$. In a complex reaction with water, HONO is finally formed and partitions into the gas-phase. Part of the NO is observed in the gas phase originated in secondary reactions of HONO at the surface (reaction 1-5b, c, d). The yield of HONO in the gas-phase is much less than 50% of the NO_2 loss, but including secondary products, such as NO, 50% is found for reaction 1-5a.

The conversion of HNO_4 in the cloud at moderate pH (~4.5) is responsible for heterogeneous source of HONO (reaction 1-6). The most important consequences of this HONO elevation are a factor of two NO_x species increase and regeneration of OH (Williams et al., 2002). This partly compensates for the removal of OH by direct phase transfer into the cloud and may have important implications regarding the oxidizing capacity of the marine boundary layer.

Soil and other surfaces containing humic acid (HA) exhibit an organic surface photochemistry that produces surface species (A^{red}) that can react selectively with nitrogen dioxide to produce HONO under irradiation in the 300-700nm range (reaction 7) (Stemmler et al., 2006). Photo induced nitrous acid production on humic acid surfaces may explain the recently observed high daytime concentrations of nitrous acid in the boundary layer (Zhou et al., 2002a; Kleffmann et al., 2005). The HONO formation rate is first order in NO_2 at low concentrations (5-120 ppb) but is equal to the rate of photochemical production of A^{red} and independent of NO_2 at high gas phase NO_2 concentrations.

Photochemical production of HONO has been reported as products of nitrate photolysis in natural and artificial snow (Honrath et al., 1999, 2000a). Irradiation at wavelengths longer than 280nm may result in reactions 1-8 (a-e) in the quasi-liquid layer on snow surface (Zhou et al., 2001). The quantum yield of reaction 1-8(b) is extremely low with a measured number of about 0.001. In contrast, reported quantum values for NO_2 production are 8 to 9 times greater than the nitrite forming route (Dubowski et al., 2001). The photolysis of nitrite (NO_2^-) can generate NO. Alternatively, NO_2^- can react with oxidants such as ozone or OH, which provides another route for the formation of

OH. Reaction 1-8e is another proposed way to generate NO_2^- by hydrolysis of photo-generated NO_2 (Boxe, 2005). NO_2^- in snow can be protonated to produce HONO which will be released into the gas phase. The NO_2 can react to form symmetric dimer of nitrogen dioxide, N_2O_4 (1-9a and 1-9b). The reactive surface species is proposed to be asymmetric dinitrogen tetroxide, $ONONO_2$, formed by isomerization of symmetric N_2O_4 (1-9c). This species subsequently photolyze to produce the nitrosonium ion, NO^+ (1-9d). NO^+ becomes solvated in the presence of water and then hydrolyzes to form HONO (1-9e and 1-9f), which is efficiently released to the gas phase. In contrast, the nitrate component is retained on the surface as nitric acid trihydrate (1-9g) (Hellebust et al., 2007). The nitrate generated NO and NO_2 can also form N_2O_3, which can further hydrolyze to form HONO (1-10) (Finlayson-Pitts et al., 2003).

The dominant homogeneous chemical loss process for HONO is its photolysis (reaction 1-11) (Reisinger, 2000). This process competes with the homogeneous recombination of the NO and OH radicals (reaction 1-1). The most important heterogeneous chemical removal process is reaction 1-12. Reaction with OH is a minor HONO loss term. The self-reaction of HONO (reaction 1-13) and the reaction of HONO with nitric acid (reaction 1-14) in the gas phase are too slow to be important (Chan et al., 1976; Svensson et al., 1987).

1.2 Chemistry of the polar boundary layer

A series of field campaigns in Polar Regions have spurred intense interest in the photochemistry occurring in snow. In the high latitude Northern hemisphere winter, snow can cover more than 50% of the landmass (Robinson et al., 1993). Because snow has a large surface-to-volume ratio, it can efficiently remove atmospheric trace gases

from the gas phase by adsorption, thus modifying atmospheric composition. Adsorbed gases can release reactive trace gases back to the atmosphere via heterogeneous photochemistry. Adsorption on ice may be an important removal process of HNO_3, of some importance for HONO and peroxyacetyl nitrate (PAN), but apparently irrelevant for NO and NO_2 (Bartels-Rausch et al., 2002). As gas-snow partitioning changes with temperature, emission from or deposition to the snowpack may change with strong temperature changes. Temperature changes are generally associated with changes in meteorological conditions: changes in wind speed and wind direction may affect snowpack ventilation and therefore atmospheric concentrations of HONO and other species that may come out of the snowpack. There seems to be agreement that the nitrate photolysis within the snowpack is the dominant origin of NO_x and HONO in the polar atmospheric boundary layer (Honrath et al., 2000a).

In the quasi-liquid layer (QLL), which is a disordered layer of ice that has chemical properties closer to water than solid crystalline ice (Boxe, 2005), NO_3^- photolysis may produce both NO_2 and NO_2^-. The latter would continue to react to form NO and HONO, NO_2 is identified as the primary emitted species from the photolysis of NO_3^- (Honrath, et al., 2000b; Zhou, et al., 2001). Photolysis will result in depletion of NO_3^- in the quasi-liquid layer and will lead to diffusion of nitrate from the bulk of the snow volume to the quasi-liquid layer. However, light alone is not sufficient to produce significant nitrogen species: Beine et al. (2002) hypothesize that a minimum temperature of the snowpack is needed to allow NO_3^- diffusion out of the snow crystals. Increasing temperature will speed up diffusion. In addition, interstitial HNO_3 may photolyze directly. Below the threshold temperature photolysis will not be effective at transforming

NO_3^- to NO_x. The threshold temperature is a function of the snow type, such as 242K for fresh columns and bullets.

Honrath, et al., (2002) showed that the 24-hour average NO_x and HONO emission rates at Summit, Greenland during the summer of 2000 were approximately 4 times the HNO_3 deposition rates, indicating that NO_x export may remove nitrogen slowly from the boundary layer plus the top few cm of the surface snowpack in summer time. In remote polar regions, snowpack photochemistry provides a way to remobilize deposited HNO_3, thereby influencing NO_x polar photochemistry.

Increasing interest has been focused on the measurement of atmospheric nitrous acid (HONO) in the high latitude boundary layer. HONO plays an important role in the atmosphere due to its photo-dissociation by UV radiation into hydroxyl (OH) and nitric oxide (NO) radicals. Accurate measurement of HONO will improve our understanding of the HO_x ($OH + HO_2$) and NO_x ($NO + NO_2$) cycles that are critically important to atmospheric photochemistry (Finlayson-Pitts et al., 2000). As a result of poor vertical mixing in the polar lower atmosphere, snow pack emissions of HONO remain confined to a thin layer near the surface, where HONO can give rise to a much greater production of OH radicals in Arctic polar sunrise than previously believed (Domine and Shepson, 2002). There is a great discrepancy between the average rate of HONO photolysis (equivalent to a surface emission of 5.3×10^{13} molecules$\cdot m^{-2} \cdot s^{-1}$) and the gradient-based HONO emission (4.6×10^{11} molecules$\cdot m^{-2} \cdot s^{-1}$) by MC/IC technique in 1999 and 2000 (Yang et al., 2002). This discrepancy cannot be resolved by presuming that HONO's lifetime precludes it from mixing throughout the modeled height. Gas-phase chemistry alone fails to explain this inconsistency. A number of measurements (Dibb et al., 2002;

Zhou et al., 2001) report elevated HONO concentrations, sometimes much higher than can be accounted for in photochemistry models. The high levels of HONO reported often lead to a dramatic over-prediction of HO_x (Davis et al., 2004) and sometimes NO_x (Dibb et al., 2004), because these high levels are difficult to reconcile with concurrent measurements of OH, HO_2 and NO. These results raised possible missing sinks for HO_x and NO_x or, alternatively, problems with the HONO measurements.

The Investigation of Sulfur Chemistry in the Antarctic Troposphere (ISCAT) 1998 and 2000 observed NO levels at South Pole Station exceeding those at other polar sites by nearly one order of magnitude. On ISCAT 2000, HONO was measured by the mist chamber method. However, the observed median HONO concentration of 25 pptv (see Table 1.1) was too high to reconcile with models of the HO_x and NO_x budget (Davis et al., 2004). This discrepancy led to great interest in going back to the South Pole to measure HONO using an alternative technique.

Table 1.1 Summary of measured HONO at Polar Sites

Time and Place	1999 July 2-4th Summit	2000 June 27-28th Summit	1992 April Alert	2000 April noon Alert	2000 Dec 27th South Pole		2003 Nov 30th, Dec 1st South Pole				2003 Nov 30th, Dec 1st South Pole
HONO (pptv)	10	15	5-10	10	25	5-71,av30 Median 33	Median 54.5 Mean 56.4		Median 42.4 Mean 45		10
Height	75cm	2m	5 m	5 m	10 m	85 cm	10 m	53.6 median	80cm	51.9 median	10 m
Reference	Dibb et al. 2002	Honrath et al., 2002	Li, Shao-Meng 1994	Zhou et al., 2001	Dibb et al., 2004		UNH MC/IC				GT LIF

1.3 Motivation

Quantifying the amount of HONO emitted by snowpack is important for the photochemistry budget, especially HO_x budget. Furthermore, a deeper understanding of the heterogeneous processes involving snowpack important to HONO is also necessary to account for additional source/sink of HONO. Consequently, one of the main goals of this thesis is the detection and quantitative assurance of these elevated daytime HONO mixing ratios.

We provide observations from ambient HONO measurements during ANTCI 2003 in the austral summer at South Pole. The Antarctic Troposphere Chemistry Investigation (ANTCI) is a four-year program including two major field studies (2003 and 2005) in Antarctica. The major science objectives are to evaluate the physical and chemical processes of nitrogen oxides and hydrogen oxides; to compare boundary layer measurements of South Pole with other regions of Antarctica; and to investigate the importance and location of the coast-to-plateau transport of sulfur.

The overall question of this dissertation is whether the enhanced HONO concentration at the South Pole can be confirmed and if so, can it be explained by either enhanced chemical production inside the snowpack or by stronger vertical transport in the planetary boundary layer.

In the experimental section of chapter 2, we will discuss different HONO measurement techniques, which justify the use of the LIF technique for our studies. The specific setup of the master oscillator / power oscillator (MOPO) will be explained, along with the details of the evaluation procedure and improvements since the work of Rodgers in 1986.

A detailed description of the Antarctic troposphere chemistry investigation (ANTCI) 2003 field campaign is addressed in chapter 3. This includes time series of HONO measurements, meteorological conditions, and an intercomparison with mist chamber/ion chromatography (MC/IC).

The pure gas phase modeling under ANTCI 2003 conditions is described in chapter 4. We present HONO as OH source compared with HCHO and O_3 and the discrepancy between pure gas phase modeling and measurement results.

Chapter 5 focuses on the snowpack as an important photochemical medium in Polar Regions. We describe the wind pumping and actinic flux inside the snowpack. We further discuss quasi liquid layer nitrite as a direct reason for observed high HONO above snow surface and what factors are important to quantify the snowpack HONO emission. Recommendations to further work are given.

The results of this dissertation are summarized in chapter 6.

CHAPTER 2

HONO MEASUREMENT TECHNIQUES

2.1 Overview of detection techniques for nitrous acid

The importance of nitrous acid in troposphere chemistry has been drawn out in detail already. However, the measurements of HONO, which strongly interact with surfaces, are a challenge for any analytical technique.

This chapter explains the basic of the most common HONO measurement techniques (Table 2.1) and the way in which Laser-Induced Fluorescence (LIF) was used.

Current HONO measurements include the following: differential optical absorption spectroscopy (DOAS) (Appel et al., 1990; Platt, 1994; Alicke et al., 2003), Fourier transform infrared spectroscopy (FTIR) (Kagann and Maki, 1983; Barney et al., 2000; Wingen et al., 2000), and laser-induced fluorescence (LIF) (Liao et al., 2006a) which are based on spectroscopy; converting HONO to NO_2^- and analyzing the nitrite by mist chamber/ion chromatography (MC/IC) (Dibb et al., 2002) or the photometric detection of an azo dye derivative by long path absorption photometer (LOPAP) (Heland et al., 2001); aqueous scrubbing using a coil sampler followed by 2,4-dinitrophenylhydrazine (DNPH) derivatization and determining the complex by high-performance liquid chromatographic (HPLC) analysis (*Z*hou et al., 1999); and the diffusion-based denuder/ion chromatography system (Poruthoor and Dasgupta, 1995; Lee et al., 2001; Spindler et al., 2003; Zhang et al., 2003; Acker et al., 2005).

Table 2.1 Comparison of existing technique to detect atmospheric HONO

Technique	DOAS	LOPAP	Denuder	LIF	FTIR	MC/IC	DNPH-HPLC
Detection limit	84 ppt per 5 minutes	1 ppt per 4 minutes	5 ppt per 30 minutes	2-3 ppt per ten minutes	10 ppb	1 ppt per 30 minutes	1-5 ppt per 5 minutes
Comments	↑Well developed technique ↓Significant performance degradation under poor visibility conditions	↑Cheap, sensitive, compact ↓Interferences from NO_2+phenols	↑High sensitivity ↓Artifacts ↓Long integration time	↑Real time measurement ↓Potential interference of laser generated OH	↓Not sensitive to most atmospheric HONO concentrations	↑High sensitivity ↓Long integration time	↑High sensitivity ↓Interference from HO_2NO_2, NO, NO_2, PAN etc.
Reference	Alicke et al., 2003	Kleffmann et al., 2006	Acker et al., 2005	Liao et al., 2006a	Tuazon et al., 1980	Dibb et al., 2004	Zhou et al., 1999

Differential Optical Absorption Spectroscopy (DOAS) is based on the Beer-Lambert law of light absorption: light in the visible and / or near UV wavelength range collected by some optics along the path through the atmosphere is spectrally analyzed in a spectrograph-detector system, where the spectrum is analyzed to gain information on the structure and amount of absorption by molecules that took place along the path. The molecular absorption bands in the UV and visible regions tend to be rather broad because simultaneous electronic, vibrational, and rotational transitions are involved. Only those species what have sufficiently structured electronic absorption spectra can be used for DOAS. The most important part is the separation of extinction of the light intensity into broad-band Rayleigh (at air molecules) and Mie (at aerosols) scattering as well as narrow-band differential absorption by trace gases present at a certain differential optical density. As the strength of the absorption structures varies with wavelength, only those absorbers with absorption structures sufficiently strong are detectable with DOAS instruments. Typically 2 to 10 trace gas absorptions can simultaneously be identified in a single atmospheric DOAS spectrum (Platt, 1994). Average trace gas concentrations of HCHO, NO_2, O_3 and HONO are retrieved by simultaneously fitting resolution adjusted reference spectra using the combined linear-nonlinear least-square algorithm. The near-ultraviolet spectrum of HONO has been investigated using different source reactions for the formation of HONO (Johnston and Graham, 1974; Cox and Derwent, 1976; Stockwell and Calvert, 1978; Kanda and Taira, 1990; Ning and Pfab, 1997). While there is general agreement on the vibronic structure, the determination of absolute absorption cross sections has been a difficult task because of the photolysis and thermal

decomposition of HONO giving rise to NO_2. NO_2 absorbs in the same region as HONO and it is difficult to isolate its absorption signal from that of HONO, especially due to the high concentrations in heavily polluted urban areas. Strong absorption bands of HONO can be found at 330.68, 341.68, 354.13, 368.15, and 383.8 nm. Depending on the optical length of DOAS, typical detection limit of HONO is from 30 to 200 pptv. The average time resolution of the DOAS measurements is 137s (Alicke et al., 2003; Platt, 1994; Trick, 2004).

The FTIR (Fourier Transform Infrared) spectrometer technique uses a typical infrared light source such as a Nernst glower, in conjunction with slits and gratings to restrict the wavelength intervals reaching the detector. The conversion of the signal intensity as a function of optical path difference (the interferogram) into signal intensity as a function of wavelength requires applying a Fourier transform. As the sample is added, the infrared spectrum will change and the difference is characteristic of the infrared-absorption species in the sample. FTIR detects nitrous acid by its absorption structures at a wavelength of 12.6 μm. A wide variety of other pollutants, like PAN, NH_3, HCHO, HNO_3 and O_3, can be monitored with sufficient sensitivity for many ambient air studies. The versatility is one of the significant advantages of FTIR. The instrument is very complex and used more in laboratory studies than in the atmospheric measurements. Furthermore, the detection limit is 2-4 ppbv, which can only be applied to heavily polluted areas. It is not suitable for in situ measurement of HONO (Tuazon et al., 1980).

In the Mist Chamber/Ion Chromatography (MC/IC) techniques, HONO is converted to NO_2^- which is analyzed. The gases are concentrated into a small volume of

ultra pure water. The samples are frozen to -20ºC within 30 minutes of collection and maintained frozen until just before ion chromatography. It has a detection limit of 1 ppt every half hour and is widely used in many field experiments, especially HNO_3 measurements (Dibb et al., 1994, 1998, 2002, 2004).

The LOPAP instrument designed to be a cheap, sensitive, compact, and continuously working HONO monitor. It is based on wet chemical sampling and photometric detection. HONO is sampled by a fast chemical reaction in the mixture of sulphanilamide in hydrochloric acid with >99.9% uptake efficiency for 1L min^{-1} gas flow. At such low pH, several chemical interferences caused by e.g. NO_2 are minimized. HONO from the constant sample gas flow is collected continuously into the liquid phase and reacts immediately to form a diazonium salt. By adding n-(1-naphthyl) ethylenediamine-dihydrochloride solution, the final color intensive azo dye is produced, which is detected photometrically. In the external sampling unit a series of two-channel system is used: the first stripping coil takes out almost all the HONO but only a small fraction of any interfering species. The second coil takes out the same amount of the interfering species but has almost no HONO. By subtracting both, possible interferences are minimized. The instrument is calibrated by exchanging the stripping solution by a nitrite standard diluted in the stripping solution, while running under zero air. It is validated in the laboratory for HONO concentrations of using ion chromatography and with DOAS instrument in a large outdoor smog chamber. LOPAP instrument has systematically higher values comparing with the DOAS instrument. Detection limits range from approximately 1 pptv with response time from 4 min. The accuracy of the measurements is 7% (Heland et al., 2001, Kleffmann et al., 2006).

The DNPH-HPLC technique is based on aqueous scrubbing of HONO using two coil samplers, followed by derivatization of the scrubbed nitrite into a highly light-absorbing medium (300μM DNPH and 8 mM HCl at 45°C). The azide derivative, 2, 4-dinitrophenyl azide (DNPA) is highly UV-absorbing and is separated from DNPH reagent and hydrazones by C_{18} reverse-phase high-performance liquid chromatographic (HPLC) using acetonitrile and water as mobile phases. DNPA is detected with an UV detector at 309nm. Potential interference includes NO_x, PAN and carbonyl compounds. The detection limit is less than 5 pptv and each sample is completed within 5 minutes.

The denuder technique is wet-chemical sampling for the measurements of a variety of atmospheric species based on the diffusion properties. The use of denuders is effective and relatively inexpensive, but much experimental work is needed to avoid interference with other atmospheric species like NO_2 and PAN (Febo et al., 1993, Acker et al., 2005). The retention efficiency of PAN, which hydrolyzes in alkaline media to liberate NO_2^- was reported to be 5-10% of the incoming PAN amount (Ferm and Sjodin, 1985; Allegrini et al., 1987). This positive interference of low reactivity compounds can be accounted for by operating two denuders in series. NO_2^- collected on denuders is rapidly oxidized to NO_3^- when ozone is present in the air stream (Perrino et al., 1990). This may lead to the underestimation of HONO and an overestimation of HNO_3 concentrations unless HNO_3 is selectively removed from the sampling air after sample collection. For measurement of HONO, one NaCl-coated denuder is used to remove HNO_3, followed by two Na_2CO_3 plus glycerol-coated denuders to collect HONO and take interference of nitrogen oxides into account. The denuders are leached with deionized water and analyzed by ion chromatography. A denuder technique without a large surface

area inlet device in order to minimize retention and/or production of gaseous atmospheric pollutants during sampling is recommended (Ianniello et al., 2007). The detection limit is 5 pptv per 5 minutes (Acker et al., 2005).

The chemical techniques are typically much cheaper, easier to use and can be much more sensitive with detection limits as low as ~1 pptv (Kleffmann et al., 2006). However, since HONO is sampled on dry or liquid surfaces and HONO is likely generated heterogeneously on the surfaces, these instruments suffer from chemical interferences and sampling artifacts (Zhou et al. 2002b). Significant differences were observed in previous intercomparison studies of chemical HONO instruments with DOAS technique (Appel et al., 1990; Febo et al., 1996; Coe et al., 1997; Spindler et al., 2003). The chemical instruments measured significantly higher concentrations during the day. The differences were explained by interferences of the chemical instruments. Therefore, the development of validated, sensitive and fast HONO instruments is very importance to quantify the oxidation capacity of the atmosphere and to understand the formation of HONO.

Rodgers (1986) photolyzed HONO to generate OH and measured the OH photo-fragment using laser-induced fluorescence. The detection limit achieved was 10 pptv for an integration time of 15 minutes. A major problem with this technique is the tendency to generate artificial OH signals. Depending on the laser energy and the ambient levels of ozone and water vapor, this OH artifact can overwhelm the signal from photolysis of HONO. Another problem is the large and sometimes variable non-resonant fluorescence background signals (Bradshaw et al., 1984). An integration time of 15 minutes is also too long for tracking quickly altering HONO concentrations during sampling events such as

at sunrise. The basic approach, however, remains valid, and with the appropriate light sources, data acquisition algorithms, sampling methods, and careful attention to the background, can form the basis for a state of the art HONO measurement with fast time response.

2.2 Laser-induced fluorescence (LIF) detection of HONO

2.2.1 Theory of LIF detection of HONO

PF-LIF allows for the detection of polyatomic molecules possessing excited states that do not fluoresce. The spectrum and photochemistry of HONO make it an excellent candidate for detection by the PF-LIF technique. HONO itself is non-fluorescent and possesses a near-ultraviolet band (300-390nm) spectrum involving an n → π* type exciting in the —N=O chromophore (Vasudev et al., 1983). The A-X transition involves promotion of a nonbonding electron from the O atom to the lowest π* orbital on the NO moiety (Shan et al., 1989). The absorption spectrum of HONO shows that it has peaks at 342, 354, and 369 nm, involving excitation within the 2_0^3, 2_0^2 and 2_0^1 bands in the υ_2 N=O stretch, suggesting that the only internal coordinate that has a significant change is the N=O bond length (Vasudev et al., 1984). The third harmonic of Nd:YAG laser is at 354.7 nm and makes it an excellent candidate to photo-fragment HONO. The 354.7 nm wavelength is used to pump the 2_0^2 transition. Previous studies by Cox (1974) have shown a near unity primary quantum yield (λ_l=355 nm) for the process:

$$HONO + h\upsilon_1 \ (\lambda_l=355 \text{ nm}) \rightarrow OH \ (X^2\Pi, v''=0) + NO \qquad \Phi_A=0.95 \qquad (2\text{-}1)$$

Where Φ_A is the quantum yield.

Both of these photo fragments, OH and NO, may be readily detected by laser-induced fluorescence with high sensitivity. The substantially larger ambient concentration of NO_2, which photo-dissociates to NO and O at the same wavelength relative to HONO precludes measurement of the NO fragment, so the HONO detection scheme is based on the detection of the OH photofragment (Figure 2.1):

$$OH\ (X^2\Pi,\ v''=0) + h\upsilon_2\ (\lambda_2=282\ nm) \rightarrow OH\ (A^2\Sigma,\ v'=1) \quad (2\text{-}2a)$$

$$OH\ (A^2\Sigma,\ v'=1) + M \rightarrow OH\ (A^2\Sigma,\ v'=0) + M^{\ddagger} \quad (2\text{-}2b)$$

$$OH\ (A^2\Sigma,\ v'=0,\ 1) \rightarrow OH\ (X^2\Pi) + h\upsilon_3\ (\lambda_3 \sim 309\ nm) \quad (2\text{-}3)$$

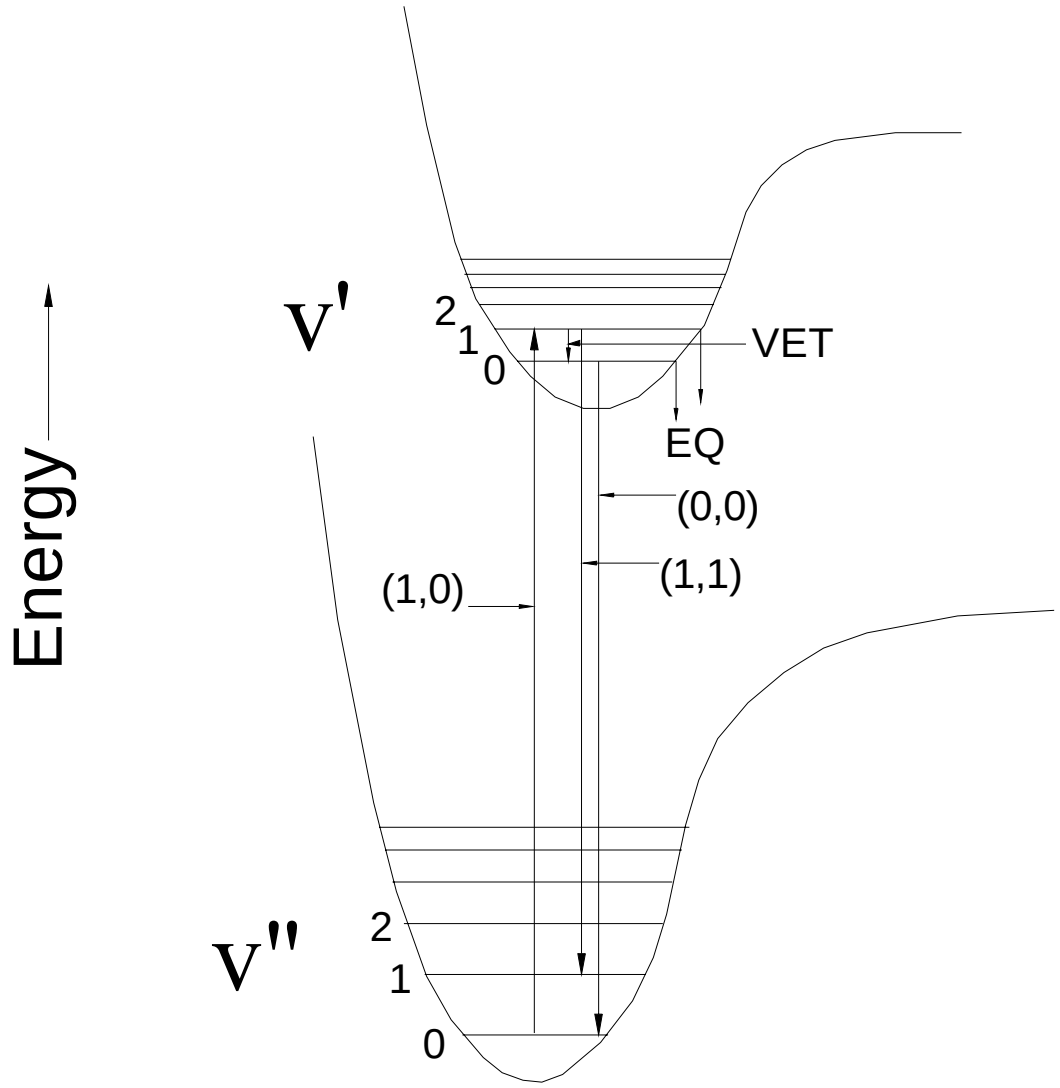

Figure 2.1 Energy diagram of LIF of OH: v"=0 state OH is excited at 282 nm to v'=1 state and the fluorescence near 309 nm back to v"=0, 1 state is monitored. (VET: vibration energy transfer, EQ: electronic quenching)

The laser is typically tuned to either the $Q_1(2)$ or $P_1(1)$ line of the OH (1, 0) band at 282nm. These lines are chosen because they are strong lines that are part of an easily recognizable pattern in the absorption spectrum. The difference in the line strengths between the $P_1(1)$ and the $Q_1(2)$ is accounted for by in-situ calibration. Collisions with N_2, O_2, and H_2O lead to significant electronic quenching, which result in attenuated fluorescence emissions from vibrational states both in v'=1 and v'=0 of $A^2\Sigma$ state. Most of the fluorescence comes from v'=0 which is populated via vibrational energy transfer from v'=1 level. The red-shifted OH fluorescence near 309 nm is easily discriminated from laser Rayleigh scattering as well as the first three Raman lines from N_2 and O_2.

At atmospheric pressure, the fluorescence efficiency is ~ $6x10^{-4}$ (Rodgers, 1986). Vibrational energy transfer (VET) and quenching rates of N_2, O_2 and H_2O are list in Table 2.2 according to previous experiments (Cleveland et al. 1988, Bailey et al. 1997, 1999, Steffens et al., 2000). The rate of N_2 caused VET is around 9 times the rate of quenching, whereas the rate of O_2 caused VET is only 1/9 to 1/4 the rate of quenching. The polar molecule H_2O has a quenching rate 2 to 4 times that of O_2 and 15 to 20 times of that of N_2 yet a relatively small VET rate which implies a strong quenching effect of even small amounts of water vapor (McDermid et al., 1982). The calculated contributions at room temperature of N_2, O_2, and H_2O to the total quenching of OH are listed in Table 2.3. N_2 dominates the VET, O_2 and N_2 are most important quenchers under dry conditions.

Table2.2 caption: Rate coefficients (10^{-10} $cm^3 \cdot molecule^{-1} \cdot s^{-1}$) for quenching and vibrational deactivation of OH $A^2\Sigma$ at 294K by N_2, O_2, and H_2O. (k_v: VET rate from 1 to 0; k_{Q0}, k_{Q1}: quenching rates from v'=0 and 1, respectively)

Gas	k_v	k_{Q0}	k_{Q1}
N_2	3.21[a]	0.34[b]	0.43[a]
O_2	0.33[a]	1.39[b]	3.06[a]
H_2O	c	6.91[d]	6.74[e]

a Steffens et al., 2000; b Bailey et al. 1997; c omitted.
d Bailey et al., 1999; e Cleveland et al. 1988, T=298K.

Table 2.3 caption: Quenching percentage for N_2, O_2, H_2O colliding with OH $A^2\Sigma$ (v' = 0 and v' = 1) at 294K under different water vapor mole mixing ratio (other colliders omitted)

Mixing ratio of H_2O	N_2	O_2	H_2O	Total quenching percentage increase by adding water	OH (v'=0) state	OH (v'=1) state
0	42.3%	57.7%	0	0	72.5%	27.5%
100ppm	42.2%	57.7%	0.1%	0.1%	72.4%	27.6%
1000ppm	41.8%	57.2%	1%	1.1%	72.3%	27.7%
1%	38.2%	52.6%	9.2%	11.0%	71.1%	28.9%
5%	27.7%	39.4%	32.9%	54.8%	66.2%	33.8%

This technique is both highly sensitive and specific to the detection of HONO. The system is calibrated by standard addition and verified by UV/VIS differential optical absorption spectroscopy.

2.2.2 Instrumental description of LIF detection of HONO

Figure 2.2 presents a schematic illustration of the optical layout in the PF-LIF HONO detection system. The necessary UV wavelengths 355 nm and 282 nm can be achieved using two Spectra Physics Quanta Ray model GCR290-10 (Mountain View, CA) Nd:YAG lasers. One is used to generate the 355 nm photolysis beam; the other is used to pump an optical parametric oscillator (OPO) to generate the 282 nm probe beam. The output energy of the GCR290 is around 1.5 J/pulse at 1.06 nm. This beam is frequency tripled to generate 700 mJ of 355 nm light. 200 mJ of the third harmonic is used to pump a grating-tuned OPO (the "master oscillator") to generate a narrow-line width signal beam at 564 nm. This signal beam is used to seed another parametric oscillator (the "power oscillator") pumped by 300 mJ of the remaining 355 nm light to generate 15-20 mJ of 564 nm light, which is then frequency doubled to generate 1-2 mJ of light at the 282 nm probe wavelength. The timing of the photolysis beam alternates at every shot, preceding the probe by 100 ns on a given shot, and following the probe by 200 ns on the next shot. The ambient OH signal is determined by calculating the difference between the signals acquired when the photolysis beam precedes the probe and when the photolysis beam follows the probe: the signal measured when the photolysis beam follows the probe provides the background signal (including contributions from ambient OH, any instrument generated OH, and any Raman signal from the probe); the signal measured when the photolysis beam precedes the probe is the OH signal from

HONO. There was no significant difference in differential signal strength when the probe delay after the photolysis beam was varied between 100 and 200 ns.

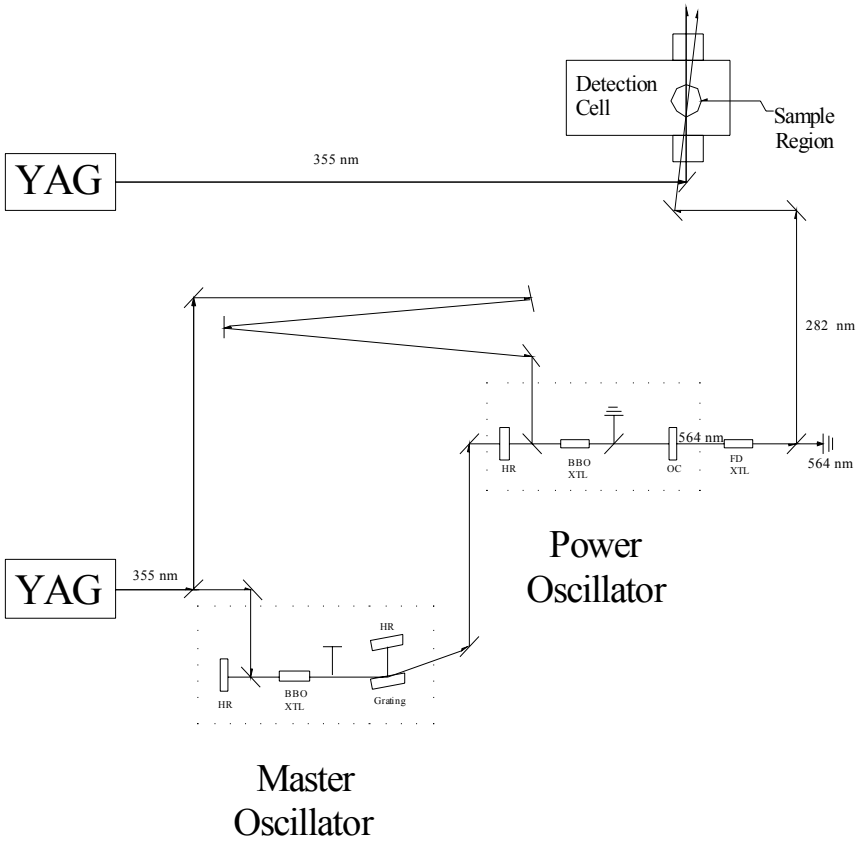

Figure 2.2 LIF OH measurement instrumentation: (BBO: beta barium borate, FD: frequency doubling, HR: high reflector, XTL: crystal, OC: output coupler)

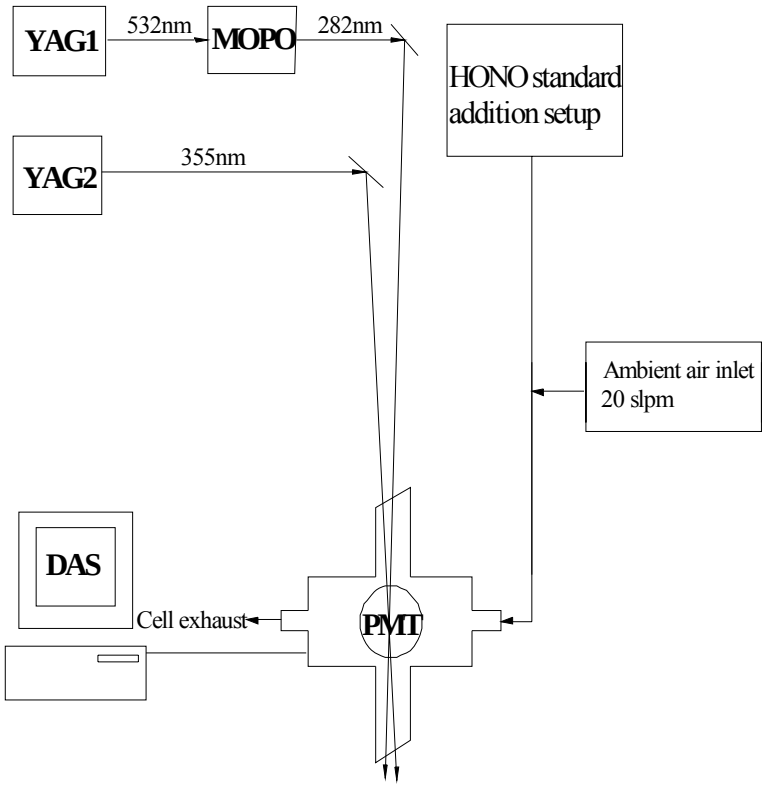

Figure 2.3 LIF HONO measurement instrumentation (MOPO: Master Oscillator / Power Oscillator, PMT: Photomultiplier Tube, DAS: Data Acquisition System)

Directly above the sampling region, a filter pack is installed which optimizes the 309 nm fluorescence transmission. The filter pack consists of nine dichroic filters (Andover; Salem, NH) coated to maximize reflection at 309 nm and maximize transmission at the 282 nm wavelength (Figure 2.4). The signal is collected on a Hamamatsu R331 PMT (Bridgeport, CT). Fluorescence data are collected on a single-shot basis with a VXI-based track-and-hold data acquisition system, which also collects reference cell fluorescence data. Temperature and pressure in the sampling cell and temperatures of various parts of the instrument such as the OPO cavities and the coolant

temperature are also monitored. The data acquisition system also controls the timing of the two lasers.

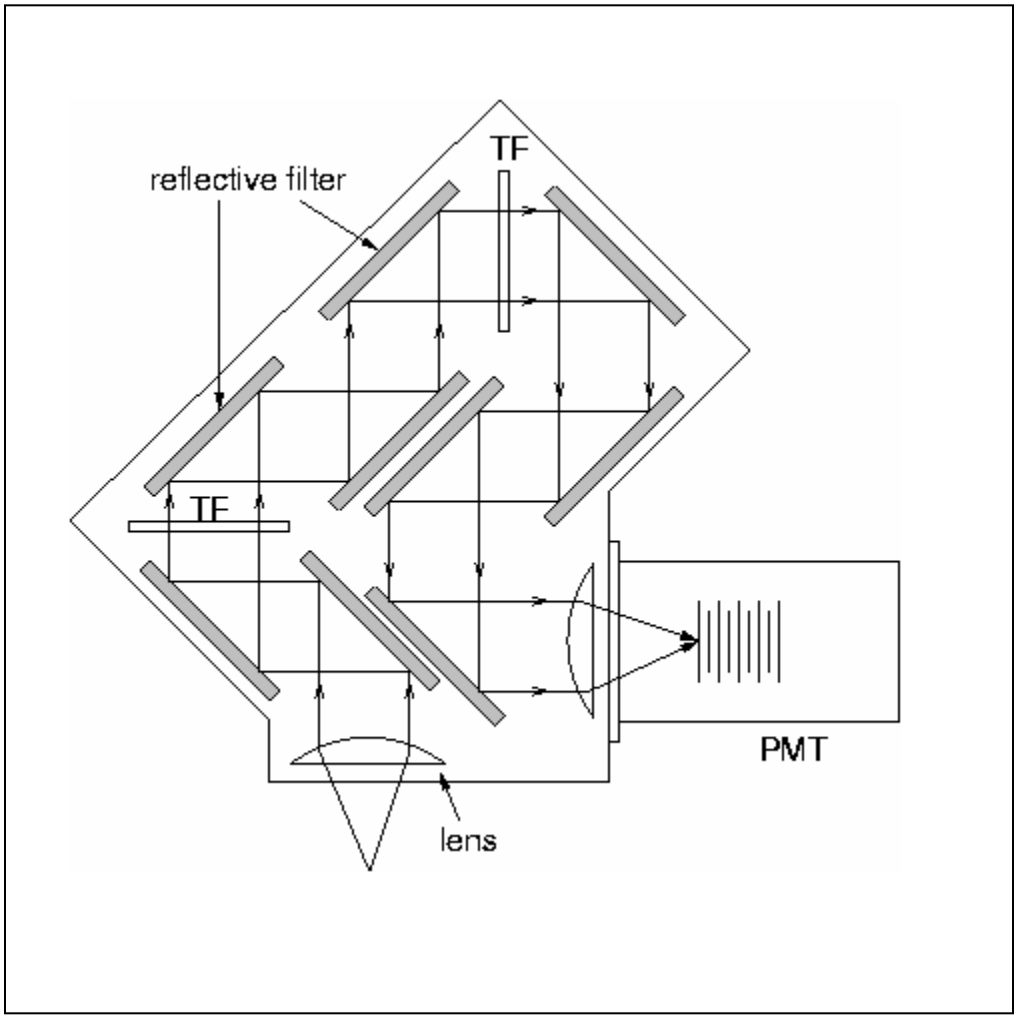

Figure 2.4 Schematic of HONO detection filters pack (TF: Transmission Filter)

2.2.3 Calibration of LIF detection of HONO

The PF-LIF instrument was calibrated using standard addition. Gaseous nitrous acid was produced using a similar method as Cox and Derwent (1976) and Masafumi and Yukio (1990). A 1 slpm flow of dry nitrogen (N_2) was passed over a solution of sulfuric acid (H_2SO_4) and sodium nitrite ($NaNO_2$). The homogeneity of the solution was ensured

by the use of a magnetic stirrer. Figure 2.5 illustrates the HONO generation chamber setup for calibration purposes.

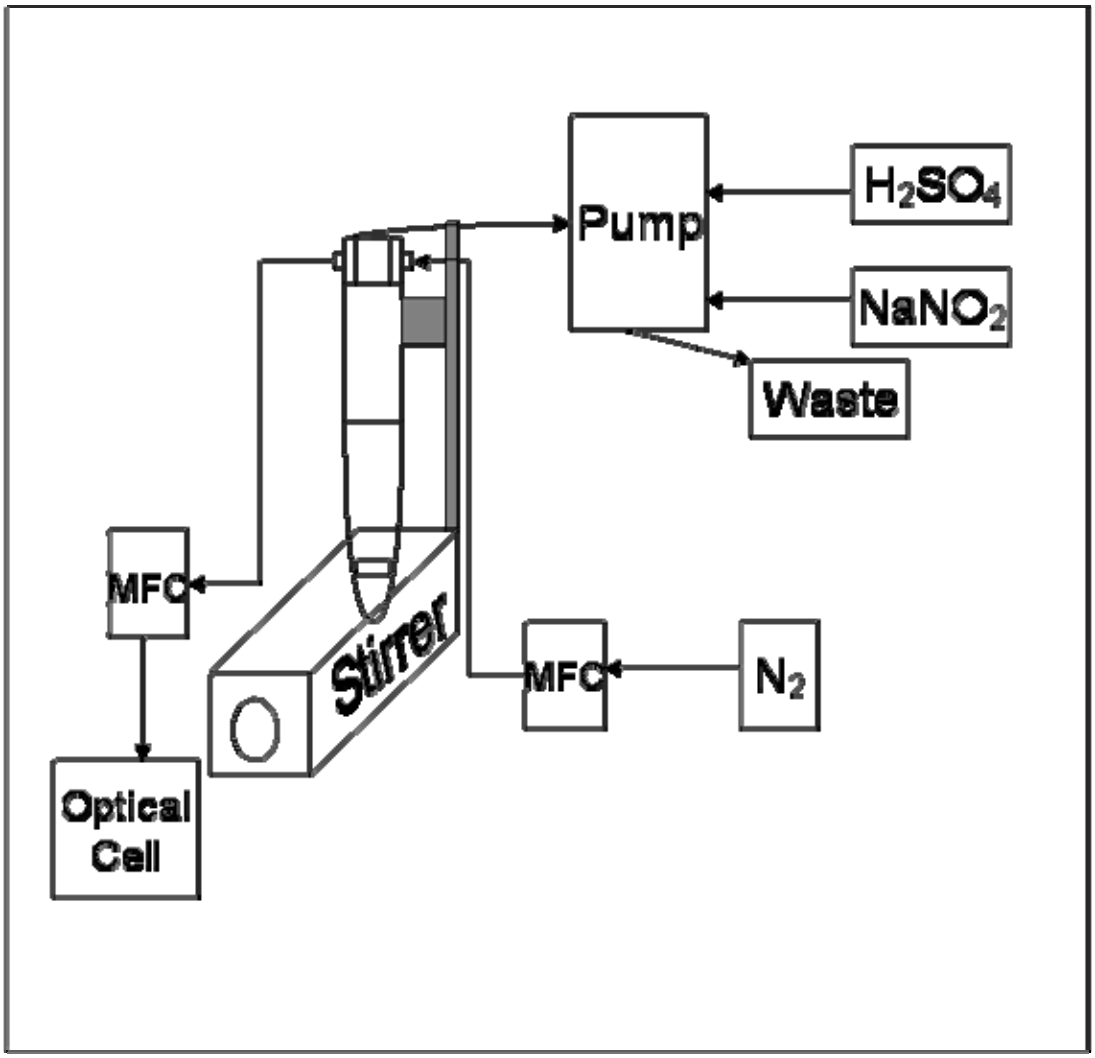

Figure 2.5 HONO generation cell setup (MFC: Mass Flow Controller)

The reaction chamber was made of glass with three entry ports, one for N_2 gas and one for each of the reactant liquids. There are two exit ports, one for the gaseous products of the reaction accompanied by N_2 as the carrier gas, and the other one for removing the liquid waste from the reaction. The continuous flow of N_2 through the reaction chamber ensures a constant flow of HONO to the optical cell. The mixture of

HONO and N_2 from the reaction cell was added to a 20 slpm flow of N_2 and directed to the optical cell. The flow rate of N_2 was chosen to represent a typical flow of ambient air during field missions.

$NaNO_2$ ($1.7x10^{-6}$ M) (Fisher Sci. CAS 763-00-0) and H_2SO_4 ($2.0x10^{-4}$ M) (Fisher Sci. 7664-93-9) solutions were prepared from analytical reagent grade reagents and pumped separately into the reaction cell. The sum of the flow rate for both of the reactants was equal to the flow rate of the exhaust line, thus providing a stable level of liquid inside the reaction chamber. The flow rates of the solutions were controlled by changing the diameter of the tubes used with a three-channel Masterflex PA-21 peristaltic pump (Cole-Parmer; Chicago, IL). The pH of the solution was kept constant at 2 to keep the Henry's Law constant of HONO at 46 $atm \cdot M^{-1}$ (Becker et al., 1996). One slpm of HONO and N_2 from the reaction cell was added to the N_2 flow of 20 slpm to produce a HONO concentration of approximately 500 pptv. The flow out of the reaction cell was controlled to change the dilution ratio of the total flow to the reaction chamber flow, thus different concentrations of HONO were produced for instrument calibration. Efforts were made to minimize the residence time of HONO in the system to avoid issues such as dark decay, adsorption and heterogeneous reactions with the surfaces.

To distinguish and characterize the background noise of the instrument, the 355 nm beam was blocked and data were collected during the calibration process. HONO does not photolyze at 282 nm and the signal collected with the photolysis beam blocked accounts for ambient OH, instrument generated OH by ozone photolysis, and 282 nm probe leakage. Data were also collected while the beam was unblocked for the same

period of time. The signal is calculated as the difference between the blocked and unblocked portions of the calibration sequence.

In order to perform sensitivity tests for this system, the 1 slpm flow from the reaction cell was mixed into a 20 slpm flow of synthetic air made of a mixture of 80% N_2 (Airgas, Randor, PA) and 20% O_2 (Airgas, Randor, PA). The flows of N_2 and O_2 were regulated before they reached the optical cell to equal a typical flow of ambient air to the cell during field missions.

The performance of the instrument is shown in Figure 2.6. To record a zero signal, a synthetic air mixture of N_2/O_2 gas (i.e. no HONO addition) was passed through the optical cell and data was collected. The 2-sigma limit of detection for HONO with this system was 2-3 pptv for ten-minute integration time in lab with 35% uncertainty. Most of the uncertainty comes from the laser power fluctuation and calibration. During Antarctic Troposphere Chemistry Investigation (ANTCI) deployment, the detection limit was found to be 6 pptv for one-minute integration time due to the low interference levels and low pressure at South Pole with 35% uncertainty.

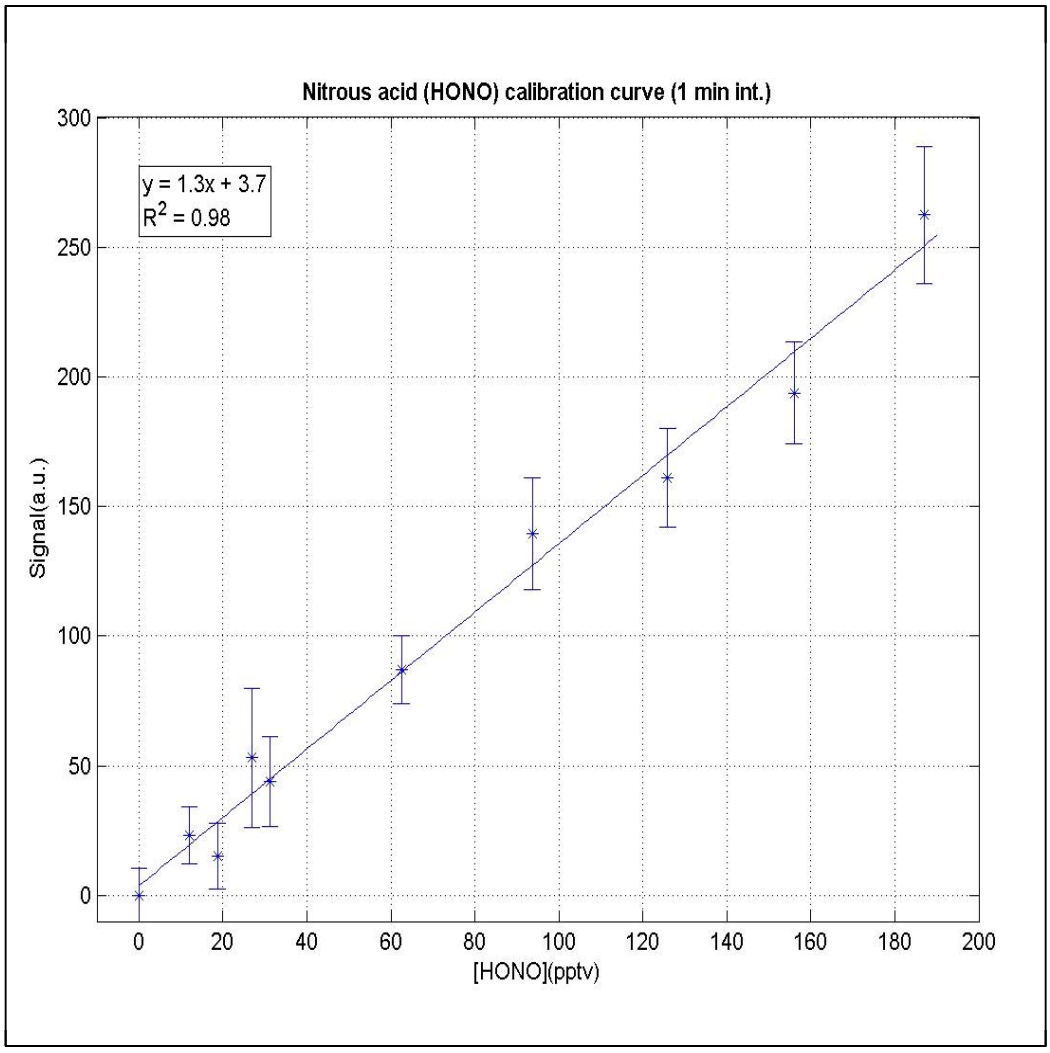

Figure 2.6 Calibration curve for PF-LIF

A potential source of interference with the OH signal in this system is the generation of artificial OH signals. The 282 nm wavelength that is used for OH monitoring causes the production of atomic oxygen O (^{1}D) from Ozone (O_3).

$$O_3 + h\nu \rightarrow O(^1D) + O_2 \ (\lambda < 310 \text{ nm}) \qquad (2\text{-}4)$$

The oxygen atom reacts with available water vapor in the sampling flow and produces OH radicals (Davis et al., 1981).

$$O(^1D) + H_2O \rightarrow OH + OH \qquad (2\text{-}5)$$

$$O(^1D) + M \rightarrow O(^3P) + M \qquad M = N_2 \text{ or } O_2 \qquad (2\text{-}6)$$

For the purposes of this experiment theoretical calculations were conducted to estimate the concentration of OH produced from O_3 dissociation and ambient water vapor. Due to increased interest in the photochemistry of HONO over snow pack (Houdier et al., 2002; Zhou et al., 2001; Bottenheim et al., 2002; Dibb et al., 2002), the initial deployment location for this instrument is the South Pole. To calculate a theoretical yield for OH radical for typical conditions at the South Pole, an O_3 concentration of 30 ppbv, a pressure of 687 mbar, a temperature of 241K and dew point temperature of 238K were used. The laser power for the 282 nm beam was assumed to be 10 mJ per pulse and the pulse width was 10ns. The equations and methods used for this calculation were similar to that of Davis et al. (1981). The resulting OH concentration from these calculations was 1 pptv. This interference level is approximately half of the signal from photolysis of HONO.

It should be noted, however, that both the ambient and the ozone generated OH concentration are accounted for as part of the background, which is subtracted from the main signal at 5 Hz. The ozone generated OH will only be significant if it contributes to an excessively high background level. This may be an issue in regions of high humidity, high ozone, and low HONO levels (Table 4). Most regions of high ozone and humidity will have significant levels of HONO, however, since NO_2 (the direct precursor of ozone) in the presence of water vapor produces HONO on surfaces (Ramazan et al., 2004). Even so, this potential decrease in the signal-to-background ratio must be kept in mind. In fact, calculations based on reported values of ozone, water vapor, temperature, and NO_2 for the field campaigns NITROCAT (NITRous acid and its influence on the Oxidation

Capacity of the ATmosphere), FORMAT (FORMAldehyde as a tracer of oxidation in the Troposphere) and Turm (Trick, 2004) indicate that the PF-LIF method would have a better signal to background ratio than the HONO measurements reported by DOAS.

Other potential interferences may arise from other species that photolyze at 282nm or 355 nm to produce OH. We have been unable to identify any such species which may be a significant interference. Table 2.4 shows the relative interference from 1 ppbv of H_2O_2, HNO_3, CH_2O, HO_2NO_2, and the background signal from 100 ppbv ozone and a range of water vapor concentrations. In principle, there may be large organic peroxides yet to be identified which may provide interference; however, the vapor pressures of these species are expected to be quite low.

Table 2.4 Calculated laser generated OH concentration(pptv) in the detection cell in urban regions

100ppbv O_3					1ppbv HONO	1ppbv HCHO + 1ppbv HO_2NO_2	1ppbv H_2O_2	1ppbv $HONO_2$
0.1%H_2O	0.5%H_2O	1%H_2O	2%H_2O	5%H_2O				
12	59	113	209	430	297	0.16	1.1	0.03

Further improvements may be implemented in this system by changing the probe beam wavelength to 308 nm. This will result in a lower limit of detection, by decreasing the ozone interference and therefore the background signal. In order to do this, the sampling pressure must be reduced to extend the fluorescence lifetime and enable temporal gating of the laser pulse. The reduction in pressure would also further reduce contributions from laser generated OH (Hard et al, 1980, 1984). Other improvements include reducing the size of the lasers and using an excimer lamp to photolyze HONO, which would facilitate the deployment and use of the instrument during field missions. A tunable HONO photolysis laser will be helpful to assess interferences.

CHAPTER 3

ANTARCTIC TROPOSPHERE CHEMISTRY INVESTIGATION (ANTCI) 2003 FIELD STUDIES AND RESULTS

3.1 Introduction of ANTCI 2003 experiments

The Antarctic Troposphere Chemistry Investigation (ANTCI) is a four year program including two major field studies (2003 and 2005) in Antarctica. The major science objectives are evaluating the physical and chemical processes of nitrogen oxides and hydrogen oxides; comparing boundary layer measurements of South Pole with other regions of Antarctica; and investigating the importance and location of the coast-to-plateau transport of reduced sulfur.

Measurements during ANTCI 2003 at the Amundsen-Scott South Pole Station include: OH, HO_2 and H_2SO_4 by Selected Ion Chemical Ionization Mass Spectrometry (SICIMS); HONO by MC/IC and LIF; HO_2NO_2 and SO_2 by CIMS; HNO_3 by CIMS and MC/IC; NO and NO_y by chemiluminescence; O_3 by UV ozonesonde and Electrochemical Concentration Cell (ECC) ozonesondes; PAN by Gas Chromatography with Electron Capture Detection(GC/ECD); H_2O_2 and HCHO by Coil Scrubbers/Fluorescence Spectroscopy; non-methane hydrocarbons, halocarbons, CH_4, CO, and DMS by GC/Flame Ionization Detector (FID), aerosol chemical composition and Hg by various techniques: Inductively-Coupled Plasma Mass Spectrometry (ICP-MS), Atomic Absorption Spectrometry (AAS), IC, and alpha- and gamma-spectroscopy; temperature, relative humidity, wind speed, wind direction by Vaisala tethersondes and Vaisala radiosondes; and boundary layer height by acoustic sounder. Actinic Fluxes were

obtained from an ultraviolet spectroradiometer located in the Atmospheric Research Observatory (ARO) and maintained by Biospherical Instruments, Inc.

Table 3.1 ANTCI 2003 measurement techniques summary

Compound	LOD[a]	Technique	Investigator	Affiliation
OH	1 x 10^5 molecules·cm^{-3}/5 min	Selected Ion Chemical Ionization Mass Spectrometry (SICIMS)	F. Eisele R. Mauldin E. Kosciuch	National Center for Atmospheric Research (NCAR)
MSA				
H_2SO_4				
HO_2/RO_2	5 x 10^5 molecules·cm^{-3}/5 min			
HONO	2-3 pptv/10 min	Laser Induced Fluorescence	D. Tan J.Mastromarino	Georgia Institute of Technology
HNO_3	5pptv/1 min	Chemical Ionization Mass Spectrometry (CIMS)	G. Huey D. Tanner S. Sjostedt	
HO_2NO_2				
SO_2				
NO	2pptv/1 min	Chemiluminescence	D. Davis M. Buhr	
NO_y	50pptv/1 min			
Peroxyacetic Nitric Anhydride (PAN)	5pptv/5 min	Gas Chromatography with Electron Capture Detection (GC/ECD)	J. Roberts	National Oceanic and Atmospheric Administration (NOAA)
			F. Flocke	NCAR
HNO_3	1 pptv/30 min	Ion Chromatography/Mist Chamber (IC/MC)	J. Dibb	University of New Hampshire
HONO				
HCOOH				
CH_3COOH				
H_2O_2	40pptv/1 min	Coil Scrubbers, Fluorescence Spectroscopy	M. Hutterli R. Bales	University of Arizona
CH_2O	30pptv/2 min			
Non-Methane Hydrocarbons	3 pptv/1 min	GC, Flame Ionization Detector (FID)	D. Blake	University of California, Irvine
alkyl nitrates	0.1 pptv/1 min			
Halocarbons	0.01 pptv/1 min			
DMS	1 pptv/1 min			

Aerosol Chemical Composition	vary from species to species	Inductively-Coupled Plasma Mass Spectrometry (ICP-MS), Atomic Absorption Spectrometry (AAS), IC, and alpha- and gamma-spectroscopy	R. Arimoto	New Mexico State University
Hg	Suitable for South Pole		S. Brooks S. Lindberg	NOAA
Temperature		Sky-Doc tethered balloons, UV ozonesonde, Vaisala tethersondes, Vaisala radiosondes, electrochemical concentration cell (ECC) ozonesondes	D. Helmig	University of Colorado, Boulder
Relative Humidity				
Wind Speed				
Wind Direction				
O_3				
Mixing Layer Depth		Acoustic Sounder	W. Neff	NOAA
Actinic Fluxes		Spectroradiometer	-	Biospherical Instruments, Inc

a) LOD : Limit of Detection

Ambient measurements were conducted at the Atmospheric Research Observatory (ARO) at South Pole during ANTCI in November and December of 2003. One face of the ARO held the *in-situ* experimental probes and faced the clean air sector, a zone between grid 360-110 degrees extending 148 km from South Pole and 2 km above the snow surface. The clean air sector has a very long fetch into the mean katabatic flow from the Antarctic Plateau.

The photo fragmentation/laser-induced fluorescence (PF-LIF) technique was used to measure atmospheric HONO 10 meters above the surface. Ambient air is drawn into the sample cell at 30 L/min through a 1/2" I.D. teflon tube ~2.5m long extending about 10 cm outside the wall of the ARO facing the clean air sector. The first 30 cm of the inlet tube was maintained at ~297K. The residence time in the inlet was ~0.5 s. There was no significant difference in signal whether the inlet heater was turned off or not, indicating

that inlet surface reactions were not important in the very dry conditions found in ANTCI. HONO in the sample cell is photo fragmented at 355 nm with the third harmonic of a YAG laser and the generated OH radical is probed at 282nm; the photolysis beam alternately precedes and follows the OH probe beam, automatically accounting for ambient as well as any instrument-generated OH; the excited state OH fluorescence at 309 nm is detected by photomultiplier tube.

Table 3.2 Summary of ANTCI 2003 HCHO, HO_2NO_2, H_2O_2, $HONO_2$ measurement results

	HCHO (pptv)	HO_2NO_2 (pptv)	H_2O_2 (pptv)	$HONO_2$ (pptv)
Mean	70	40	230	90
Max	340	68	500	353
Min	1	2	40	0.4

Table 3.3 Calculated laser generated OH concentration (pptv) per pulse with 1 mJ 282 nm and 300 mJ 355 nm in the detection cell at South Pole

30 ppbv O_3, 0.05%H_2O	6 pptv HONO	70 pptv HCHO + 40 pptv HO_2NO_2	230 pptv H_2O_2	90 pptv $HONO_2$
0.98	0.97	0.01	0.14	0.002

Table 3.2 lists the typical concentrations of measured HCHO, HO_2NO_2, H_2O_2 and $HONO_2$. Table 3.3 shows the laser generated OH concentrations per pulse. In reality, we do not discriminate between ambient OH and 282 nm O_3 generated OH. We distinguish the 355nm generated OH from the sum of ambient OH, probe beam 282 nm generated OH, and photolysis beam 355 nm generated OH. Generally speaking, real OH LIF signals from HONO are 0-15% higher than the background signal. This detection scheme is direct, fast, and free from identifiable interferences, including hydrogen peroxide, nitric acid, and pernitric acid.

The system was calibrated by standard addition every 3 hours. A 1 slpm flow of dry nitrogen was passed over constant mixing of $NaNO_2$ and H_2SO_4 solutions to generate standard additions of HONO (typically 12 to 50 pptv). The 2-σ detection limit of the technique was typically 2-3 parts per trillion by volume (pptv) for HONO, with a sample integration time of 10 minutes. The relative uncertainty was estimated to be about ± 35%, driven largely by calibration uncertainty and laser power fluctuations. Measurements were typically taken for the 12 hours per day that the inlet was over sunlit snow.

3.2 ANTCI 2003 HONO measurement results

HONO was measured in the ARO on Nov 30th, Dec 1st, 3rd, 15th, 17th, 21st, 22nd, 25th, 27th and 28th (Figure 3.1 top panel). The median mixing ratio of HONO 10m above the snow in this period was 5.8 pptv (6.3 pptv mean), reaching a maximum value of 18.2 pptv on Dec 1st. We see the highest concentrations at the end of November; a period marked by cold temperatures, and a shallow boundary layer. NO levels (shown in Figure 2 and taken to be representative of other surface-emitted species) measured in the ARO at this time are also highly elevated, indicating surface emissions into a small mixing volume. HONO levels decrease in early December, when the boundary layer is relatively deep; NO levels in this time period are relatively low. HONO levels increase again around December 22nd, a period also marked by high levels of NO, HNO_3, and HNO_4. The HONO levels we report here by LIF are lower than previous observations reported by MC/IC from ISCAT 2000 (Dibb et al., 2004) and much lower than concurrent MC/IC measurements.

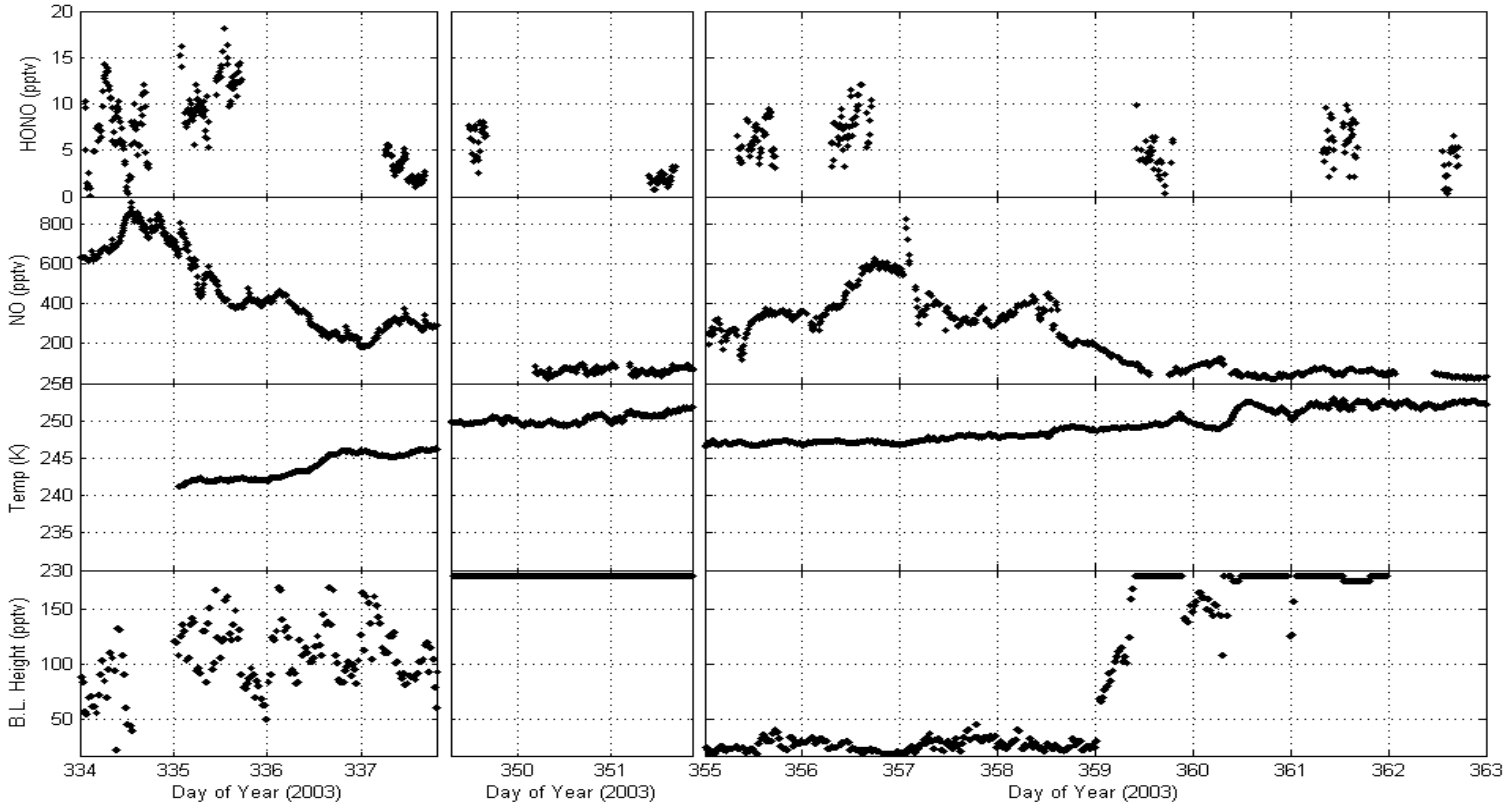

Figure 3.1. Temporal plot of HONO (pptv), NO (pptv), temperature (K) and boundary layer height (m). Observed HONO mixing ratio was at 10 m above the snow at South Pole on Nov 30th, Dec 1st, 3rd, 15th, 17th, 21st, 22nd, 25th, 27th and 28th during ANTCI 2003. The highest line in the boundary layer height panel is 180 m, which indicates that data were collected and analyzed for mixed layer depth but none was found. The maximum range of the sodar deployed was 175m.

Figure 3.2 shows HONO levels for Dec 1st showing the typical variability over the 12 hour measurement period. Since there was no night during ANTCI 2003, diurnal variability is driven largely by wind direction, presence of cloud cover, and presumably snow-phase chemistry.

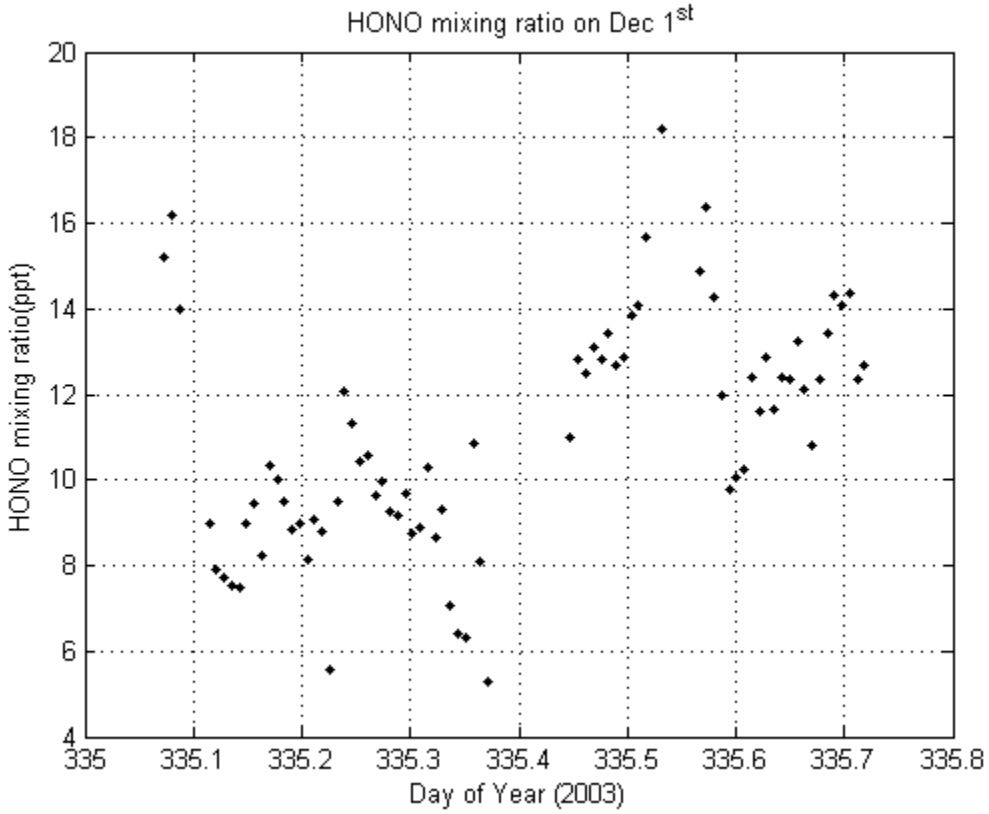

Figure 3.2 HONO observations on Dec 1st, 2003 10 m above the snow at South Pole.

In 2003, mixing ratios of NO reach 900 pptv; these high NO_x concentrations are highly correlated with atmospheric stability and are believed to result from snowpack emissions. Because NO is both a gas-phase precursor to HONO and a photolysis product, it may be interesting to compare the behavior of these two species. Overall, the median HONO to NO ratio is 2%, except for the last two days when the ratio increased to 10%. The correlation between the two, however, is poor (Figure 3.3).

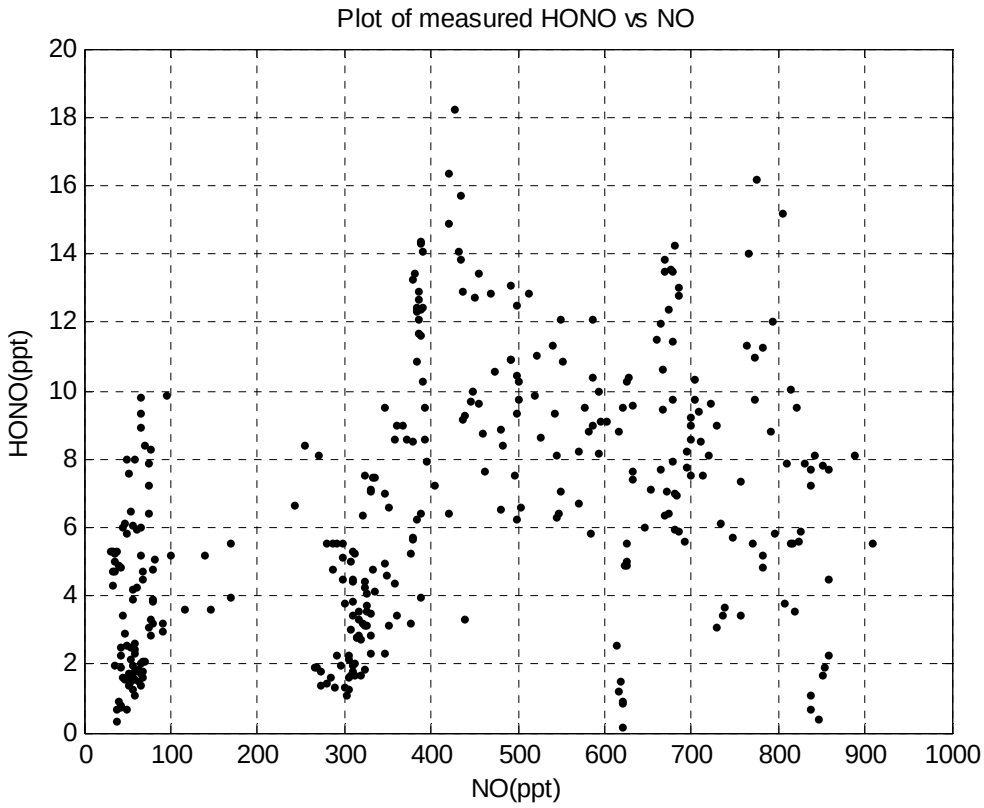

Figure 3.3 Scatter plot of the mixing ratio of HONO versus NO. The correlation is very poor (r^2=0.17)

The poor correlation (r^2=0.17) is not surprising, however, given that the median lifetime of NO_x at ANTCI 2003 was 13 hours, whereas the median lifetime for HONO was only 6 minutes. HONO will be much more sensitive than NO to local conditions and less sensitive to chemistry upwind. Furthermore, the snow emission chemistry is complex and involves heterogeneous processes and interstitial photochemistry. Factors could influence the HONO source like HNO_3 deposition rate, rate of photolysis of NO_3^- and NO_2^-, pH of snow, wind speed, solar radiation etc. If photolysis of nitrate (NO_3^-) is the dominant source of HONO, and the HONO generation is the secondary step through NO_2^-. NO_2^- photolysis is considerably faster than that of NO_3^-; depending on properties such as the temperature dependence of the snow-phase reactions, partitioning and

quantum yield of the involved processes, NO, NO_2, or HONO may be dominant products. It is neither expected nor necessary that the NO/HONO ratio be fixed.

HONO was also measured by mist chamber/ion chromatography analysis (MC/IC) of the NO_2^- ion by the University of New Hampshire (Dibb et al., 1994, 2002). Most of the MC/IC measurements were taken at the snow surface adjacent to the ARO; however, MC/IC HONO data for Nov 30th and Dec 1st at 10 m in the ARO are also available. The MC/IC observed HONO levels at both the surface and from the ARO are significantly higher than the PF-LIF observations, and also higher than was reported in ISCAT 2000. There is no noticeable trend in MC/IC surface versus 10m data, at least for the two days MC/IC data are available from the ARO. Overall, MC/IC HONO data from ANTCI 2003 were 7.2±2.3 times higher than LIF HONO data (Figure 3.4) with no correlation (r^2 is 0.017).

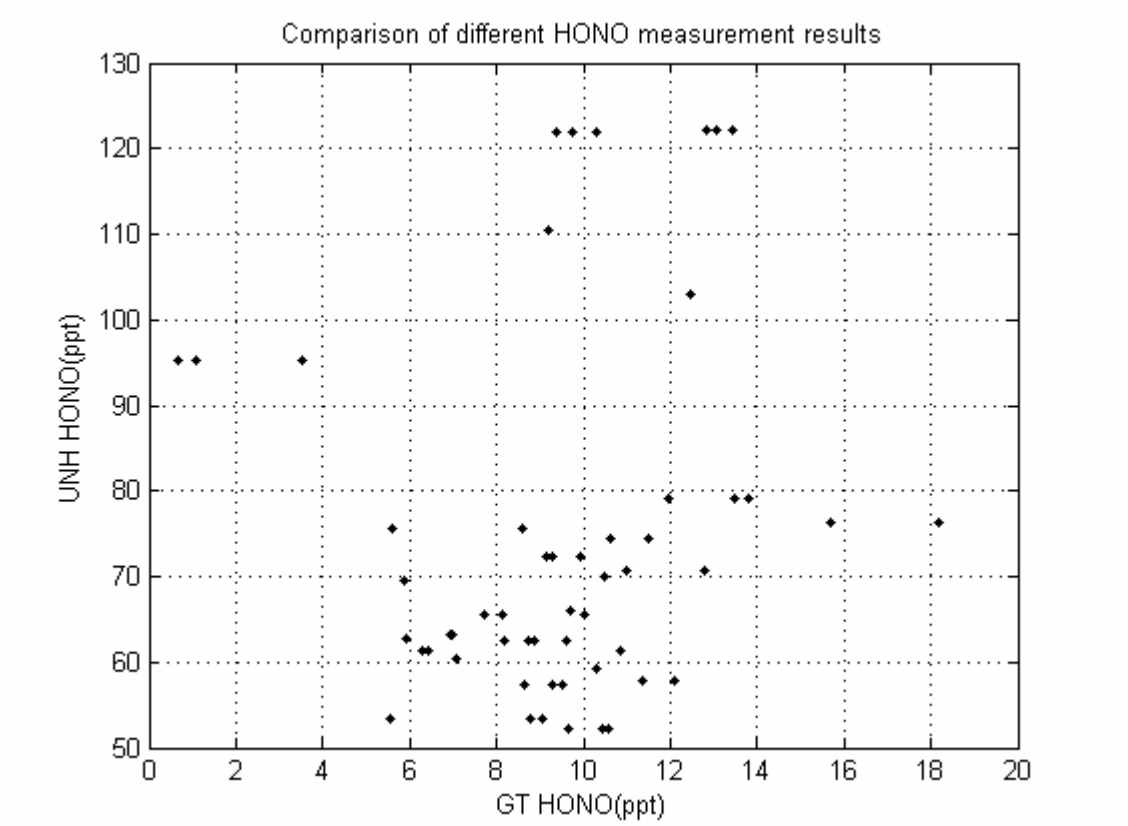

Figure 3.4 Comparison of different HONO measurements on Nov 30th and Dec 1st (UNH: MC/IC; GT: LIF) (r^2=0.017)

At present we do not have a definitive explanation for the large discrepancy found in ANTCI between measurement techniques. An intercomparison of the two techniques at 10m was unsuccessful: the median HONO mixing ratio at 10 m for the intercomparison period by MC/IC is 55 pptv, while that by LIF is 10 pptv. Exchange of calibration standards was also unsuccessful: the LIF calibration source produced interferences for the MC/IC measurement not observable by LIF, and the MC/IC source (dissolved nitrite) was not suitable for the gas-phase LIF measurement. It should also be noted that concurrent LIF and MC/IC HONO data are limited and the intercomparison is not performed in a controlled setting, further complicating a detailed assessment of the differences. It is possible that the MC/IC technique might suffer from interference from

HNO_4. During the intercomparison period, the MC/IC HONO observations appeared to track the sum of LIF HONO and HNO_4 as measured by CIMS (S. Sjosted, personal communication, 2005). We also cannot rule out the possibility that the LIF measurement was actually less sensitive than reported. Possible other reasons for this discrepancy include the different inlets and time scales used for the two techniques which could result in adsorption of HONO, heterogeneous hydrolysis of NO_2 or positive interferences from NO_2^- or other nitrogen oxides, in particular pernitric acid.

3.3 ANTCI 2003 conclusions

The ANTCI 2003 measurements confirm the high HONO levels observed previously in ISCAT 2000 (Table 3.2), although there is significant discrepancy in the HONO measurements by LIF and MC/IC.

Table 3.4 Comparison of existing results of HONO measurements 10 meters above snow at South Pole, both MC/IC measurements were reported by Dibb.

Time	2000 Dec 27th	2003 Nov 30th- Dec 1st	
Technique	MC/IC	MC/IC	LIF
Median HONO (pptv)	25	55	10

Both the LIF and MC/IC techniques observed higher than expected levels of HONO; however, the MC/IC observations were higher than the LIF observations by a factor of 7.2±2.3 in the median. HONO as measured by LIF technique roughly follows NO levels and scale inversely with boundary layer height. A number of factors could influence the HONO concentrations observed during ANTCI, including the HNO_3 deposition rate, the rate of photolysis of snow-phase NO_3^-, the concentration of NO_2^-, the pH of snow, wind speed, and solar radiation, etc. A air snowpack modeling effort in

chapter 5 is developed to understand HONO during ANTCI 2003, including the possible snow HONO source.

CHAPTER 4

GAS PHASE MODEL RESULTS OF ANTCI 2003 HONO CONCENTRATION

4.1 Gas phase model description

Figure 4.1 shows the scheme of the gas phase photochemical box model, assuming all calculated species (HONO, NO_2, O, CH_3O, CH_3O_2, OH, HO_2, H_2O_2 and HCHO) to be in steady state. It is typically constrained by observed values for O_3, NO, HNO_3, HNO_4, $J(NO_2)$, $J(O^1D)$, pressure, temperature and dew point. It also accommodates observational constraints of CH_4, CO, C_2H_6 and PAN when measurements are available; when they are not available, the values are estimated by interpolation. Gas kinetic rate coefficients are taken from JPL Chemical Kinetics and Photochemical Data for use in Atmospheric Studies (Sander et al., 2006). The photolysis coefficients of HONO, HNO_3, HO_2NO_2, PAN and HCHO are provided by Dr. Gao Chen. The model is modified with constrained HONO as reported by LIF to evaluate the importance of HONO with respect to HO_x and the possible magnitude of snow emission of HONO.

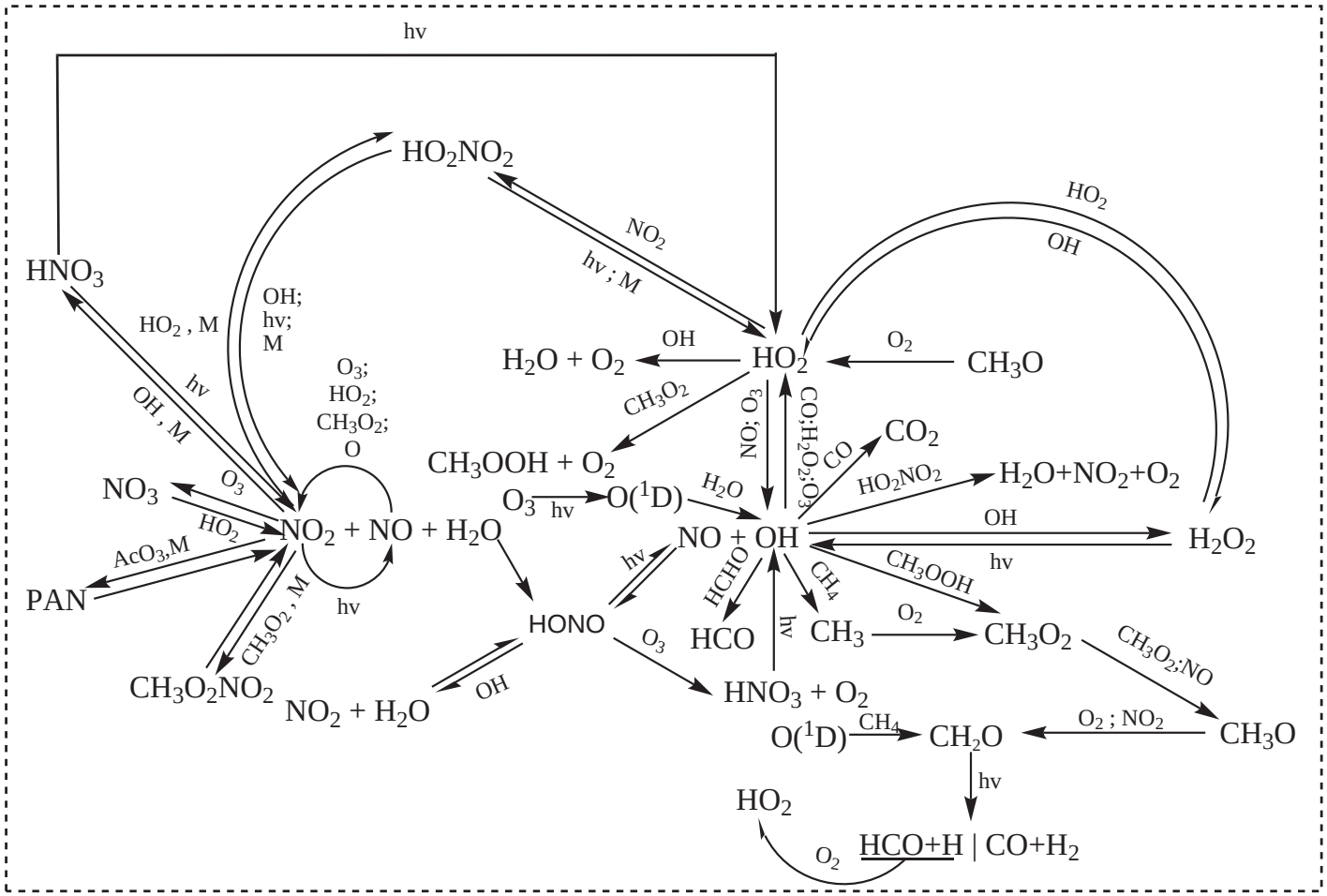

Figure 4.1 Scheme of gas phase modeling

The calculated species (HONO, NO_2, O, CH_3O, CH_3O_2, OH, HO_2, H_2O_2 and HCHO) are assumed to be in steady state.

4.2 Gas phase model results of ANTCI 2003 data

Figure 4.2 shows the scatter plot of LIF measured HONO versus the modeled steady-state HONO. The median HONO levels as observed by LIF are about 92%±67% higher than the modeled HONO.

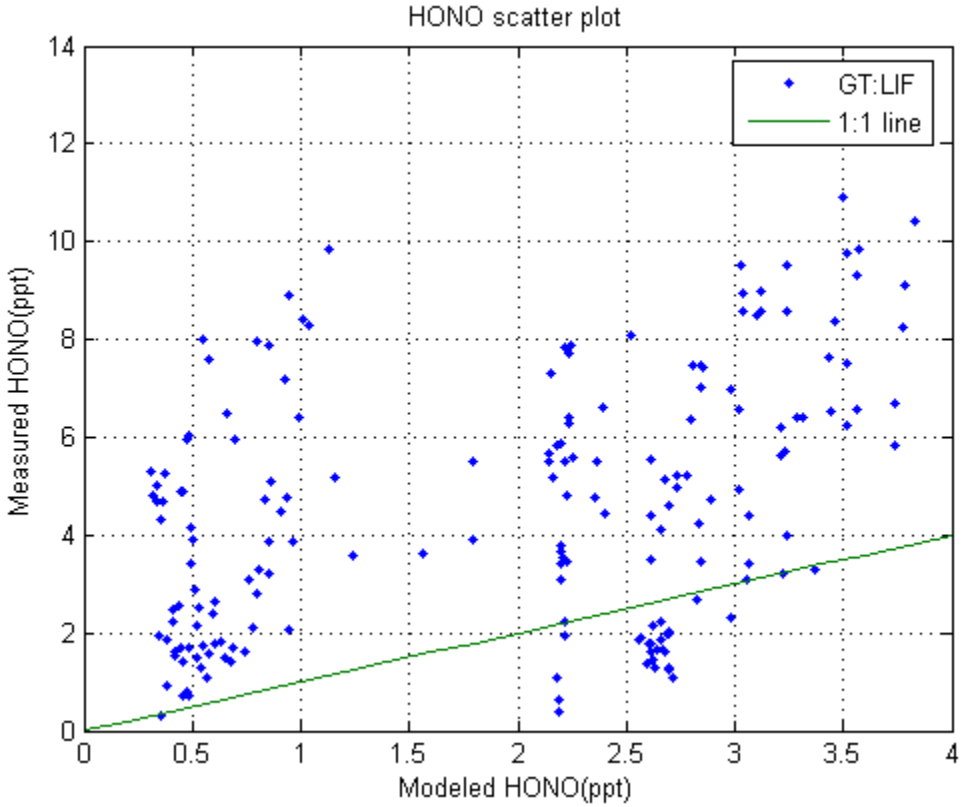

Figure 4.2 Comparison of GT measured HONO with the modeled HONO (GT: Georgia Institute of Technology). A few outliers were removed. The median value of GT measured HONO over modeled HONO ratio is 1.92±0.67

The discrepancy between model HONO and observed HONO may not be surprising if snowpack is a HONO source, as Zhou et al. (2001) observe. There is no snow source in the pure gas-phase model. We can infer a snow emission term by forcing the model to match the observations. This inferred emission term is generally positive and has a median value of (8.33±0.54) $\times 10^4$ molec·cm^{-3}·s^{-1} (Figure 4.3). Concurrent

measurements made by the UNH group using MC/IC found median HONO mixing ratio at 80 cm above the snow is 42 pptv. On Nov 30th and Dec 1st, the UNH group also measured at 10 m as part of an intercomparison. However, due to the large discrepancy between our 10m results (Figure 3.4), it is impossible to quantify the HONO surface flux directly from observations alone. A more comprehensive 1-D modeling is needed in order to better understand other possible HONO source terms and snow surface HONO flux (see Chapter 5).

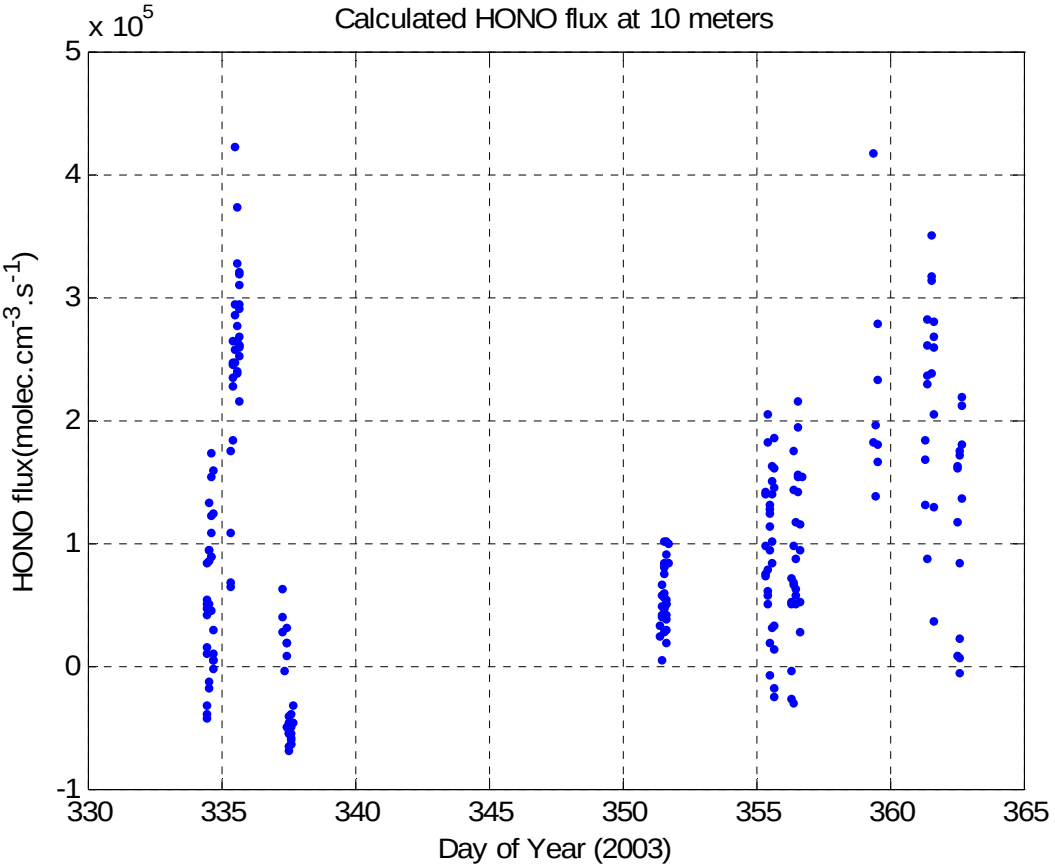

Figure 4.3 A snow HONO emission is inferred according to the measured elevated HONO concentration. This inferred emission term is generally positive and has a median value of (8.33±0.54) $\times 10^4$ molec·cm^{-3}·s^{-1}

Unconstrained modeled OH was 78%±20% higher than observed OH using the technique of SICIMS (Tanner et al.,1997) (Figure 4.4); OH calculated by a model with

constrained HONO, on the other hand, was 157%±35% higher than observed OH, in which case HONO is the dominant source of OH compared with photolysis of O_3 and HCHO. If the HONO concentration is calculated from steady-state, its OH production rate would be substantially underestimated. The results also suggest an unaccounted HO_x sink mechanism in current gas phase model. For example, OH reactions with organic compounds (Anastasio et al., 2007) and addition channel of HO_2 reaction with NO_2 (Butkovskaya et al., 2007) can be a significant sink.

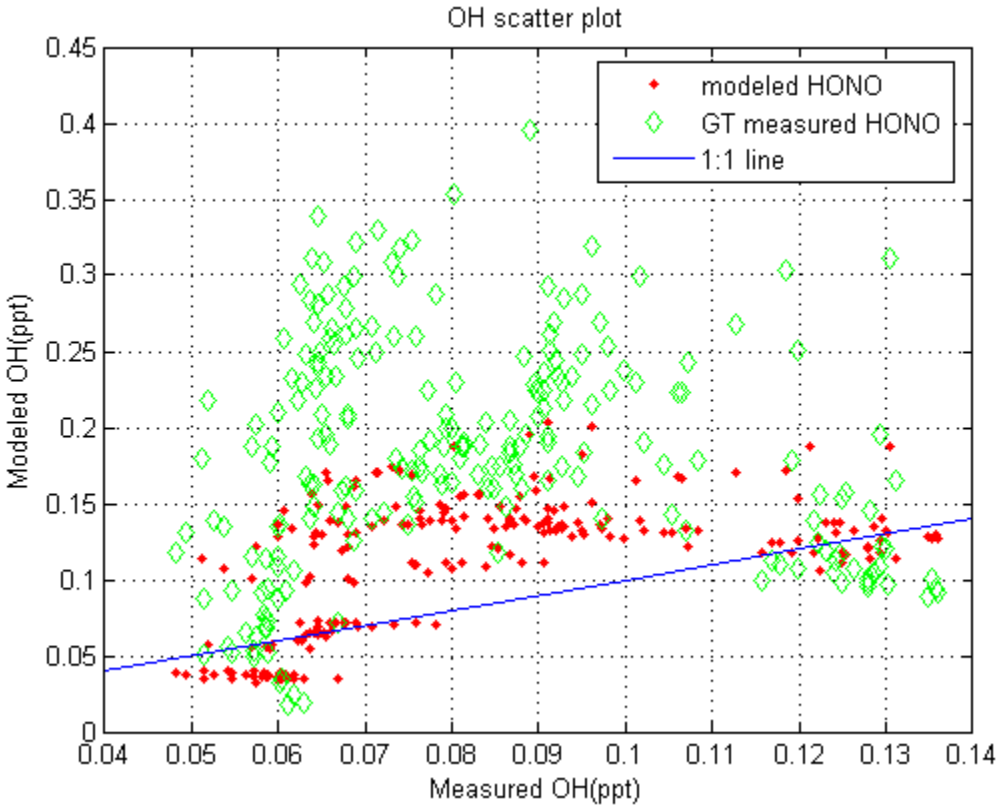

Figure 4.4 Comparison of measured OH with modeled OH using HONO constrained by LIF and unconstrained HONO. The median value of modeled OH constrained by LIF HONO over unconstrained model HONO ratio is 1.3±0.2.

Table 4.1 The OH formation rate from O_3, CH_2O and HONO

Reaction		Rate Constant
$HONO + h\nu$	$OH + NO$	j_{HONO}
$O_3 + h\nu$	$O_2 + O(^1D)$	j_{O3}
$O(^1D) + H_2O$	$2OH$	k_1
$O(^1D) + N_2$	N_2	k_2
$O(^1D) + O_2$	$O + O_2$	k_3
$O(^1D) + CO_2$	$O + CO_2$	k_4
$CH_2O + h\nu$	$H + HCO$	j_{CH2Oa}
$CH_2O + h\nu$	$H_2 + CO$	j_{CH2Ob}
$H + O_2$	HO_2	k_5
$CHO + O_2$	$HO_2 + CO$	k_6
$HO_2 + NO$	$OH + NO_2$	k_7
$HO_2 + O_3$	$OH + 2O_2$	k_8
$HO_2 + HO_2$	$H_2O_2 + O_2$	k_9
$OH + CH_4$	$H_2O + CH_3$	k_{10}
$OH + CO$	$CO_2 + H$	k_{11}
$OH + NO_2$	HNO_3	k_{12}
$OH + O_3$	$HO_2 + O_2$	k_{13}

The OH formation rate from O_3,CH_2O,HONO

$$r(OH,O3)= \frac{2k_1[H_2O]}{k_1[H_2O]+k_2[N_2]+k_3[O_2]+k_4[CO_2]}\ jO_3[O_3]$$

$$r(OH,CH2O)=(k_7[NO+k_8[O_3])\left[\frac{\left((k_7[NO]+k_8[O_3])^2+8k_9 \cdot j_{CH2Oa}[CH_2O]\right)^{1/2}-(k_7[NO]+k_8[O_3])}{2k_9}\right]$$

$$r(OH,HONO)=j_{HONO}[HONO]$$

We calculate the OH formation rate according to Li (1994) (Table 4.1). The HCHO concentrations are measured by Manuel Hutterli and Roger Bales of the University of Arizona, while O_3 mixing ratios are measured by Detlev Helmig of the University of Colorado. The measured HONO will be dominant OH source (Figure 4.5). On the other hand, the pure gas phase modeled HONO will compete with HCHO and O_3 as major OH source (Figure 4.6). Contributions from HONO photolysis are higher than those from O_3 and HCHO on Nov 30th, Dec 1st, 3rd, 21st and 22nd while lower than those

from O_3 and HCHO on Dec 15th, 17th, 25th, 27th and 28th.

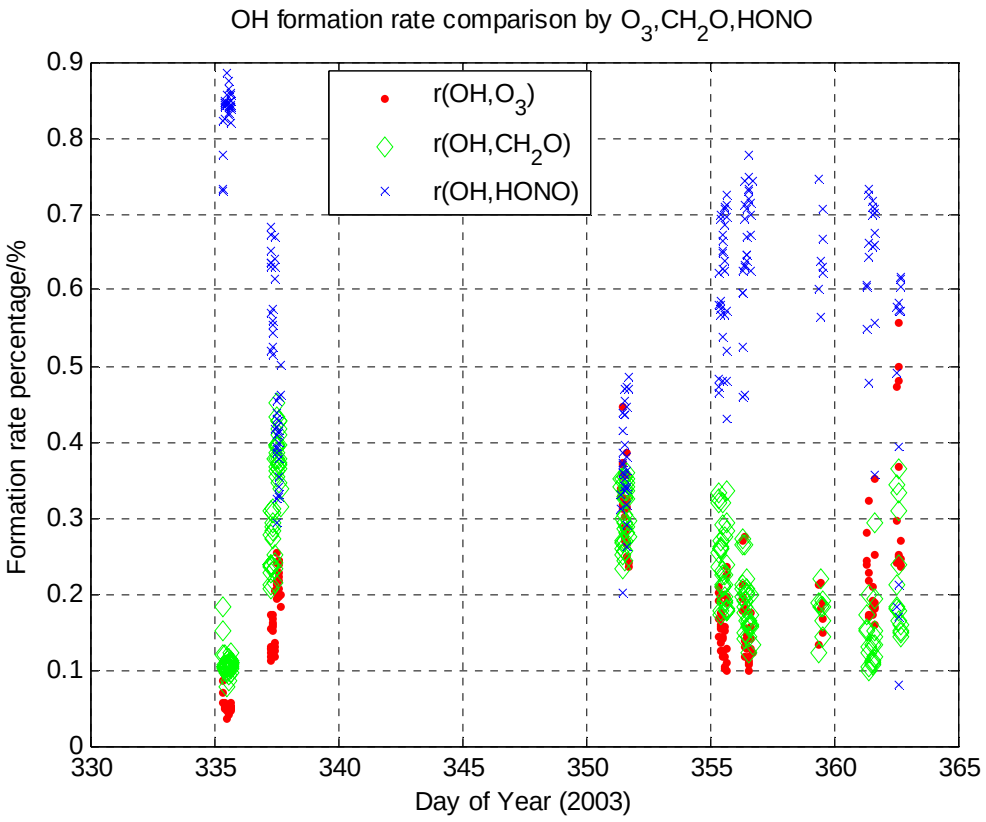

Figure 4.5 OH formation rate from measured O_3, CH_2O and HONO. HONO is clearly the dominant OH source compared with HCHO or O_3. The HONO formation rate for OH ranges from 8% to 89% with a mean value of 59%.

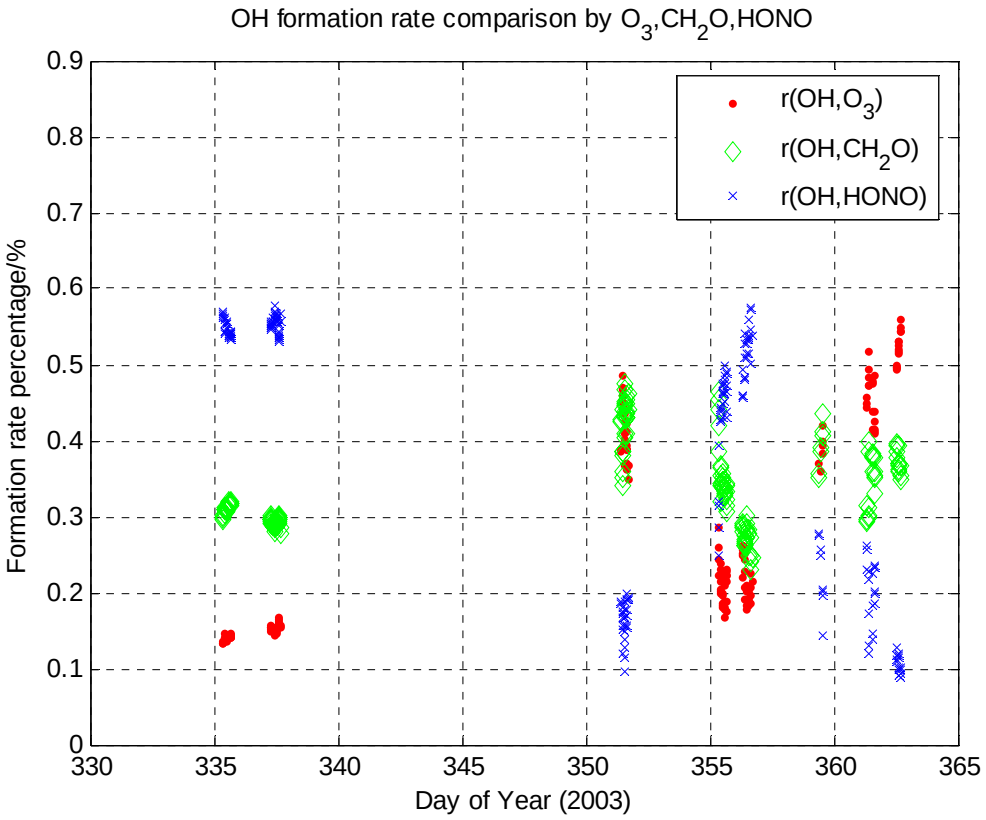

Figure 4.6 OH formation rate from measured O_3 and CH_2O along with modeled HONO. HONO is a dominant OH source on Nov 30th, Dec 1st, 3rd, 21st and 22nd while a minor OH source on Dec 15th, 17th, 25th, 27th and 28th. The HONO formation rate for OH ranges from 9% to 58% with a mean value of 40%.

4.3 Gas phase model of ANTCI 2003 data summary

The ANTCI 2003 measurements confirm the high N oxides observed previously in ISCAT 1998 and 2000. Both the LIF and MC/IC techniques observed enhanced but inconsistent HONO. Most of the MC/IC observations were at 80cm but on two days at 10 m. The ten meters MC/IC observations were higher than the LIF observations by a factor of 7.2±2.3 in the median. HONO as measured by both techniques follow NO levels and scale inversely with boundary layer height (Liao et al., 2006b). As in ISCAT 2000, the abundance of both HONO measurements exceeds the model predictions, with

LIF higher than the model by a factor of 1.92±0.67. We speculate that there may be a missing snow source term of HONO from the photolysis of snowpack NO_3^- and estimate its value based on the differences between modeled and observed HONO. Our observed HONO are not high enough to significantly influence the NO_x budget, but will increase the modeled HO_x over-prediction by 28%±15% and lead to a dramatic over-prediction of measured OH by 157%±35%. Given the short lifetime of HONO, these differences are hard to reconcile with observed low OH levels unless there is a significant missing HO_x sink in the model. It appears, however, that HONO competes with O_3 and HCHO as the dominant source of OH at South Pole. Air snowpack modeling will clarify the possible snow HONO source.

CHAPTER FIVE

AIR-SNOWPACK MODELING OF HONO

5.1 Overview of the snowpack model

Current research in polar snow chemistry focuses on the chemical and physical transfer processes that control the concentrations and fluxes of the atmospheric components. Understanding the transfer processes is essential to snow chemistry. To the best of the author's knowledge, models for investigating snow chemistry to date have only include hydrogen peroxide by McConnell et al. (1998) and formaldehyde by Hutterli et al. (1999). They use parameterizations to relate gas concentrations in the ice to those in the firn air (Domine et al., 2007).

The boundary layer is ubiquitously stable in polar region, due to the combined effects of the infra-red properties and albedo of the snow and low sun angle (Anderson and Neff, 2007). The lack of diurnal radiation variations during ANTCI 2003 makes the stable boundary layer condition with suppressed vertical mixing more obvious at South Pole than at other polar locations (Helmig et al., 2007). This causes snowpack emissions at South Pole to accumulate to higher mixing ratios than other polar sites.

Photochemical production of HONO has been reported as products of nitrate photolysis in natural and artificial snow (Honrath et al., 1999, 2000). Sampling of HONO 30 cm below the snow surface is much higher than 10 cm below the snow surface (Jacobi et al., 2004). Photolysis of nitrate alone can't explain the measured high concentration of ambient HONO because there is hardly any actinic flux 30 cm deep in the snow. We propose the following mechanism for snowpack emission of HONO:

$$NO_{3\,(aq)}^{-} + h\nu \rightarrow NO_2 + O^{-}_{(aq)}$$
$$2NO_2 + H_2O_{(aq)} \rightarrow NO_{2(aq)}^{-} + NO_{3\,(aq)}^{-} + 2H^{+}_{(aq)} \qquad (5.1\text{-}1)$$
$$NO_{2\,(aq)}^{-} + H^{+}_{(aq)} \rightleftharpoons HONO_{(aq)} \xleftrightarrow{Henry'sLaw} HONO_{(gas)}$$

Photolysis of nitrate generates NO_2 in the QLL which can easily escape to the interstitial air due to its low solubility. The large surface to volume ratio of snowpack catalyzed the hydrolysis of NO_2 to generate NO_2^- in the QLL. NO_2^- is protonated to produce HONO which will be released into the gas phase. The HONO has a long life time deep below the snow surface so that the equilibrium between quasi-liquid nitrite and interstitial air HONO according to Henry's law is reached. This high interstitial air HONO is transported to the surface snow by windpumping and subsequent diffused to the ambient air. Through this transportation process, HONO concentration is reduced by photolysis. In this way, HONO concentration is bigger deep into the snowpack and its concentration is proportionally to snowpack nitrite concentration which is very sensitive to the acidity of the snowpack. Photolysis of nitrate as well as NO_2 hydrolysis could serve as the source of nitrite. We assume constant vertical profile of nitrate and nitrite concentration for the lack of measurements. We build a comprehensive 1-D model to quantify the above mentioned processes. The model comprises of wind pumping, diffusion, chemistry reaction and inter-phase transfer processes. First we describe the wind pumping and actinic flux inside the snowpack. We further discuss quasi liquid layer nitrite as a direct reason for observed high HONO above snow surface and how this high concentration HONO is transported upwards. In the end, we discuss what factors are important to quantify the snowpack HONO emission.

5.2 Air snowpack model description

5.2.1 Wind pumping

The transfer of local chemical tracers into the snow or vice versa by air flow through the snow (wind pumping) is important for snow chemistry. Snow contains varying quantities of air, the large part of this air volume will be replaced frequently due to changes of air pressure and strong winds above the surface. The snow structure and surface roughness will determine the ventilation processes. Air passing through snow can be cleansed by dry/wet deposition or be contaminated by chemical compounds released by reactions in the snow.

Waddington et al. (1996) estimated that polar snow was a collection of loose-packed ice spheres each 0.2mm in diameter, the surface area of ice grains in the upper 7cm is more than three orders of magnitude larger than the area of a smooth impenetrable surface. Therefore the snow surface may be considered to be a big chemical reaction chamber.

The rate of air flow through snow is controlled by spatial or temporal gradients in air pressure and the permeability of the snow. Intrinsic permeability K, the ability of a porous medium to allow fluid to flow through it, is defined by Darcy's Law

$$\vec{Q} = -K \frac{1}{\mu} \nabla \Psi \qquad (5.2.1\text{-}1)$$

$$\Psi = p_{air} - \rho_{air} g z \qquad (5.2.1\text{-}2)$$

$\vec{Q}$: volumetric fluid flux ($m^3m^{-2}s$);

μ : fluid viscosity ;

Ψ: the potential energy per unit fluid volume, also known as the hydraulic potential;

z : the vertical coordinate measured positive downward;

$\nabla\Psi$ comprises the air pressure gradient and the gravitational potential gradient. A typical value of K in Antarctic snow is 10^{-9} m^2, although value can easily vary by an order of magnitude. Darcy's Law is valid when the flow within the snow is linear and laminar, this is generally the case for polar snow (Cunningham and Waddington, 1993).

Ignoring the slight hydrostatic pressure gradient, air moves through snow according to Darcy's law

$$\vec{Q} = \frac{K}{\mu}\frac{\partial p'}{\partial z} \tag{5.2.1-3}$$

Where $\vec{Q}$ is volume flux of air in the vertical direction. z is the vertical coordinate with its origin at the surface of the snow and is positive downwards. The perturbation pressure p' is the difference between air pressure and the mean air pressure. According to the air mass conservation equation:

$$\frac{\partial}{\partial z}(\vec{Q}\rho) + \phi\frac{\partial \rho}{\partial t} = 0 \tag{5.2.1-4}$$

The air also obeys the ideal gas law:

$$p = \rho RT \tag{5.2.1-5}$$

Where R is the gas constant for air. From equation (5.2.1-1) to (5.2.1-5)

$$\kappa_p \frac{\partial^2 p'}{\partial z^2} = \frac{\partial p'}{\partial t} \tag{5.2.1-6}$$

$$\kappa_p = \frac{Kp_0}{\mu\phi} \tag{5.2.1-7}$$

The diffusivity κ_p for pressure perturbations is a function of snow permeability K, a typical κ_p in snow is 10 $m^2 \cdot s^{-1}$(Cunningham and Waddington, 1993).

p_0: average atmospheric pressure

Although this is the linear approximation to the actual diffusion equation for gas flow in porous media, this approach is normally taken for gas flow.

Permeability tends to increase with porosity; however, even at constant density, Shimizu (1970) showed that grain size, age, site windiness and degree, and type of post-depositional metamorphism can cause permeability to vary by a factor of ten.

In natural snow, permeability approaches zero at the depth of pore closeoff, which is the depth range over which the pores gradually close. In Antarctica this depth is typically 50-150 m (Kaspers et al., 2004). This has important implications for mixing of gases deep in the firn. However, we treat K as a constant in this dissertation because many features of snow ventilation relevant to chemical deposition can be understood in the context of uniform permeability within one meter of the snow surface.

Sastrugi are meter-scale longitudinal dunes eroded by the wind. Sastrugi are most prominent where ice-sheet surfaces are exposed to persistent strong winds from a single direction, as on the perimeter of East Antarctica. At the South Pole, the winds are weaker and more variable, and the lengths of sastrugi are typically a few meters, widths 1 m, and heights 0.1-0.5 m. Sometimes there are two or three sets of sastrugi crossing each other and forming a network of ridges (Warren et al., 1998).

A complete treatment of firn ventilation would include calculation of air flow and associated convective transport of chemical species in the atmosphere above the snow as well as within the snow. We can first estimate the atmospheric parameters controlling air pressure and chemical concentrations at the air-snow interface, then calculate air flow only within the snow. Uncertainty associated with these parameterizations of the air-

snow interface constitutes a major source of uncertainty in the calculated chemical changes caused by wind pumping.

Three sources of pressure gradients can cause wind pumping: barometric pressure variations, wind turbulence and steady wind flow over topography. Barometric pressure variations and wind turbulence are not important processes compared with topographic pumping (Colbeck, 1989).

Air pressure should be elevated over some area on the upwind face of a topographic bump due to dynamic wind pressure, and should be lowered over some area on the lee side near the crest of the bump due to the airfoil effect associated with the increased velocity. The pressure differences on the surface would induce pressure gradients and steady air flow within the bump and surrounding snow. Toyota and McConnell (2005) derived the mean 1D wind pumping speed for the Darcy's flow rate within snowpack having uniform physical properties and residing on non-porous sea-ice:

$$\bar{v} = \frac{k}{\mu}\frac{6\rho_{air}U_{10}^2}{\pi}\frac{h}{\lambda}\frac{1}{\lambda}\frac{\sqrt{\alpha^2+1}}{\alpha}\left(C_1\exp\left(-\frac{z}{\delta}\right)-C_2\exp\left(\frac{z}{\delta}\right)\right) \tag{5.2.1-8}$$

where

$$\delta = \frac{\alpha}{\sqrt{\alpha^2+1}}\frac{\lambda}{2\pi}\text{, which is the e-folding depth} \tag{5.2.1-9}$$

$$C_1 = \frac{\exp\left(\frac{H_s}{\delta}\right)}{\exp\left(\frac{H_s}{\delta}\right)+\exp\left(-\frac{H_s}{\delta}\right)} \tag{5.2.1-10}$$

$$C_2 = \frac{\exp\left(-\frac{H_s}{\delta}\right)}{\exp\left(\frac{H_s}{\delta}\right) + \exp\left(-\frac{H_s}{\delta}\right)} \qquad (5.2.1\text{-}11)$$

z : distance from the atmosphere-snowpack interface;

H_s : mean snow depth;

k : permeability;

μ : dynamic viscosity of air;

U_{10} : surface wind speed;

h : relief amplitude;

λ : relief wavelength;

α : horizontal aspect ratio of reliefs (if α < 1 then elongated in the wind direction like sastrugi);

There are no sastrugi measurements from ANTCI 2003. Here the 1994 South Pole summertime measurement data are used (Table 5.2.1-1) (Warren et al., 1998). The weighting function is assumed to be inversely proportional to the sastrugi's area (personal communication with Stephen Warren). I multiply each wind pumping speed with the respective weighting function and add them together to get the mean wind pumping speed (Figure 5.2.1-1).

Table 5.2.1-1 Dimensions of typical of summertime sastrugi at South Pole

Feature	Height, m	Length, m	Width, m	Weighting Function, %
1	0.25	15.0	4.0	0.9
2	0.20	5.4	1.8	5.3
3	0.10	8.0	1.2	5.4
4	0.25	4.0	2.0	6.5
5	0.23	2.2	1.3	18.1
6	0.09	1.1	0.9	52.4
7	0.24	6.5	0.7	11.4

The strength of the flow through the surface decreases rapidly with increasing sastrugi length, so the smaller surface features generate stronger flows. However, the flow decays more slowly with depth at longer sastrugi lengths (Figure 5.2.1-1).

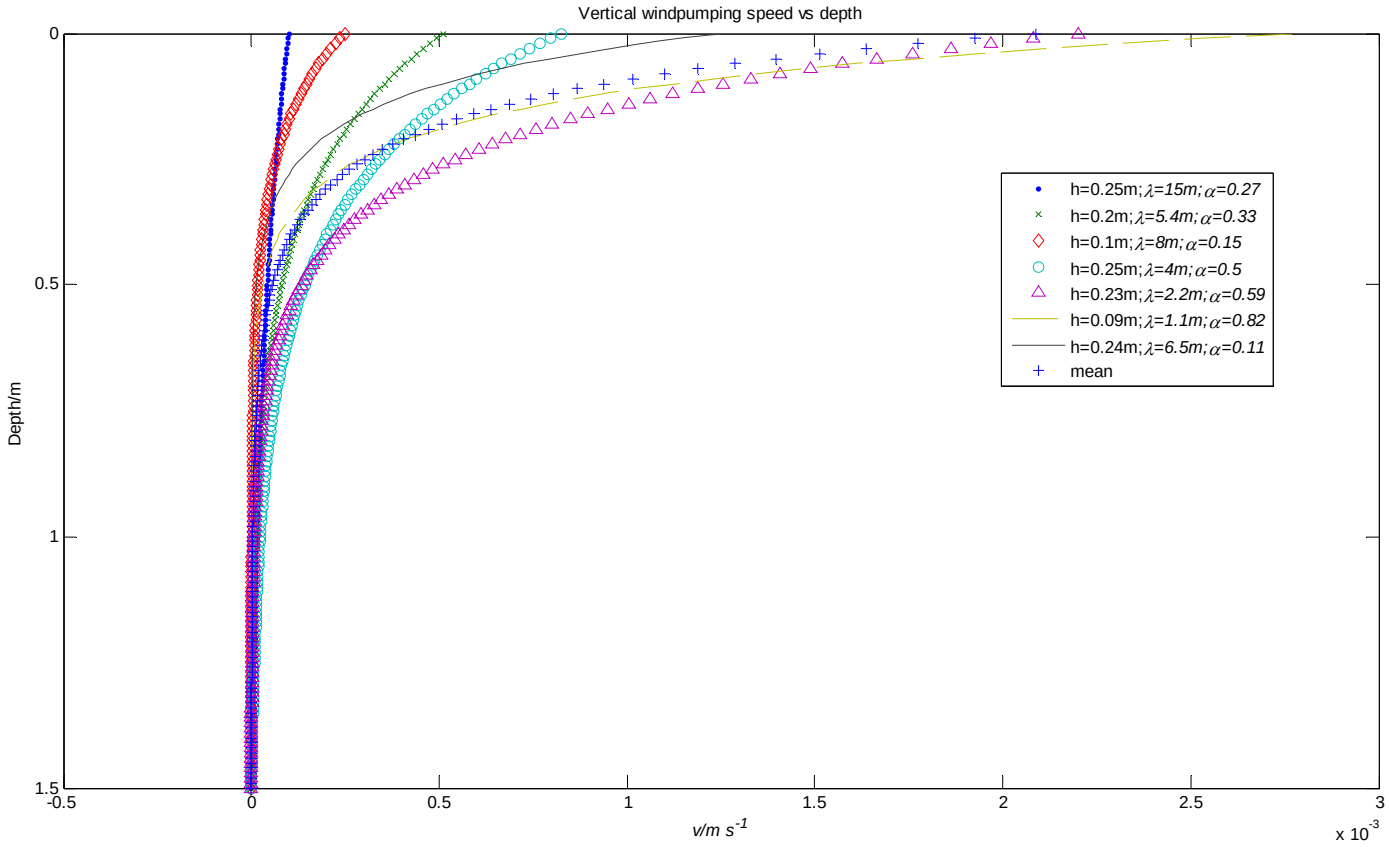

Figure 5.2.1-1 Simulation of wind pumping speed based on different dimensions of summertime sastrugi at South Pole. The surface wind speed is 5.1 m/s. The smaller surface features generate stronger flows. The e folding depth for the mean speed is 10cm.

It is easier to understand the wind pumping process through 2 D modeling (Figure 5.2.1-2). Colbeck (1989) obtained the sub-surface air flux $\vec{Q}(x,z)$, i.e.

$$\vec{Q}(x,z) = (Q_x, Q_z) = -\frac{K}{\mu}\nabla p(x,z) = \frac{2\pi}{\lambda}\frac{Kp_0}{\mu}e^{-2\pi z/\lambda}\left(\sin[2\pi x/\lambda], \cos[2\pi x/\lambda]\right)$$
$$= \frac{6\rho_{air}U_{10}^2\pi}{\lambda^2}\frac{Kh}{\mu}e^{-2\pi z/\lambda}\left(\sin[2\pi x/\lambda], \cos[2\pi x/\lambda]\right) \quad (5.2.1\text{-}12)$$

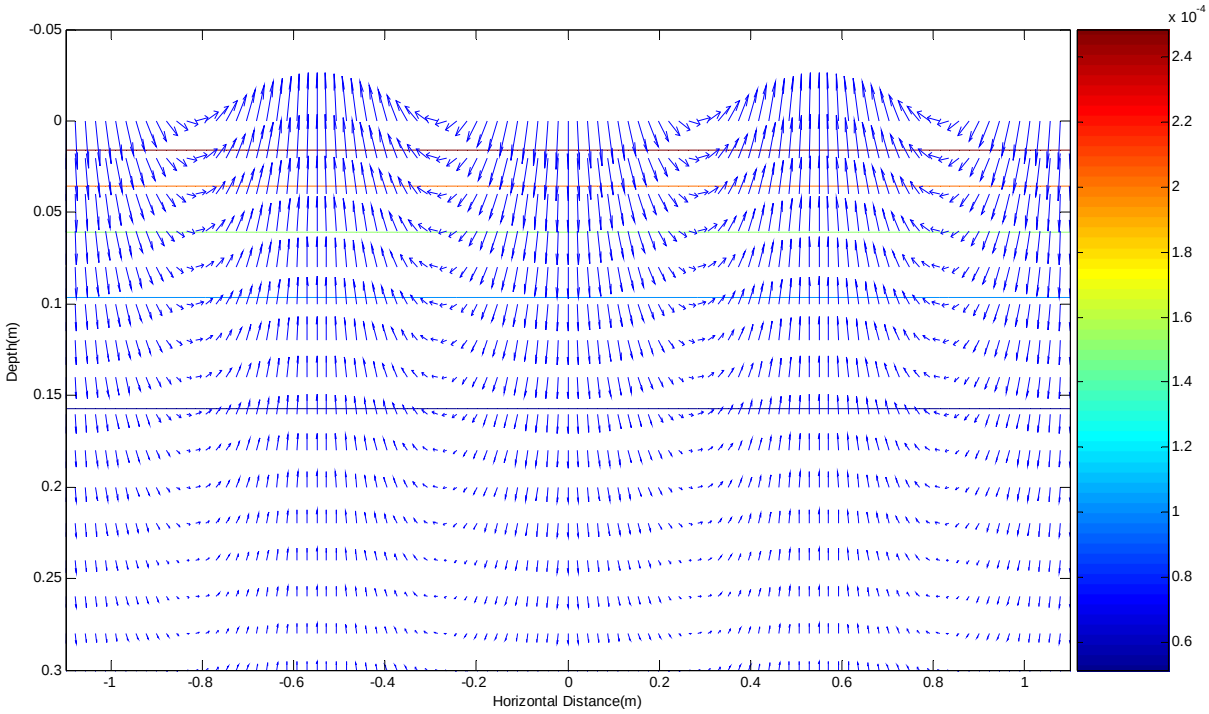

Figure 5.2.1-2 2D simulation of volumetric air flow vector (m/s) (λ=1.1m, h=0.09m)

The air flow is restricted to shallow depths by the same e-folding depth $\delta=\lambda/2\pi$. The pressure perturbation depends only on the shape h/λ of the ripples. The air flux is proportional to the pressure gradient, so it scales inversely with the actual distance between high and low pressure areas. This means that a snow surface covered by many small ripples will pump more air than a surface of equal area covered by a few large ripples of the same shape h/λ.

Cunningham and Waddington (1993) calculated the volumetric air flux within the snow:

$$\vec{Q}(x,y,z) = (Q_x, Q_y, Q_z,) = -\frac{K}{\mu}\nabla p(x,y,z)$$

$$= \frac{Kp_0}{\mu}\frac{2\pi}{\lambda}e^{-z/\delta}\left[\sin\left(\frac{2\pi}{\lambda}x\right)\cos\left(\frac{2\pi}{\alpha\lambda}y\right), \frac{1}{\alpha}\cos\left(\frac{2\pi}{\lambda}x\right)\sin\left(\frac{2\pi}{\alpha\lambda}y\right), \frac{\lambda}{\alpha}\cos\left(\frac{2\pi}{\lambda}x\right)\cos\left(\frac{2\pi}{\alpha\lambda}y\right)\right]$$

After integrating over the high-pressure portion of the bump surface for the vertical air flux component Q_z and dividing by the area $\alpha\lambda^2$ of each bump, the average volumetric air flux into the snow is

$$\overline{Q_z} = \frac{K}{\mu}\frac{p_0}{\pi^2}\frac{1}{\delta} = \frac{K}{\mu}\frac{3\rho_{air}U^2{}_{10}}{\pi^2}\frac{h}{\lambda}\frac{1}{\delta} = \frac{K}{\mu}\frac{6\rho_{air}U^2{}_{10}}{\pi}\frac{h}{\lambda}\frac{1}{\lambda}\frac{\sqrt{\alpha^2+1}}{\alpha}$$

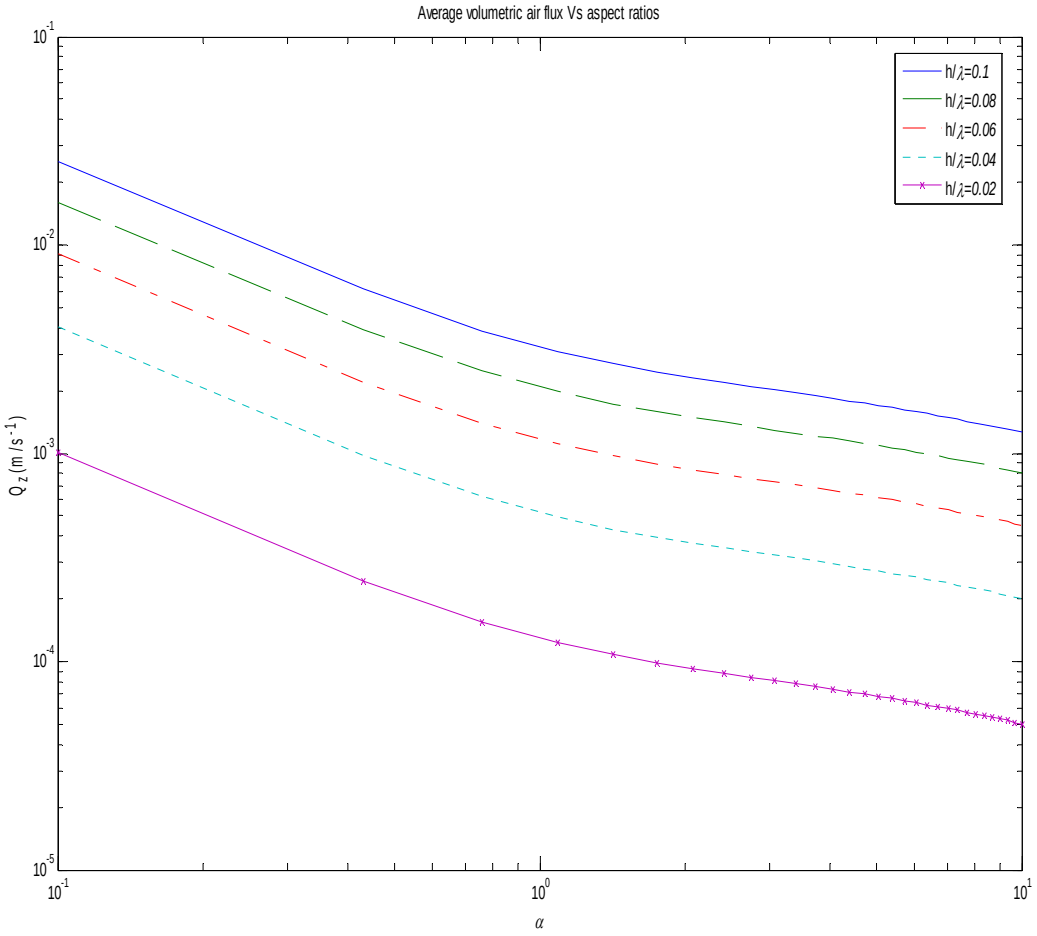

Figure 5.2.1-3 Sensitivity of volumetric air flux with aspect ratios α and h/λ

The theoretical volumetric air flux Qz at South Pole for topographic features that vary in height seasonally between 5-7.5cm, as a function of aspect ratios α and h/λ are shown in figure 5.2.1-3.

Air flow through snow occurs in response to pressure gradients at the surface that arise from the surface topography. The strength of the flow through the surface decreases rapidly with increasing sastrugi length, so the smaller surface features generate stronger flows. However, the flow decays more slowly with depth at longer sastrugi lengths.

The largest uncertainties of wind pumping arise, however, from the parameterization of the snow microtopography and the pressure variations it generates, and from the permeability of the near-surface snow (Cunningham and Waddington, 1993). Permeability and micro topography depend strongly on wind, temperature and accumulation rate, and this dependence is probably nonlinear. If there are fewer sastrugi, then the wind pumping effect would be over predicted.

5.2.2 Actinic Flux inside the snowpack

The radiative transfer inside the snow is quite similar to that inside a cloud. We applied the same numerical solution (Toon, et al., 1989) as the one used inside the cloud to calculate the actinic flux inside multiple layers of snow, but used tailored initial and boundary conditions. The snow top boundary condition is derived from the Tropospheric Ultraviolet Visible (TUV) model (Madronich and Flocke, 1998). Empirical values for absorption and scattering coefficients are parameterized so that no knowledge of the snow crystal size or shape is required (Lee-Taylor and Madronich, 2002).

We set up the snowpack as a diffusive medium with actinic flux circulating through it. A two-stream method was used for the movement. Movement of actinic flux is divided into an upward and downward component. Each of the components is approximated with a forward and backward probability function. Scattering by snow grains has the forward diffraction peak, making two-stream expansion of the probability function inadequate. To correct this, a Delta-Eddington algorithm (Joseph, et al., 1976) is used, which uses a delta function in the forward direction and a smooth scaled probability function (Equation 5.2.2-9 and 5.2.2-11). The optical depth was calculated by empirical absorption and scattering coefficients and observational snow density (Lee-Taylor and Madronich, 2002). The diffusion equation was solved numerically by defined boundary conditions (Equation 5.2.2-22 and 5.2.2-25).

Individual snow grains scatter solar radiation. The angular pattern of single scattering is described by the scattering phase function P, which gives the angular distribution of scattered energy as a function of direction. It is the fraction of radiation incident from direction Ω that is scattered into direction Ω':

$$P=P(\Omega,\ \Omega') \tag{5.2.2-1}$$

The scattering phase function is defined so that it is normalized over all scattering angles:

$$\frac{1}{4\pi}\int_{4\pi} d\Omega P(\Omega,\Omega') = 1 \tag{5.2.2-2}$$

The scattering is axisymmetric. Hence:

$$P(\Omega,\Omega') = P(\Omega\cdot\Omega') = P(\Theta) \tag{5.2.2-3}$$

Θ is the scattering angle measured from the incident direction. The normalization condition for the axially symmetric scattering phase function becomes:

$$\frac{1}{2}\int_{-1}^{1} d(\cos\Theta)P(\cos\Theta) = 1 \tag{5.2.2-4}$$

Positive Θ refers to forward scattering. Any axially symmetric scattering phase function can be written as a series of Legendre polynomials as:

$$P(\cos\Theta) = \sum_{l=0}^{\infty} \omega_l P_l(\cos\Theta) \tag{5.2.2-5}$$

where $P_l(\cos\Theta)$ is the l^{th} Legendre polynomial, normalized so that:

$$\int_{-1}^{+1} P_l(\cos\Theta)P_m(\cos\Theta)d(\cos\Theta) = \frac{2}{2l+1}\delta_{lm} \tag{5.2.2-6}$$

The two lowest moments of the scattering phase function are used to characterize single scattering by its asymmetry and by the amount scattered into the forward direction:

$$\begin{aligned} g &= \frac{1}{2}\int_{-1}^{+1} \cos\Theta P(\cos\Theta)d(\cos\Theta) \\ f &= \frac{1}{2}\int_{-1}^{+1} \frac{1}{2}[3(\cos\Theta)^2 - 1]P(\cos\Theta)d(\cos\Theta) \end{aligned} \tag{5.2.2-7}$$

where g is the asymmetry parameter and f is the forward scattered fraction. In general,

g >0 forward (Mie) scattering

g=0 isotropic or Rayleigh scattering (5.2.2-8)

g<0 backward scattering

As the snow grains are much larger than typical solar radiation wavelengths, the scattering phase functions are strongly forward peaked.

The Eddington approximation truncates the scattering phase function (Equation 5.2.2-5) at its first moment (Briegleb and Light, 2007):

$$P(\cos\Theta) \approx 1 + 3g^* \cos\Theta \tag{5.2.2-9}$$

g* is related to the asymmetry parameter g:

$$g^* = \frac{g - f}{1 - f} \tag{5.2.2-10}$$

Equation (5.2.2-9) cannot represent the strong forward peak in realistic scattering. One can modify the phase function by a δ-function:

$$P(\cos\Theta) \approx 2f\delta(1 - \cos\Theta) + (1 - f)(1 + 3g^* \cos\Theta) \tag{5.2.2-11}$$

In calculating the direct-beam radiation multiply scattered by each layer, the optical properties of the radiatively active components above this layer must first be combined into a single set. The resulting total optical depth τ which is the product of absorption coefficient and depth, effective single-scattering albedo ω_0 which is the ratio of scattering to extinction (absorption plus scattering), and effective asymmetry factor g are defined by the summations

$$\tau_n = \sum_{1}^{n-1} \tau_i \tag{5.2.2-12}$$

$$(\omega_0 \tau)_n = \sum_{1}^{n-1} (\omega_0)_i \tau_i \tag{5.2.2-13}$$

$$(g\omega_0\tau)_n = \sum_1^{n-1} g_i(\omega_0)_i \tau_i \tag{5.2.2-14}$$

The delta-scaling is used to account for the strong forward scattering of snow grains by redefining the asymmetry factor, optical depth, and single-scattering albedo, which is given by the following equations:

$$\begin{aligned} \tau' &= (1-\omega_0 g^2)\tau \\ \omega_0' &= \frac{(1-g^2)\omega_0}{1-\omega_0 g^2} \\ g' &= \frac{g}{1+g} \end{aligned} \tag{5.2.2-15}$$

Consider a diffusion domain where the directional dependence of multiple scattering events is largely lost, the upward and downward flux (F^+ and F^-) densities must be related to these fluxes as well as to the direct downward flux from the sun. The multiple scattering and absorption in the snowpack can be simplified to two-stream equations:

$$F_n^{+}(\tau) = Y_{1n}\left\{\exp[-\lambda_n(\tau_n-\tau)] + \Gamma_n \exp(-\lambda_n\tau)\right\} + Y_{2n}\left\{\exp[-\lambda_n(\tau_n-\tau)] - \Gamma_n \exp(-\lambda_n\tau)\right\} + C_n^{+}(\tau)$$

$$F_n^{-}(\tau) = Y_{1n}\left\{\Gamma_n \exp[-\lambda_n(\tau_n-\tau)] + \exp(-\lambda_n\tau)\right\} + Y_{2n}\left\{\Gamma_n \exp[-\lambda_n(\tau_n-\tau)] - \exp(-\lambda_n\tau)\right\} + C_n^{-}(\tau)$$

(5.2.2-16)

τ is the optical depth at any point within a layer. τ_c is the cumulative optical depth of layers above layer n and Y_{1n}, Y_{2n} are determined by boundary conditions, while k and Γ depend upon the form of the two-stream equation used:

$$k = (\gamma_1^2 - \gamma_2^2)^{1/2} \tag{5.2.2-17}$$

$$\Gamma = \frac{\gamma_2}{\gamma_1 + k} = \frac{\gamma_1 - k}{\gamma_2} \tag{5.2.2-18}$$

$$C^+(\tau) = \frac{\omega_0 \pi F_s \exp[-(\tau_c + \tau)/\mu_0][(\gamma_1 - 1/\mu_0)\gamma_3 + \gamma_4\gamma_2]}{\lambda^2 - 1/\mu_0^2} \tag{5.2.2-19}$$

$$C^-(\tau) = \frac{\omega_0 \pi F_s \exp[-(\tau_c + \tau)/\mu_0][(\gamma_1 + 1/\mu_0)\gamma_4 + \gamma_2\gamma_3]}{\lambda^2 - 1/\mu_0^2} \tag{5.2.2-20}$$

C^+ and C^- are the direct upward and downward solar term. $\gamma_1, \gamma_2, \gamma_3, \gamma_4$ are appropriate weighting coefficients related to multiple scattering events. The coefficients depend on the particular form of the two-stream equation. In the case of Delta Eddington scheme, the auxiliary definitions are:

$$\begin{aligned}
\gamma_1 &= (1/4)[7 - \omega_0'(4 + 3g')] \\
\gamma_2 &= -(1/4)[1 - \omega_0'(4 - 3g')] \\
\gamma_3 &= (1/4)(2 - 3g'\mu_0) \\
\gamma_4 &= 1 - \gamma_3
\end{aligned} \tag{5.2.2-21}$$

For the upper boundary condition at the top of the atmosphere, the downward diffuse flux equals any diffuse flux which may be incident.

$$F_1^-(0) = F_0^-(0) \tag{5.2.2-22}$$

For the layer between the top layer and the bottom layer, the upward and downward fluxes are continuous

$$F_n^+(\tau = \tau_n) = F_{n+1}^+(\tau = 0) \tag{5.2.2-23}$$

$$F_n^-(\tau = \tau_n) = F_{n+1}^-(\tau = 0) \tag{5.2.2-24}$$

τ_n is the total optical depth of the *n*th layer.

For the bottom layer of the snow, the upward flux is 0

$$F_N^+(\tau_N) = 0 \tag{5.2.2-25}$$

Put the boundary layer condition into $F_n^+(\tau), F_n^-(\tau)$ and solve for Y_{1n}, Y_{2n} at different depth by standard tridiagonal solution method.

The total actinic flux at *n*th layer is

$$F_n = (\frac{1}{\mu_1})\{Y_{1n}[(1+\Gamma_n)(1+\exp(-\lambda_n\tau_n))] + Y_{2n}[(1+\Gamma_n)(1-\exp(-\lambda_n\tau_n))] + C_n^+(\tau_n) + C_n^-(\tau_n)\}$$
$$+ F_{dir\_surface}\exp[-(\tau_c + \tau_n)/\mu_0] \tag{5.2.2-26}$$

Where

$$\mu_1 = (1-\omega_0)/(\gamma_1 - \gamma_2) \tag{5.2.2-27}$$

$F_{dir\_surface}$ is the direct actinic flux on top of snow surface which is the output of the TUV model.

The photolysis frequency, *J*, is determined for species *x*, by evaluating the following convolution product over all wavelengths:

$$J_x = \int \sigma_x(\lambda)\Phi_x(\lambda)F(\lambda)d\lambda \tag{5.2.2-28}$$

Here, $F(\lambda)$ is the spectral actinic flux (radiant flux density incident onto a spherical area) and $\sigma(\lambda)$ and $\Phi(\lambda)$ are, respectively, the absorption cross-section and the photodissociation quantum yield of the molecule *x*.

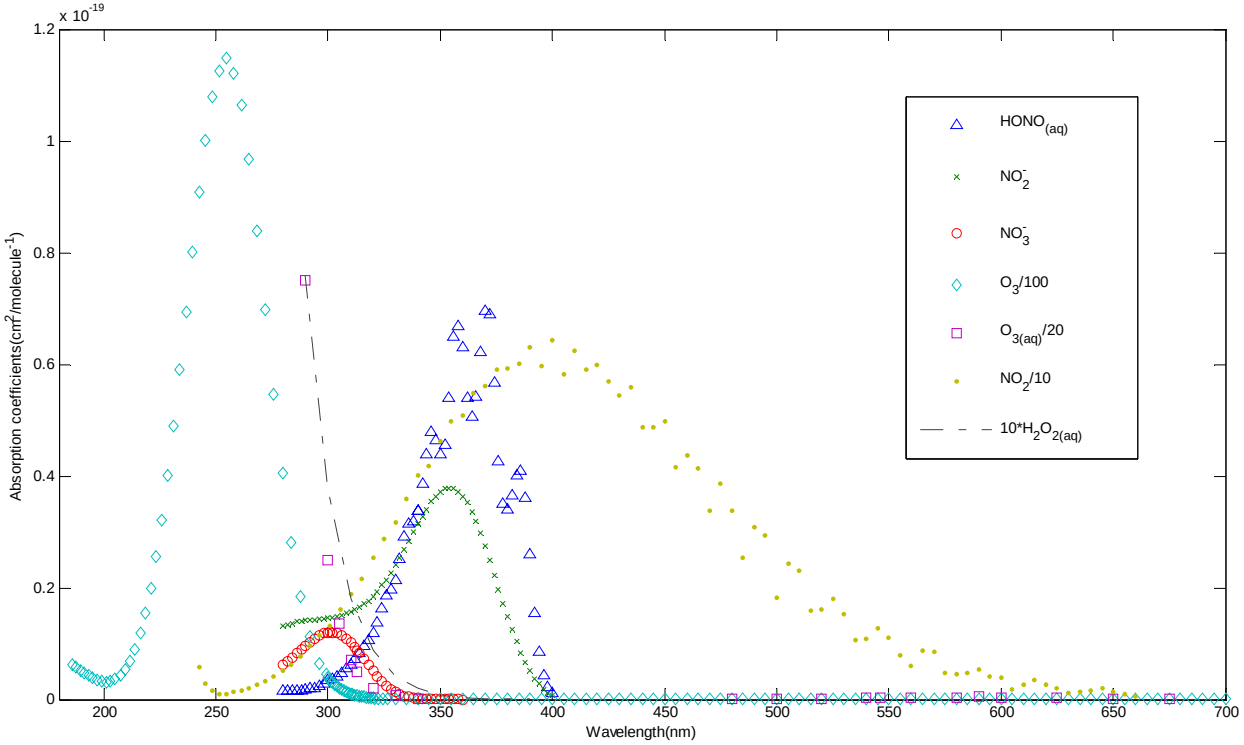

Figure 5.2.2-1 Absorption coefficients of various species

Table 5.2.2-1 References for the quantum yield and cross section

	$HONO_{(aq)}$	NO_2^-	NO_3^-	$H_2O_{2(aq)}$	$O_{3(aq)}$	O_3	NO_2
Quantum yield	(Fischer and Warneck, 1996)	(Fischer and Warneck, 1996);(Zellner, et al., 1990)	(Chu and Anastasio, 2003); (Warneck and Wurzinger, 1988);(Zellner, et al., 1990); (Bartels-Rausch and Donaldson, 2006)	(Zellner, et al., 1990)	(Finlayson-Pitts and Pitts, 1986)	(Sander et al., 2006)	(Sander et al., 2006)
Cross section	(Fischer and Warneck, 1996)	(Fischer and Warneck, 1996)	(Burley and Johnston, 1992)	(Graedel and Weschler, 1981)	(Graedel and Weschler, 1981)	(Sander et al., 2006)	(Sander et al., 2006)

The TUV model is used to parameterize the atmospheric conditions. Cloud optical density, and O_3 and NO_2 columns are careful chosen so that the J value of O^1d and NO_2 from TUV output match those derived by the Biospherical Company using an Eppley radiometer during ANTCI 2003. Figure 5.2.2-2 and 5.2.2-3 are simulated actinic flux at the top of atmosphere and the snow surface on Dec 21st, 2003.

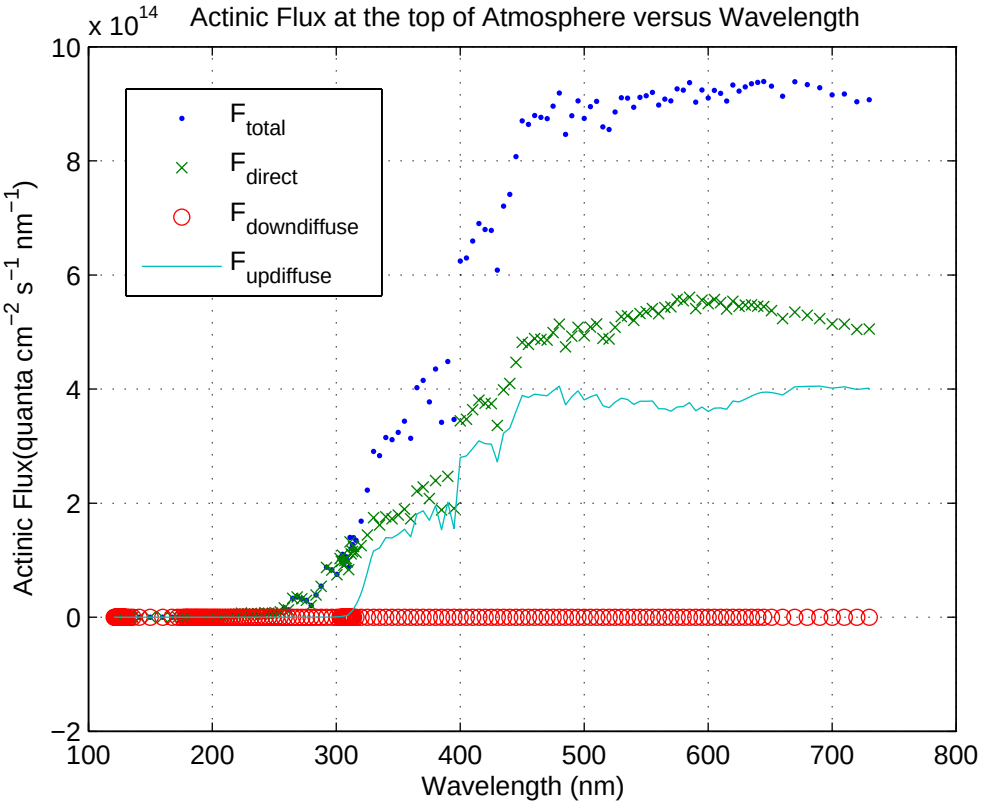

Figure 5.2.2-2 Actinic Flux simulation at the top of atmosphere on Dec 21st, 2003 at South Pole by TUV model.

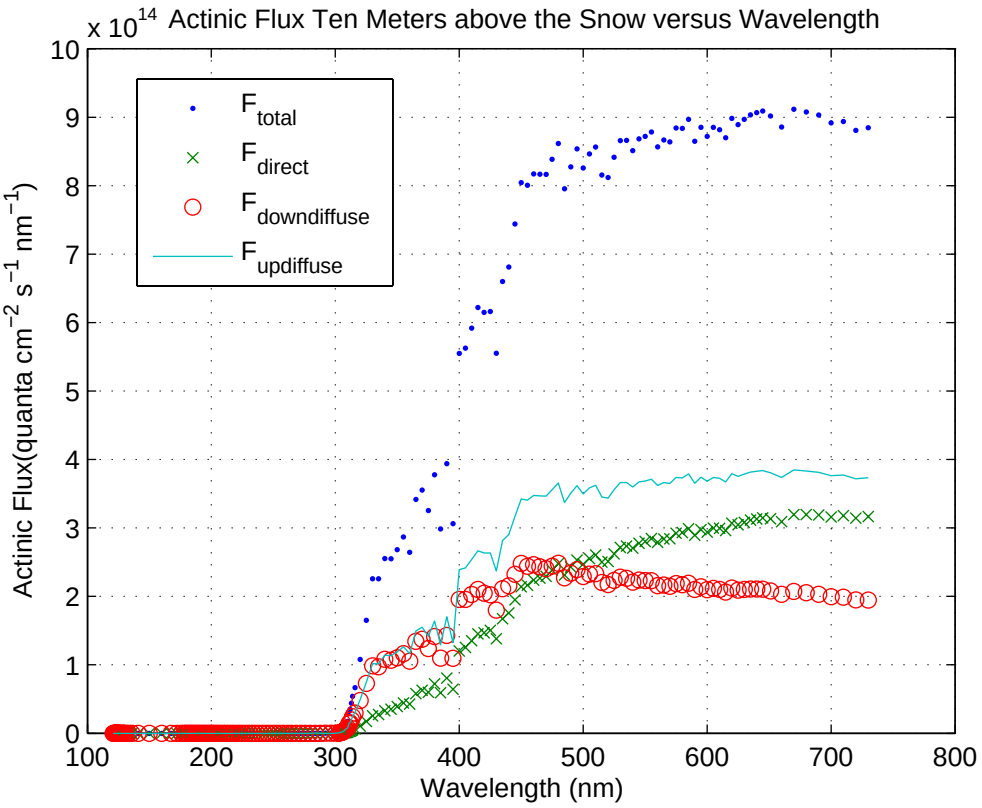

Figure 5.2.2-3 Actinic Flux simulation ten meters above the snow surface on Dec 21st, 2003 at South Pole by TUV model, parameters were calibrated by reported J_{NO2} and J_{O1d} from the Biospherical Company.

The snow surface actinic flux is used as the top boundary condition for the snowpack actinic flux simulation (Figure 5.2.2-4 to 5.2.2-7). The downwelling component is bigger than upwelling component from the snow surface to 9.5 cm down (Figure 5.2.2-4). The difference is due to the direct actinic flux. After the 9.5 cm, all incident light is diffuse which means the downwelling component and upwelling component are the same in magnitude.

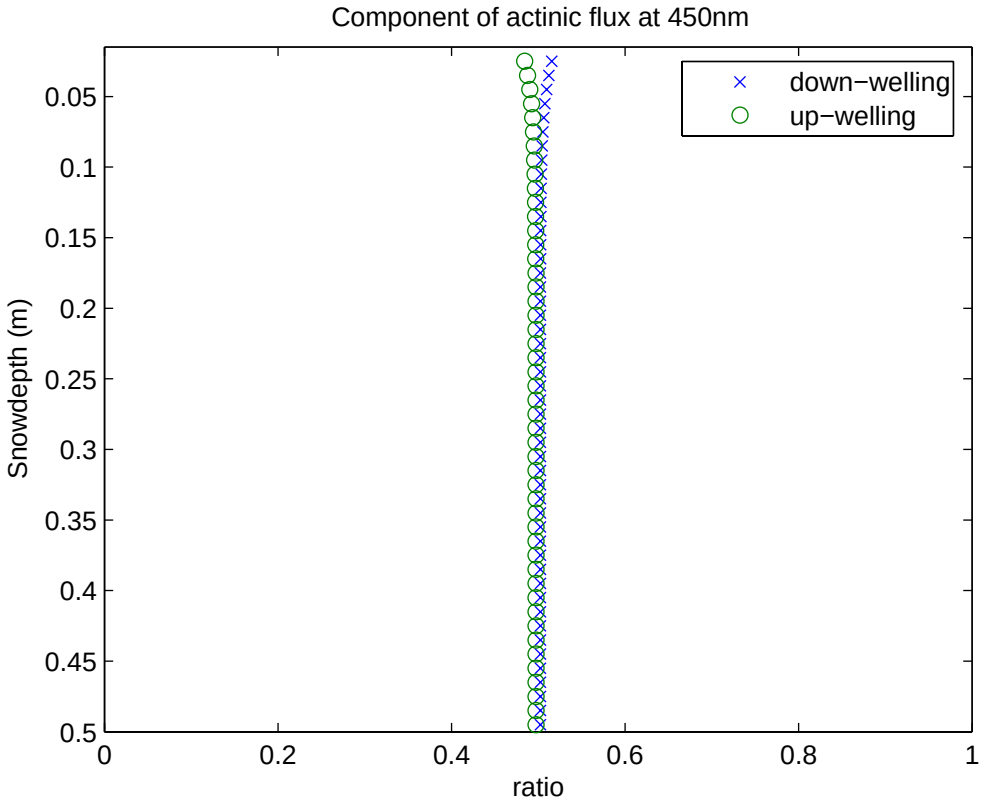

Figure 5.2.2-4 The component of actinic flux at 450nm with snow depth.

Figure 5.2.2-5 shows the total actinic flux changing with snowpack and wavelength. The total actinic flux peaks around 450 nm because the snow/ice has minimum absorption at this wavelength (Grenfell and Perovich, 1986; Perovich and Govoni, 1991). The structure between 300 nm and 400 nm is inherited from the incoming actinic flux at the snow surface (Figure 5.2.2-2 and figure 5.2.2-3).

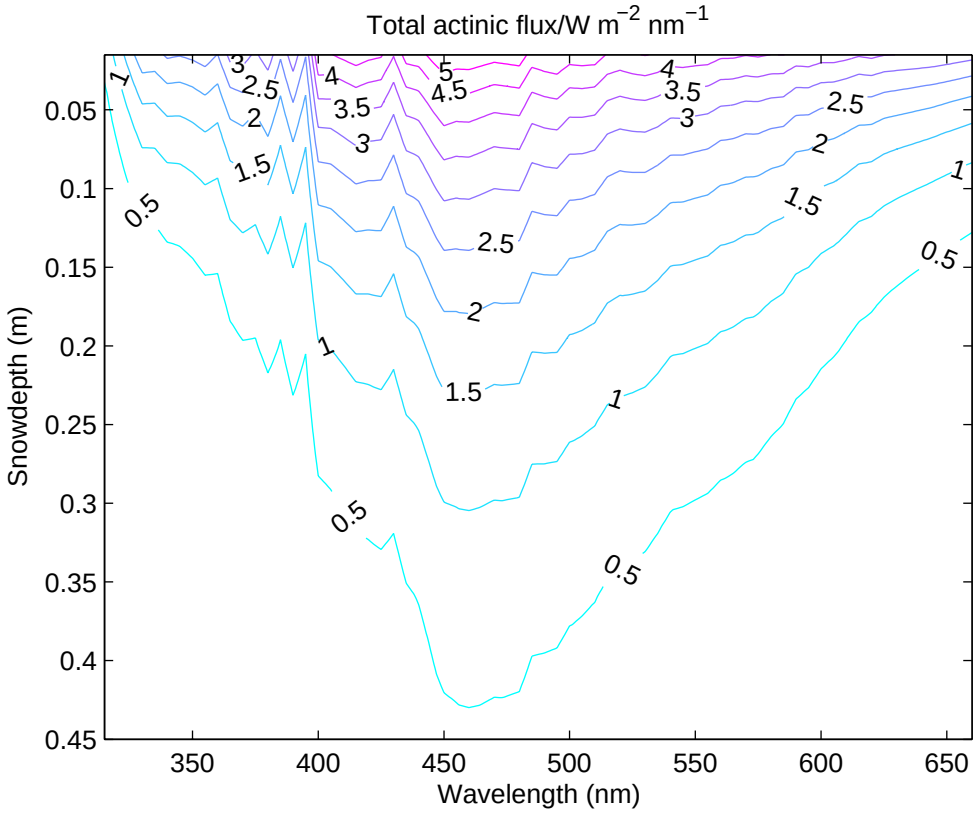

Figure 5.2.2-5 Simulation of actinic flux with snow depth and wavelength. Conditions are: mass-specific scattering coefficient σ_{scatt}=22.5 m^2 kg^{-1}, snow density ρ=0.3 g cm^{-3}, solar zenith angle θ=68º, no soot.

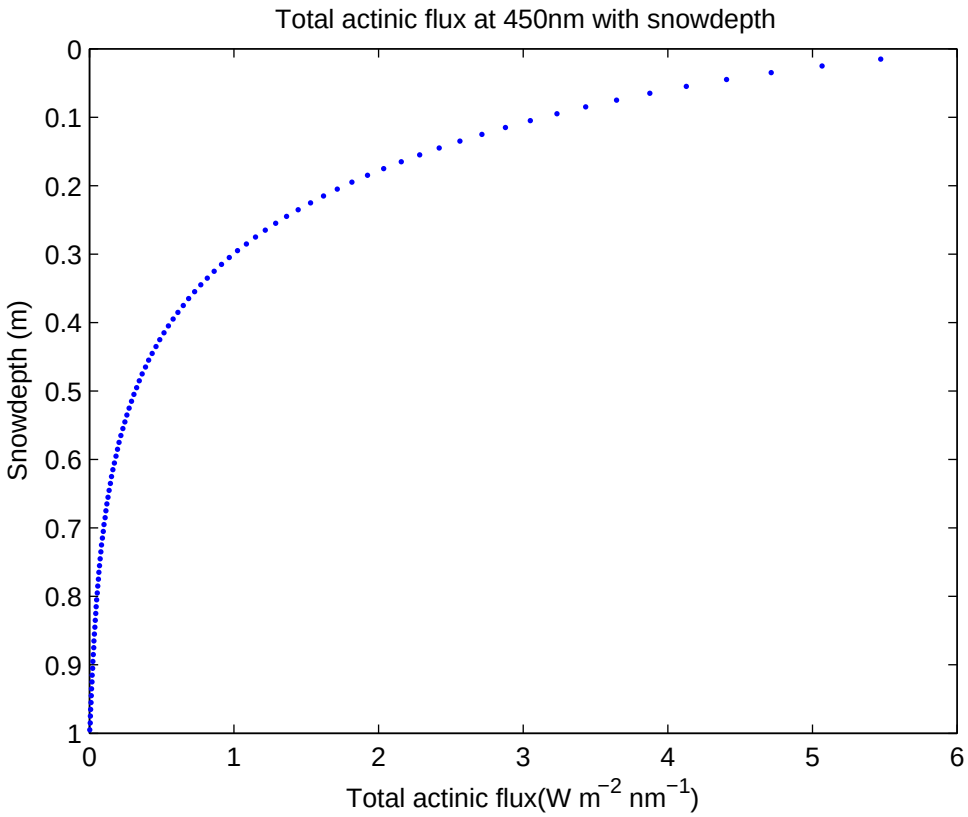

Figure 5.2.2-6 Total actinic flux with snow depth at 450nm. The e folding depth is 16cm and e^2 depth is 33cm.

Using the snowpack radiative model, we simulate the photolytic destruction of nitrate (Figure 5.2.2-7).

$$NO_3^- \xrightarrow{h\upsilon} NO_2^- + O(^3P) \xrightarrow{H^+} HONO(g) \qquad (5.2.2\text{-}29)$$

The quantum yield for HONO is $(3.8 \pm 0.6) \cdot 10^{-4}$ (Bartels-Rausch and Donaldson, 2006).

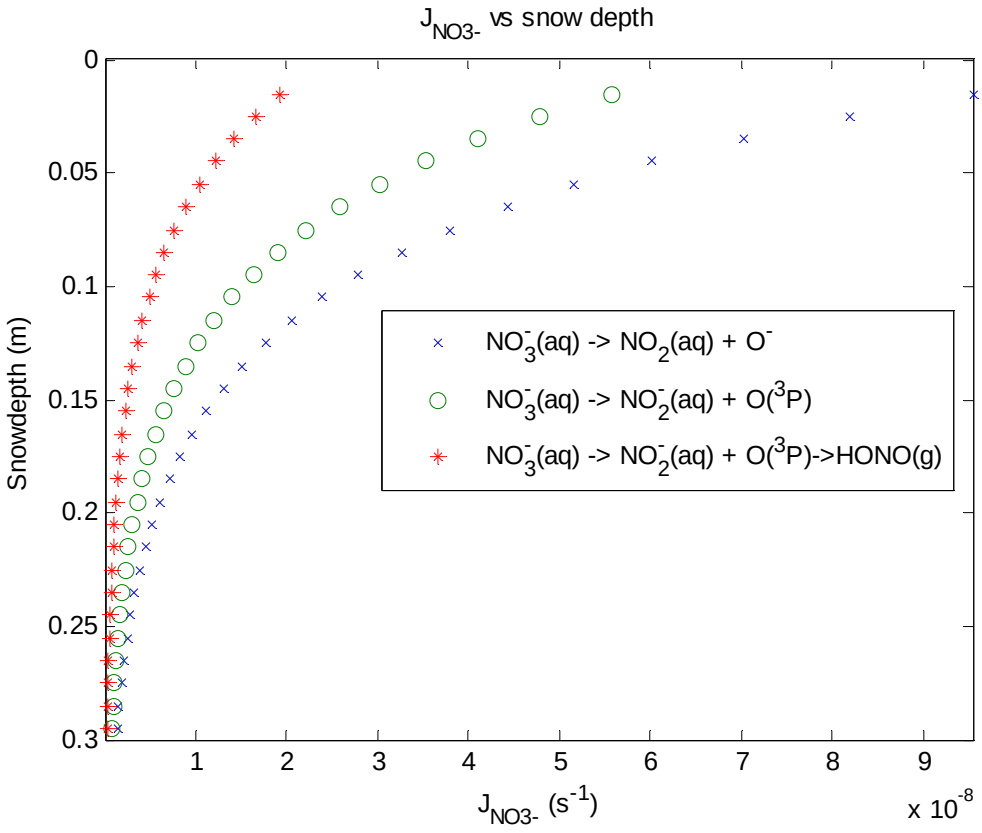

Figure 5.2.2-7 J_{NO3^-} with snow depth. The e folding depth is 6cm and e^2 depth is 16cm.

5.2.3 Master equation and model results

The quasi-liquid layer (QLL) is a disordered layer of ice at the surface that has chemical properties closer to water than solid crystalline ice (Boxe, 2005). Ionic solutes are efficiently excluded from the ice matrix upon freezing, and in the presence of solutes it is not clear whether the surface layer of ice is a true liquid or a quasi-liquid. There are no reaction data for the QLL phase reactions or for the thickness of the QLL as a function of temperature for solute-containing ices. In practice I am assuming that the surface layer is a true liquid with a significant freezing point depression and using the known aqueous phase reactions. The quasi-liquid layer thickness relative to the snow grains radius is very important to scale the bulk snow solute concentration to the QLL solute concentration.

Diffusion and ventilation are two important processes that affect the movement of trace gases within a snowpack. Diffusion is a transport process driven by both concentration and temperature gradients, where wind ventilation provides an advective transport process with interstitial air movement within the snowpack. Trace gas concentrations are also affected by in situ chemistry production/loss and gas/liquid exchange. We model interstitial HONO using the combination of one-dimensional advection-dispersion equation by McConnell et al. (1998) and multiphase model by Sportisse and Djouad (2000):

$$\frac{\partial C_g}{\partial t} = D\frac{\partial^2 C_g}{\partial z^2} - U\frac{\partial C_g}{\partial z} + Q_g - S_g - 3\frac{\lambda_m}{a}\cdot\frac{LWC}{1-LWC}\cdot\left(C_g - \frac{C_a \cdot P}{H}\cdot 10^{12}\right) \qquad (5.2.3\text{-}1)$$

where C_g/C_a are the gas/liquid phase HONO concentrations, t and z are time and depth respectively. The first two terms describe transport of gas phase HONO by dispersion

and convection. D is the dispersion, including both gas-phase molecular diffusion D_g and mechanical dispersion D_m. The mechanical dispersion is caused by advective mixing of tracer particles on the pore scale and is given by the product of the absolute value of the flow velocity field *v* and a dispersion length (generally taken as the mean pore diameter) d (Neuweiler et al., 2001). In the case of this work, d is 2mm (Waldner et al., 2004), the daily average pore velocities range from 10^{-2} to 10^{-4} m/s. D is 1.3×10^{-5} m^2/s (Ervens et al., 2003). U is the wind pumping velocity of the air in the z direction.

Q and S represent the chemical sources and sinks for gas phase HONO within the snowpack. Here I assume that HONO photolysis is the most important sink and NO_3^- photolysis is the most important source. Snowpack nitrate profiles were not measured, so the concentration of NO_3^- is assumed to be constant with snow depth, which is $NO_3^- = 2 \cdot 10^{-5}$ mol kg^{-1} snowpack concentration. The J values of nitrate and nitrite have similar behavior with depth through out snowpack, as described in section 5.2.2. Snow pit measurements by Jack Dibb of UNH show that bulk nitrite concentrations are four orders of magnitude less than that of nitrate. Here we also assume a constant concentration of nitrite with snow depth.

The transfer of molecules from the interstitial air phase to the QLL aqueous phase and vice versa is treated by the last term in equation 5.2.3-1. The net flux is the difference of the departure from Henry's law equilibrium at the surface and the reactive uptake of HONO on the snow surface. Trace gases can diffuse to the QLL or collide and stick to the surface of QLL. In the case of HONO, gas to aqueous phase diffusion is omitted because of large mass accommodation coefficient (α) of HONO (Schwartz, 1986). Mass accommodation coefficient and reversible dissolution (according to the

Henry's Law) are incorporated. LWC is the unitless liquid water content and λ_m describes the mass transfer through gas-liquid phase:

$$\lambda_m = \frac{1}{4}\alpha\bar{v} \qquad (5.2.3\text{-}2)$$

Here α is the mass accommodation coefficient; $\bar{v}$ is the mean molecular velocity; a is the snow grain radius. H stands for the Henry law constant and P is the pressure. The factor 10^{12} in equation 5.2.3-1 is used to scale to the gas phase concentration in unit of part per trillion (ppt). The following parameters are taken from Herrmann et al (2000).

Q_g = gas phase source reaction rate [ppt s^{-1}]

S_g = gas phase sink reaction rate [ppt s^{-1}]

α = mass accommodation coefficient (0.5)

a = snow crystal radius (0.001 m)

$\bar{v}$ = molecular speed $= \left(\frac{8RT}{\pi M}\right)^{1/2}$ [m s^{-1}]

M = molecular mass [kg mol^{-1}]

R = gas constant [J mol^{-1} K^{-1}]

T=temperature [K]

LWC = liquid water content [–]

(LWC=(1-porosity) ·QLL to snow volume ratio=(1-0.53) ·$2\cdot10^{-3}$ (Michalowski, et al., 2000)) $= 9.4 \cdot 10^{-4}$ vol/vol)

H = Henry's Law constant [mol L^{-1} atm^{-1}]

λ_m = gas-liquid phase transfer coefficient [s^{-1}]

The sun is visible through the summer and the constrained input data points are ten minute averages. It is reasonable to suppose the gas phase concentrations do not change in the time interval, that is $\frac{\partial C}{\partial t} = 0$. Then equation (5.2.3-1) can be reduced to an ordinary differential equation which can be solved.

The windpumping speed and actinic flux decrease sharply with the depth. Deep down the snowpack, chemical reaction rates are slow enough that the gas phase HONO reaches equilibrium with the QLL phase HONO according to Henry's Law. Due to the lack of a measured nitrite profile, here we use a constant snowpack nitrite concentration (Jack Dibb, personal communication). I use the bulk snow nitrite concentration, median value of measured snowpack pH and QLL volume ratio to estimate the aqueous phase HONO concentration. The QLL HONO concentration, atmospheric pressure, and Henry's law constant of HONO are then used to estimate the gas phase HONO concentration at deep below the snow surface, which is about 164 pptv at 30 cm below the snow surface when the boundary layer is extremely low. The measured snow surface HONO concentrations by MC/IC are too high to accommodate the current model setup.

Figure 5.2.3-1 shows the modeled HONO vertical profile inside the snowpack on Dec 17th, 21st, 22nd, 25th, 27th and 28th. HONO decreases exponentially with respect to deep boundary layer on Dec 17th, 25th, 27th and 28th and the chemical migration is large due to advective transport. On Dec 21st and 22nd, the mean boundary layer depth is only 25.55 m and the boundary layer is very stable, in the low-wind scenario the migration of HONO in the snowpack can be largely attributed to diffusive transport.

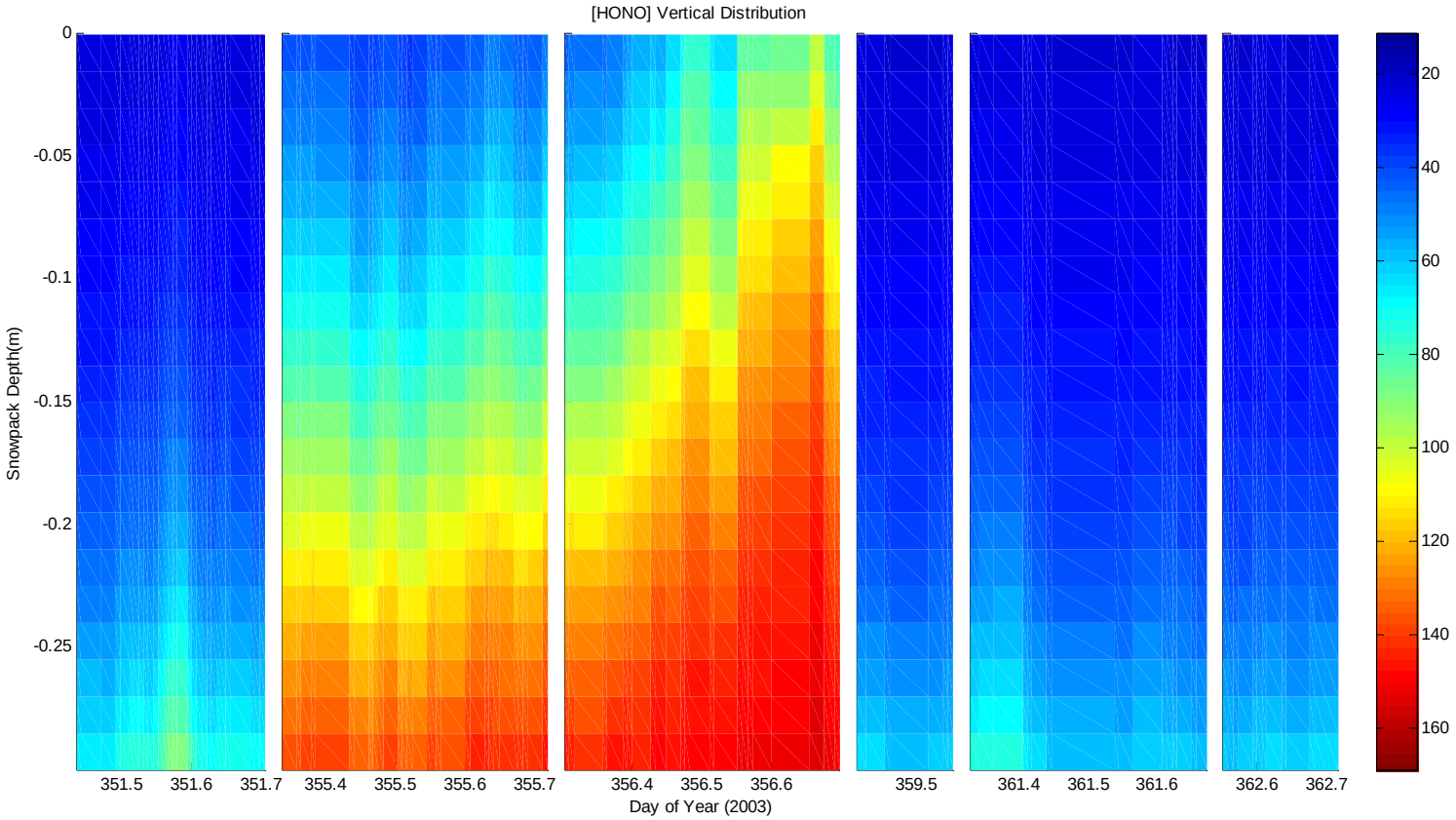

Figure 5.2.3-1. Simulation of HONO vertical profile inside the snowpack on Dec 17th, 21st, 22nd, 25th, 27th and 28th.

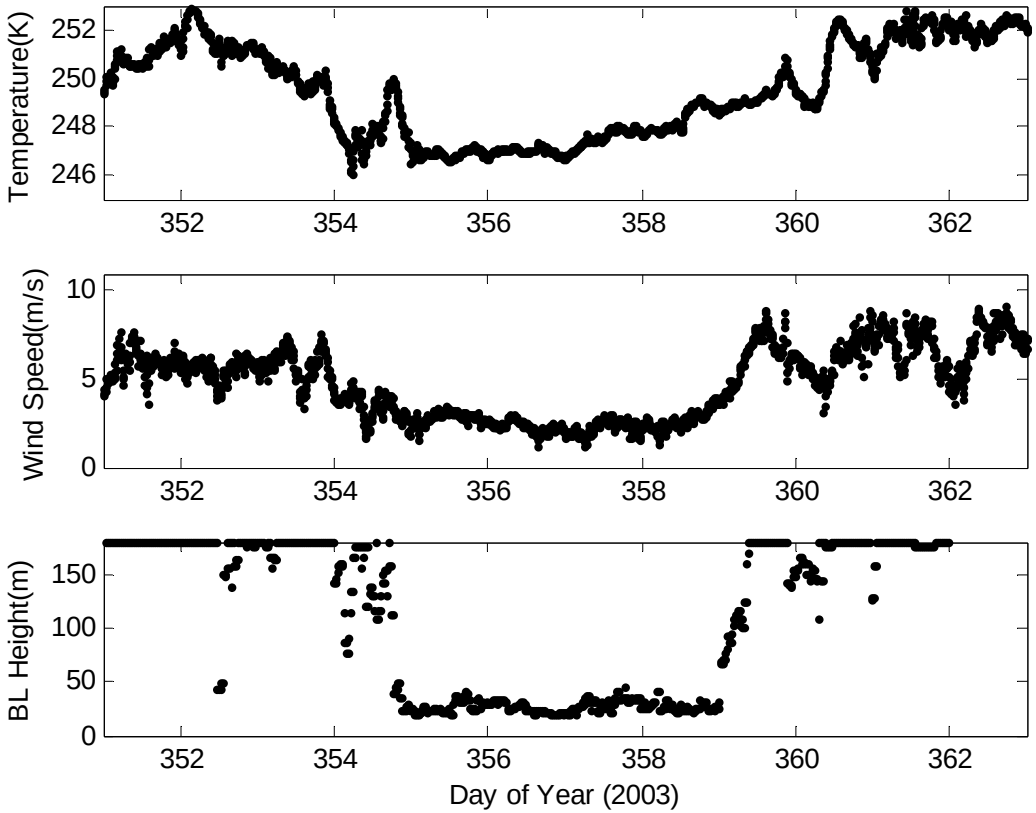

Figure 5.2.3-2. Temperature, wind speed and boundary layer height from Dec 17th to Dec 28th. They have the similar pattern in the sense that they decrease during 355 to 359 when the mean boundary layer height is 26.7 meters.

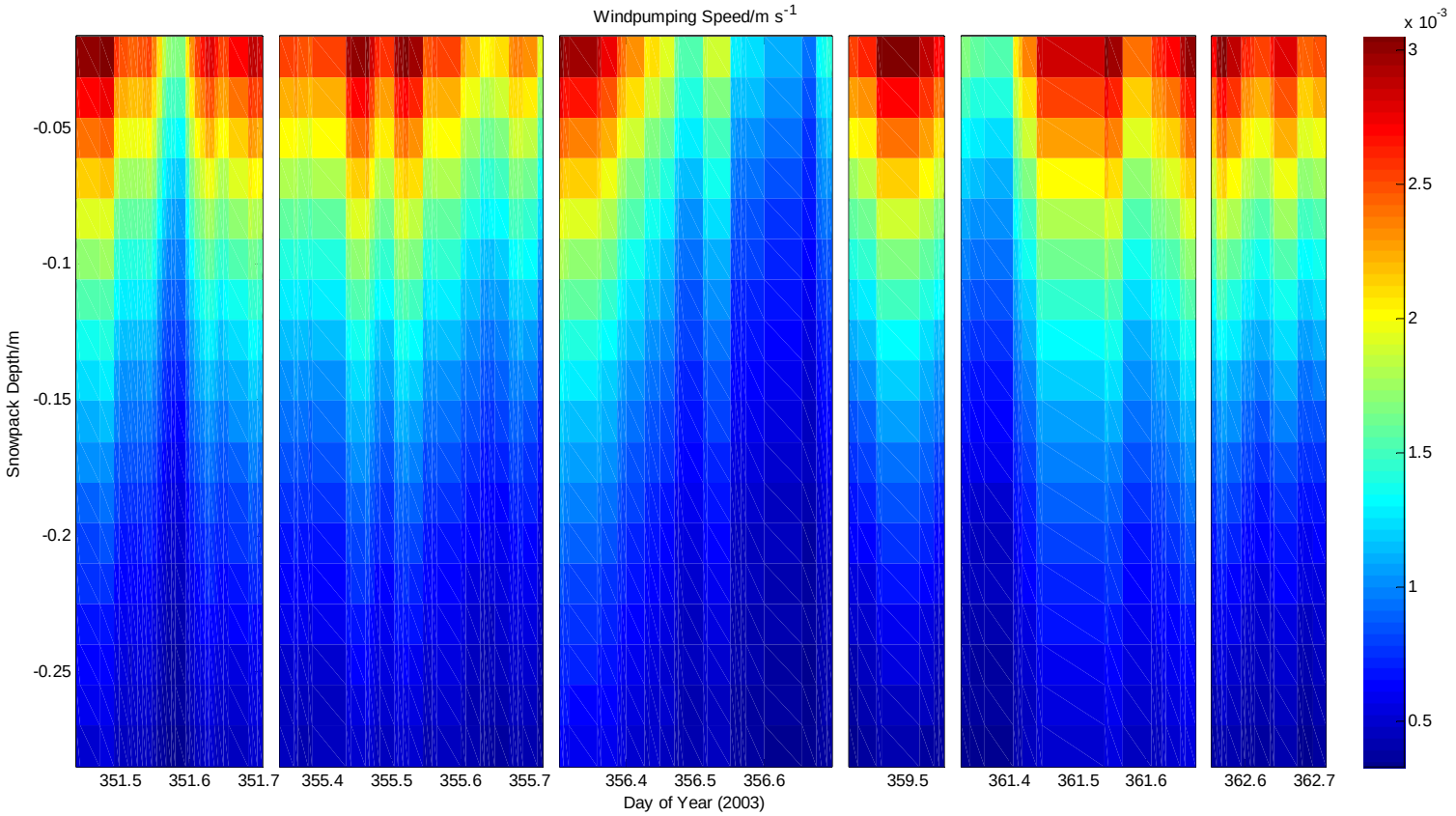

Figure 5.2.3-3. Simulation of windpumping speed from 0 m to 0.3 m below snow on Dec 17th, 21st, 22nd, 25th, 27th and 28th

The general form of the transport or mass balance equation above the snow is given by:

$$\frac{\partial C}{\partial t} = k_z \frac{\partial^2 C}{\partial z^2} - w\frac{\partial C}{\partial z} + Q - S \qquad (5.2.3\text{-}3)$$

k_z is the vertical eddy diffusion coefficient

w is the vertical advection velocity

Q is the chemical production rate

S is the chemical loss rate

The vertical eddy diffusion coefficient k_z quantifies the vertical flux of a tracer given a known concentration profile and is given by

$$k_z = 0.4 \cdot z \cdot u_* \qquad (5.2.3\text{-}4)$$

Where 0.4 is the von Karman constant, z is the height and u_* is the friction velocity. u_* is related to the surface momentum fluxes by Anderson and Neff (2007):

$$u_* = [(\overline{u'w'})^2 + (\overline{v'w'})^2]^{1/4} \qquad (5.2.3\text{-}5)$$

Turbulence mixes the trace gases vertically and horizontally. $\overline{u'w'}$ and $\overline{v'w'}$ (m^2 s^{-1}) are mean kinematic vertical turbulent fluxes. The estimated characteristic time for turbulent mixing from the snow surface to the HONO inlets at 10 m is 2.1 minutes (median values), estimated as $\tau_t = \frac{z}{\kappa \cdot u_*}$ (Yang et al., 2002). This value is less than the median HONO life time above the snow surface which is 6.6 minutes.

To simply the vertical profile, we assume steady state for time dependent solution:

$$\frac{\partial C}{\partial t} = 0$$

At steady state

$$k_z \frac{\partial^2 C}{\partial z^2} - w\frac{\partial C}{\partial z} + Q - S = 0 \qquad (5.2.3\text{-}6)$$

The model is highly constrained by measurement data, and the time interval is minutes, over this period of time, the mean vertical velocity is ~zero. I use LIF measured HONO concentrations at 10 meters as upper level boundary condition and surface snowpack model output as snow surface condition.

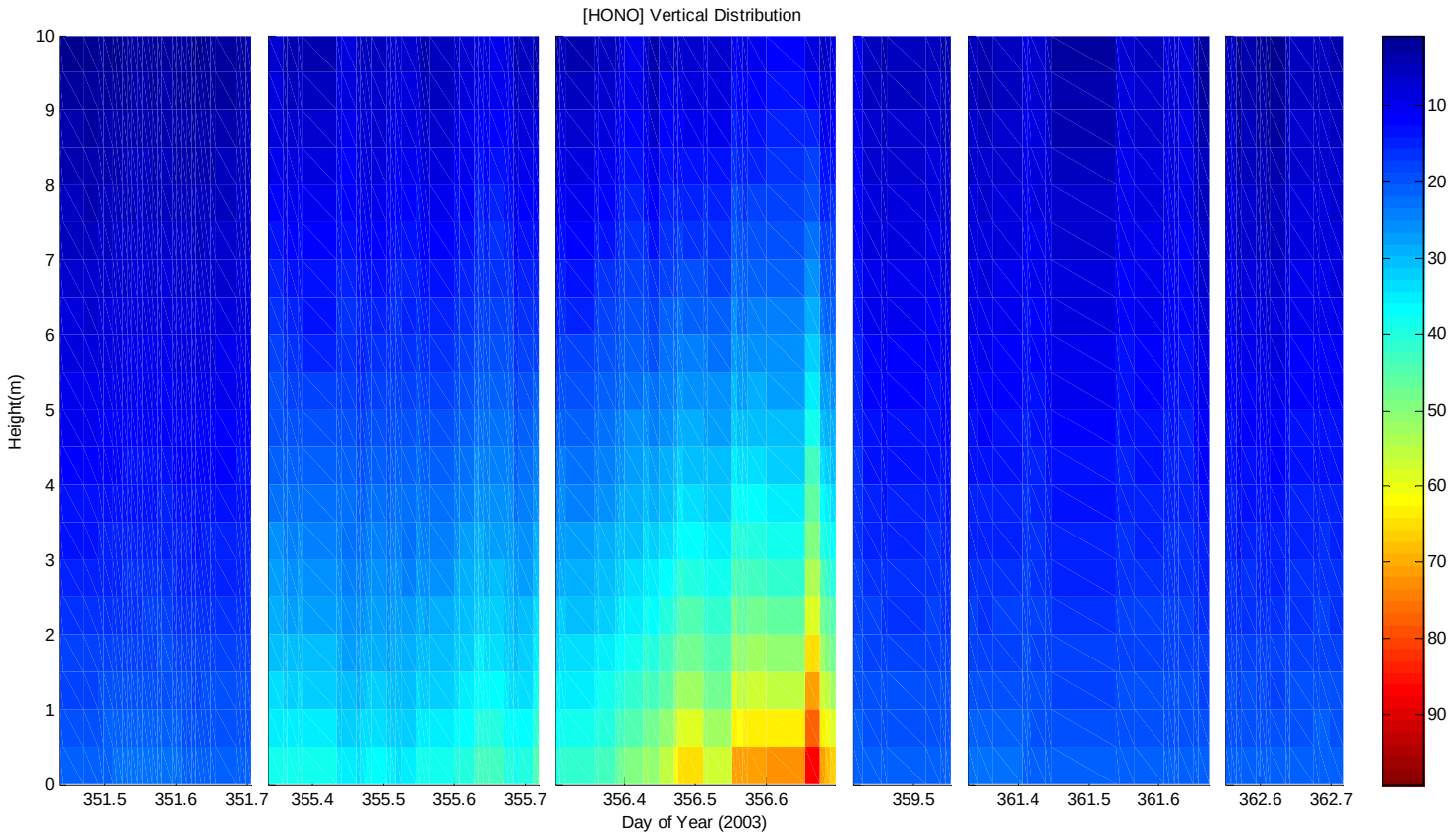

Figure 5.2.3-4. Simulation of HONO vertical profile above the snowpack on Dec 17th, 21st, 22nd, 25th, 27th and 28th. The boundary condition C (z_0) is constrained by the measured HONO by LIF and C (z_{m+1}) is from the snowpack model output, where z_0 = 10m and z_{m+1} = 0m.

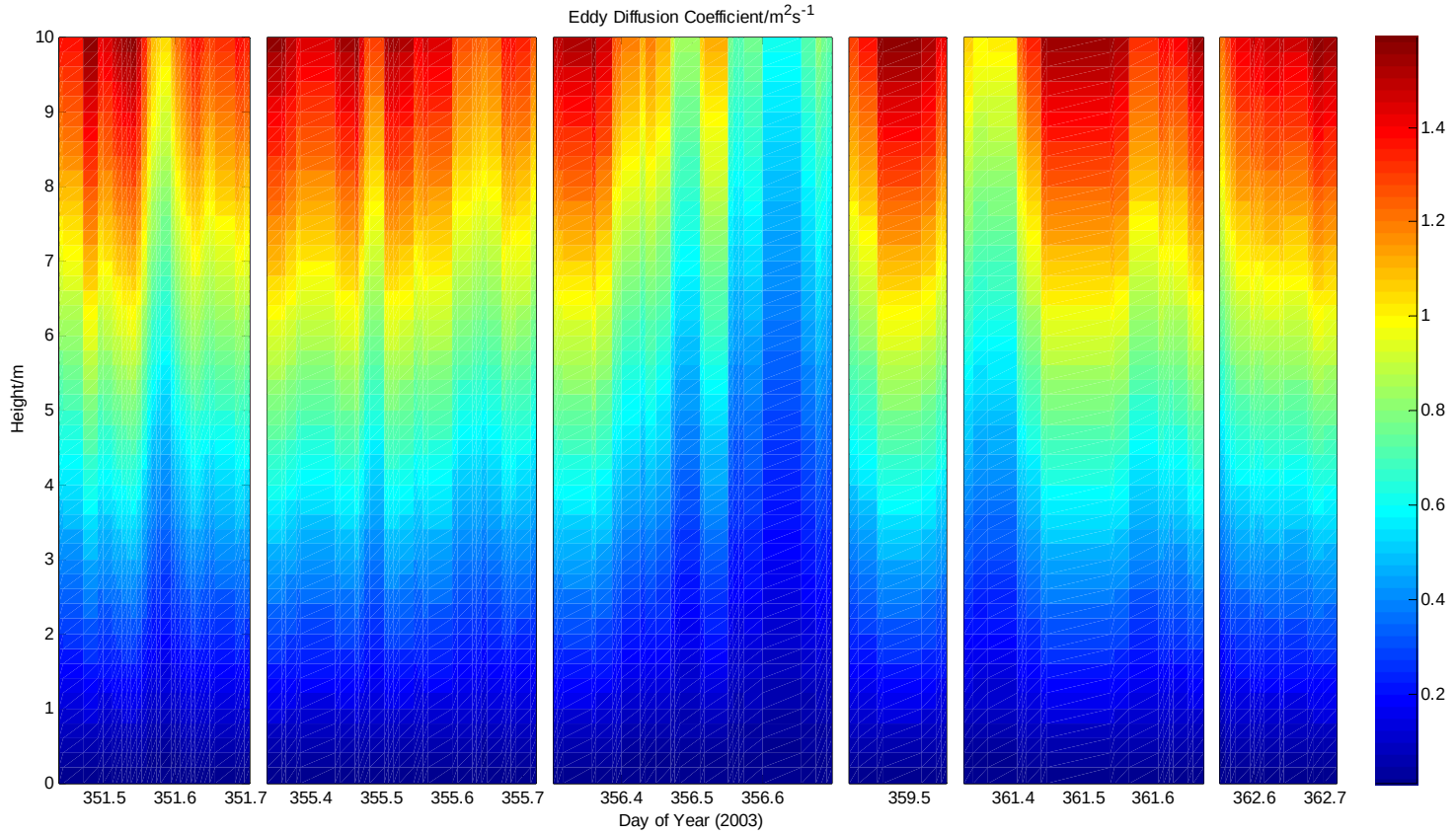

Figure 5.2.3-5. Simulation of eddy diffusion coefficient from 0 m to 10 m above snow on Dec 17th, 21st, 22nd, 25th, 27th and 28th.

Figure 5.2.3-4 shows the model results for the air above the snow surface. However, based on the large discrepancy between the modeled OH and measured OH, we can't apply current model for ATNCI 2003 measurement validation or future prediction unless we identify the unaccounted OH_x sink first. In addition, the temperature dependence on the QLL solute concentrations is not considered in current model, which will change the QLL ion concentration.

5.2.4 Air snowpack model sensitivity analysis

The HONO concentration deep in the snow is very sensitive to the pH, QLL to snow volume ratio and nitrite concentration (Table 5.2.4-1). From the table we can infer no nitrous acid emission on alkaline snow surfaces, which is consistent with the field measurements of Beine et al. (2005).

Table 5.2.4-1 Sensitivity analysis of HONO concentration deep below snow surface where the equilibrium between QLL HONO and interstitial air HONO is reached. The pH and $[NO_2^-]$ are measured melted snow minimum, median, and maximum concentrations from Dec 1st to 18th, 2003 (Jack Dibb, personal communication). The bold numbers are the parameters used in the model.

QLL to snow volume ratio= 2×10^{-3}				
HONO (pptv)		pH		
		5.3	**5**	4.5
$[NO_2^-]$ (10^{-9}M)	1	4	8	24
	20	84	**164**	470
	70	296	575	1646

QLL to snow volume ratio= 2×10^{-4}				
HONO (pptv)		pH		
		5.3	5	4.5
$[NO_2^-]$ (10^{-9}M)	1	42	82	235
	20	844	1644	4704
	70	2955	5753	16463

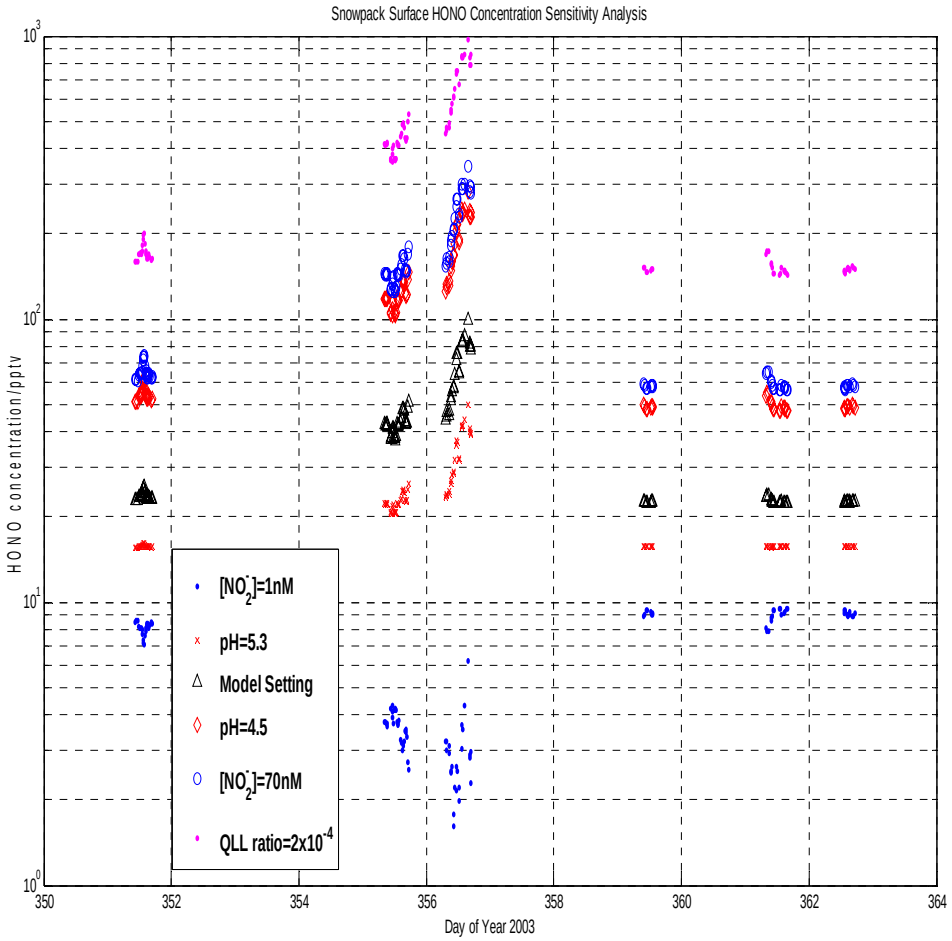

Figure 5.2.4-1. Sensitivity analysis of HONO concentration at the snow surface.

Figure 5.2.4-1 shows the snow surface HONO concentration is sensitive to the model parameters set up as well. The snowpack can be a HONO sink if there is not enough nitrite in the snowpack.

Another uncertainty is the QLL to snow volume ratio which is likely to be a function of temperature. However, if the ratio is very low, such as is shown on the right panel of table 5.2.4-1, we will need to revisit the relationship between QLL to snow volume ratio to QLL concentration. If the thickness of QLL is too thin, it is unlikely the

ions, like NO_3^-, will remain excluded from the snow to reach this super-saturated solution in the quasi-liquid layer. In that case, part of ions will be excluded as crystals and we need to estimate the saturation concentration for that temperature in the QLL.

Henry's Law refers to ideal solutions, which under the volume concentration effect of the QLL is not likely, but how to correct for nonideality in the QLL is still not clear. Other reactions that can happen, for example, NO_2^- and HONO can be oxidized by molecular oxygen to nitrate ions at a much faster rate (Takenaka et. al., 1992, 1996). Those areas remain unexplored.

Nitrous acid (HONO) and the nitrite ion represent a particularly important conjugate pair in the quasi liquid layer. In highly acidic media, HONO will form nitroacidium ion, H_2ONO^+.

$$H_2ONO_{(aq)}^{+} \xleftrightarrow{H^+} HONO_{(aq)} \xleftrightarrow{H^+} NO_2^{-}{}_{(aq)} \qquad (5.2.4\text{-}1)$$

pK_{a1}=1.7, pK_{a2}=2.8 (*Riordan, et al.*, 2005).

$$HONO_{(aq)} = N(III)\frac{pK_{a1}[H^+]}{[H^+]^2 + pK_{a1}[H^+] + pK_{a1}pK_{a2}} \qquad (5.2.4\text{-}2)$$

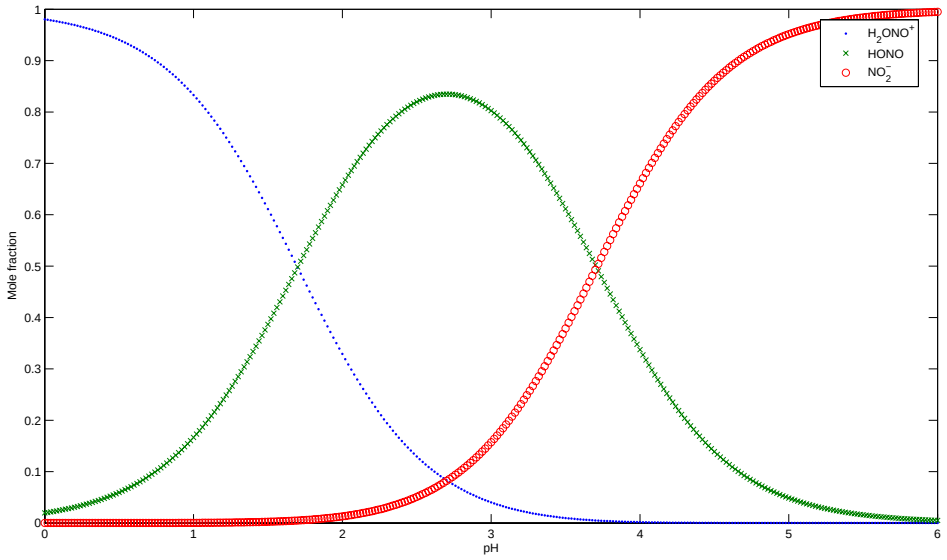

Figure 5.2.4-2. Model simulation of HONO speciation for the two-step equilibrium process.

Figure 5.2.4-2 shows that the aqueous phase HONO concentration in the snowpack is very sensitive to acidity of the QLL. It is assumed that ions are efficiently excluded on freezing, so the ratio of quasi-liquid layer ion concentration to melted snow ion concentration inversely tracks the QLL volume ratio. If we can apply the assumption to H^+, the pH of the QLL is likely to be significantly lower than that of the melted snow. In the other words, the QLL to snow grain volume ratio can influence the pH and further determine the ion distribution. However, we cannot apply the assumption to H^+ because of possible buffer species in the QLL. For example, the CO_2 concentration at the South Pole is about 374 ppmv (http://cdiac.ornl.gov/trends/co2/sio-spl.htm). The $[HCO_3^-]$ is inferred to be $3.6 \cdot 10^{-5}$ M in snow according to Henry's Law and the acid-base kinetics of carbonate ions. The melted snow H^+ concentration is $1.2 \cdot 10^{-5}$ M (Jack Dibb, personal communication). HCO_3^- together with other ions could buffer the change of H^+ (figure 5.2.4-3). In the current air snowpack model, it is supposed that the QLL pH stays

constant at 5 and the "extra" H^+ is bound by other weak-acid anions or stays in the ice matrix. In contrast, NO_2^- and NO_3^- stay within the QLL completely.

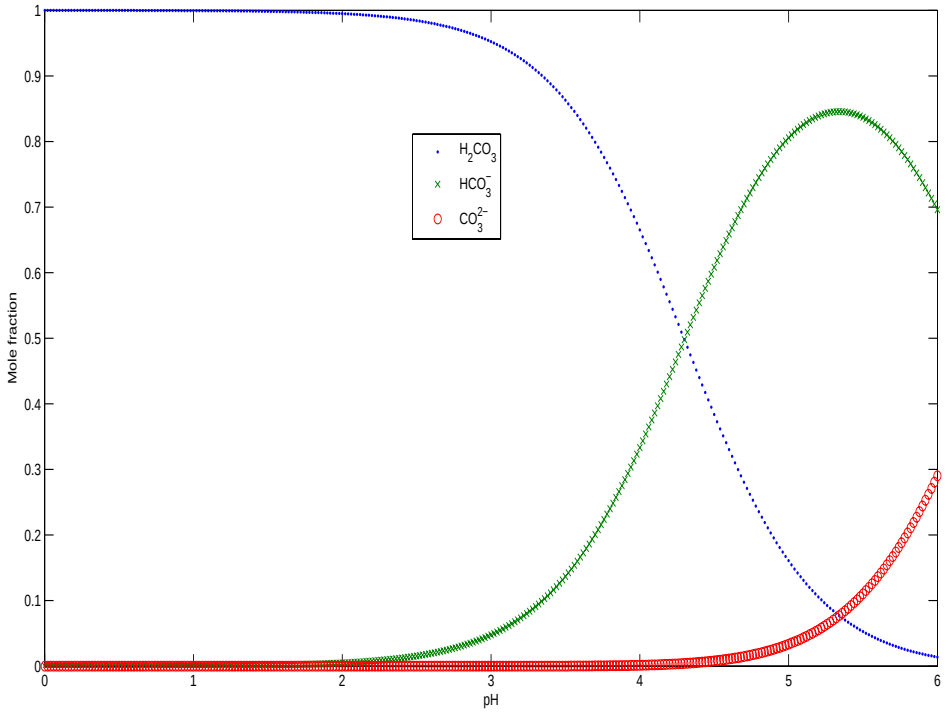

Figure 5.2.4-3. Model simulation of CO_2 speciation for the two-step equilibrium process.

5.3 Model discussions

It is widely accepted that the photolysis of nitrate is the main reason for the observed high HONO in Polar regions. Photolysis of nitrate can be a dominant HONO source inside the snowpack; however, the observed HONO emission from the snowpack was triggered mainly and directly by the equilibrium between quasi liquid layer nitrite and firn air HONO deep within the snow surface (i.e. 30 cm below snow surface). The high concentration HONO in the interstitial air is subsequently transported above snowpack by diffusion and windpumping. Since actinic flux decreases sharply in the vertical direction within snowpack, photolysis of nitrate is unlikely be a significant nitrite source 30 cm below the snow surface. Processes other than direct nitrate photolysis could be a source for nitrite, for an example, the hydrolysis of NO_2. So nitrate is important for HONO in the sense that photolysis of nitrate generates nitrite and NO_2 in the near surface areas, which could migrate down to vary the nitrite concentration at deeper level of snowpack. How nitrite vertically distributes is poorly characterized.

To have a better understanding of the snow chemistry, other gas species and detailed stoichiometry need to be included. In appendix A the framework of air-cloud multiphase chemistry (Ervens et al., 2003) is modified for the snowpack. There are numerous unknowns that must be tackled before we can routinely predict the rates of these reactions. Due to the lack of ANTCI 2003 field measurement and the uncertainty of chemistry inside the quasi-liquid layer, the comprehensive multiphase chemistry is not included in this thesis. However, even with future concurrent firn air measurements, measurements of concentrations in the snow are restricted to stable compounds in melted snow samples. There is no convincing evidence about whether different species attach to

surface hydrogen bonds, dissolve in the quasi-liquid layer or reside in the ice crystals. Species attached to the surface of snow crystals can be expected to have a reactivity similar to that in the aqueous phase. Species incorporated within the ice matrix are not in contact with the atmosphere. Their reactivity will be limited to the solid to quasi-liquid layer diffusion process which is extremely slow (Grannas et al., 2007). The partitioning of species leads to a guessing game for the chemical reactions. Our current understanding of the quasi-liquid layer is poorly characterized. It is assumed that QLL reaction rate will be similar to the liquid phase one and that the depth of the QLL is influenced by both the salt content of the snow and the ambient temperature. Treating the reactions in the QLL as aqueous means that we are assuming that we are dealing with concentrated true liquids, however, it is not clear whether such an assumption is warranted or not. There is experimental evidence that the thickness of the QLL increases with temperature (Girardet and Toubin, 2001), only limited species number of pollutants were discussed in the same study. However, in the very rich field of snow physicochemistry, the quantitative relationship between QLL depth and temperature as well as pollutant concentrations is not available.

Since the lifetime of OH is extremely short, the vertical scale of elevated OH concentrations depends on the lifetimes of the precursor compounds and the intensity of vertical mixing. However, due to the large discrepancy from the gas phase modeled OH and measured OH, the measured OH mixing ratio is assumed constant. This could lead to an underestimate of HONO in the gas phase. Levels of measured OH were also reported less than the modeled OH in the Summit, Greenland, which implied an unidentified HO_x sink (Yang et al., 2002).

5.4 Future research

The purpose of this part is pointing out further investigations needed to develop the coupled air-snow chemical models.

First we need a better description of physical constants of the top 30cm of surface snow layers. For an example, the vertically resolved density, temperature gradient, permeability of the snowpack, and dimension of sastrugi. These factors are important for calculating the wind pumping processes. In areas with less permeable snow, the residence time may be sufficiently large to allow those gases to react with other reactants contained in snow, resulting in less observed emissions. Air flow in this thesis is mainly caused by wind-driven variations in surface pressure over a rough snow surface.

Secondly, there are two important physical processes for the transmission of light inside snowpack: scattering and absorption. Thus the snow surface areas, albedo of snow, impurity (especially soot) concentration and grain shape are important physical constants. Vertically resolved measurements of irradiance are applied to constrain radiation transfer models and used to invert the measurements to actinic fluxes.

Thirdly, temperature, pH and ionic content of natural snow are determining factors for modeling HONO. Temperature determines the chemical reaction constant and the depth of the quasi-liquid layer. Most importantly, we need to have more evidence to apply the melted snow measurement to the actual number and reaction rate in the quasi liquid layer. Measurements of trace gas fluxes at different snowpack depth are very helpful to parameterize the numerical model calculation.

Fourthly, boundary layer dynamics (advection and turbulent mixing near snow surface) assists the interpretation and predictive power of air chemistry. Snow

microphysics of QLL and reaction kinetics in this layer needs further investigation. To have a better understanding of the snow chemistry, other gas species and detailed stoichiometry need to be included.

CHAPTER SIX

CONCLUSIONS

Atmospheric nitrous acid (HONO) is an important source of OH in urban areas. It is a significant and sometimes dominant OH source in polar regions. In the polar atmosphere, measurements of HONO are an important part of understanding the dynamics of snow-air chemistry and atmospheric photochemistry. The low levels of HONO present in such regions necessitate the development of instrumentation with low detection limits. An improved method of detecting HONO is developed using photo-fragmentation and laser-induced fluorescence. HONO is photo-fragmented into OH and NO at 355 nm and the generated OH (v′′=0 state) is probed at 282 nm to the v′=1 excited state; the excited state OH fluorescence at 309 nm is detected by a photomultiplier tube. The instrument is calibrated using standard HONO produced from the reaction of sulfuric acid and sodium nitrite. The detection limit of this method is 2-3 pptv for ten-minute integration time with 35% uncertainty.

The ANTCI 2003 measurements confirm the high N oxides observed previously in ISCAT 1998 and 2000. The median LIF observed mixing ratio of HONO 10m above the snow was 5.8 pptv (mean value 6.3 pptv) with a maximum of 18.2pptv on Nov 30th, Dec 1st, 3rd, 15th, 17th, 21st, 22nd, 25th, 27th and 28th. The LIF HONO observations are compared to concurrent HONO observations performed by mist chamber/ion chromatography (MC/IC). Both the LIF and MC/IC techniques observed enhanced HONO; however, the MC/IC observations were higher than the LIF observations by a factor of 7.2±2.3 in the median and the data are not correlated. It is possible that the MC/IC technique might suffer from interference from HNO_4. A comparison between the

soluble nitrite measurement by MC/IC and the pernitric measurement may help to resolve measurement issues. HONO as measured by both techniques roughly follow NO levels and scale inversely with boundary layer height. As in ISCAT 2000, the abundance of both HONO measurements exceeds the pure gas phase model predictions, with LIF higher than the pure gas phase model by a factor of 1.92±0.67, which implies snow emission of HONO must be occurring. The LIF observed HONO are not high enough to significantly influence the NO_x budget during ANTCI 2003, but will increase the model HO_x over-prediction by 28%±15% and lead to a dramatic over-prediction of measured OH by 157%±35%. Given the short lifetime of HONO, these differences are hard to reconcile with observed low OH levels unless there is a missing HO_x sink. It appears, however, that HONO competes with O_3 and HCHO as the dominant source of OH at South Pole during ANTCI 2003.

Since pure gas phase chemistry cannot resolve the measured high concentration of HONO, a 1D air-snowpack model of HONO was developed and constrained by observed chemistry and meteorology data. The 1D model includes pure gas phase chemical mechanisms, molecular diffusion and mechanical dispersion, windpumping in snow, gas phase to quasi-liquid layer phase HONO transfer and quasi-liquid layer nitrate photolysis. Photolysis of nitrate is important as a dominant HONO source inside the snowpack, however, the observed HONO emission from the snowpack was triggered mainly by the equilibrium between quasi liquid layer nitrite and firn air HONO deep down the snow surface (i.e. 30 cm below snow surface). The high concentration of HONO in the firn air is subsequently transported above snowpack by diffusion and windpumping. In order to predict the vertical profile of HONO concentration inside the snowpack, the following

information is needed: the changes of surface pressure, winds above the snow surface, temperature, snow density, snowpack permeability, dimension of sastrugi, albedo of snow, soot concentration of snow, snow grain shape, concentration of nitrate and nitrite, pH of snow, mass accommodation of HONO to quasi liquid layer of snow and reversible dissolution (according to the Henry's Law), etc. Given the limited ANTCI 2003 field measurements of pH and nitrite snowpack concentrations, snow emission of HONO is highly likely and will be transported to 10 meters above the snow, where GT LIF measured high HONO concentration. The pH and thickness of quasi liquid layer along with continuous nitrite measurement are key factors to calibrate and validate the air snowpack model.

APPENDIX A
FUTURE DEVELOPMENT OF THE AIR SNOW

MULTIPHASE MODELING

Reactions in the quasi-liquid layer are potentially important in the generation or transformation of interstitial air pollutants. The processes consist of the following sequence of steps: Mass-transport of the precursor species to the air-QLL interface; transfer across the interface and establishment of solubility equilibrium locally at the interface; mass-transport of the dissolved gas or ions in the aqueous phase; aqueous phase chemical reactions; mass-transport of reaction products and subsequent evolution into the gas-phase. Defining and comparing the characteristic times of these processes is important to find the rate-controlling processes. If any process is rapid compared to other processes, then this process is negligible which leads to substantial simplification of the description. After finding the rate limiting step, at times long compared to the characteristic time for this process, the system reaches a "steady state" in which species concentrations, fluxes, reaction rates, etc., no longer vary as a function of time. The description of the space and time dependence of species concentrations in terms of partial differential equations can be simplified to space dependence of species concentration represented by an ordinary differential equation. Coupling is made through boundary conditions at the interstitial air/quasi liquid layer interface by assuming equilibrium as described by Henry's law. This treatment not only simplified the system but also provides more insight.

The transfer of molecules from the interstitial air phase to the QLL aqueous phase and vice versa is treated by the resistance model of Schwartz [1986]. In this model gas

phase diffusion, mass accommodation and the Henry's Law constants are considered. The following parameters are taken from Herrmann et al (2000). The mass transport from the gas phase is described as a first order loss rate constant:

$$k_t = \left(\frac{r^2}{3D_g} + \frac{4r}{3 \cdot \bar{c} \cdot \alpha} \right)^{-1} \quad \text{(A-1)}$$

D_g = gas phase diffusion coefficient [$m^2\ s^{-1}$]

α = mass accommodation coefficient

r = snow crystal radius (10 μm)

$\bar{c}$ = molecular speed = $\left(\frac{8RT}{\pi M} \right)^{1/2}$ [$m\ s^{-1}$]

M = molecular mass [$kg\ mol^{-1}$]

R = gas constant [$J\ mol^{-1}\ K^{-1}$]

In total, the phase transfer is described by the following equations [Schwartz, 1986]:

$$\frac{d[X]_{aq}}{dt} = Q_{aq} - S_{aq} + \left(C_g k_t - \frac{[X]_{aq} \cdot k_t}{K_H} \right) \frac{1000}{RT} \quad \text{(A-2)}$$

$$\frac{dC_g}{dt} = D \frac{\partial^2 C_g}{\partial z^2} - U \frac{\partial C_g}{\partial z} + Q_g - S_g - \left(C_g \cdot k_t - \frac{[X]_{aq} \cdot k_t}{K_H} \right) \frac{1000}{RT} \quad \text{(A - 3)}$$

$[X]_{aq}$ = QLL phase concentration [$mol\ L^{-1}$],

Q_g = gas phase source rate [$cm^{-3}\ s^{-1}$],

C_g = gas phase particle density [cm^{-3}],

S_g = gas phase sink rate [$cm^{-3}\ s^{-1}$],

T = temperature [K],

LWC = liquid water content [–],

(fixed to $6 \cdot 10^{-4}$ vol/vol),

Q_{aq} = QLL phase source reaction rate [mol L^{-1} s^{-1}],

S_{aq} = QLL phase sink reaction rate [mol L^{-1} s^{-1}],

K_H = Henry's Law constant [mol L^{-1} atm^{-1}],

k_t = gas phase transfer coefficient [s^{-1}],

R = gas constant.

A significant area of uncertainty relates to the assumed aqueous-like surface layer on the snow grains. As all ions are assumed to be present in this layer, the concentrations will depend on the QLL to snow grains volume ratio. Here I test the sensitivity of this ratio with respect to the species fraction according to the Henry's Law.

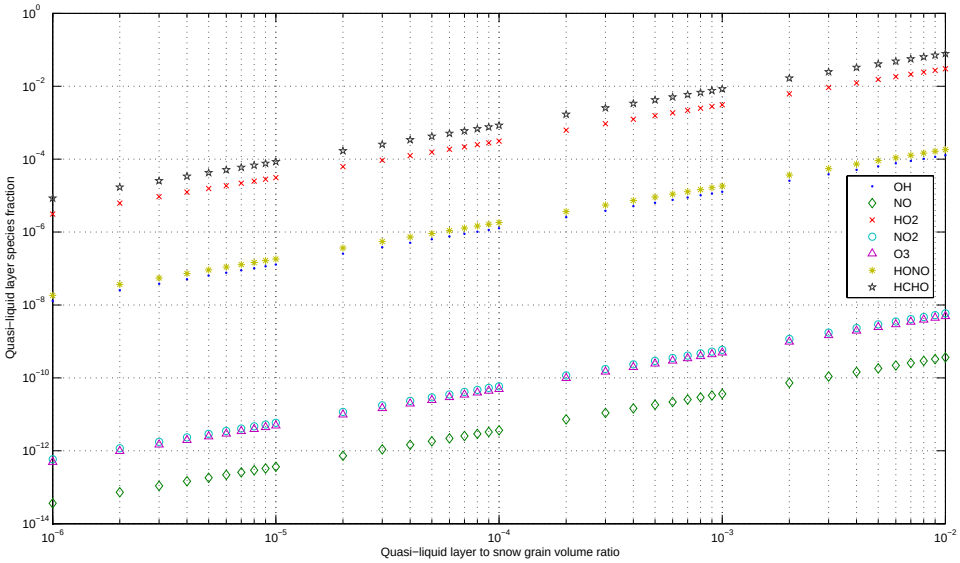

Figure A-1 Various species QLL aqueous fraction versus QLL to snow grain volume ratio at 238K

Table A-1 Henry's Law constants (K_H), mass accommodation coefficients (α) and gas phase diffusion coefficients (D_g).

Species	K_{H298}, M atm^{-1}	ΔH/R, K	α	D_g, [10^{-5} m^2 s^{-1}]
O_3	$1.14 \cdot 10^{-2}$	-2300	0.05	1.48
HO_2	$9 \cdot 10^3$		0.01	1.04
OH	25	-5280	0.05	1.53
H_2O_2	$1.02 \cdot 10^5$	-6340	0.11	1.46
HNO_3	$2.1 \cdot 10^5$	-8700	0.054	1.32
NO_2	$1.2 \cdot 10^{-2}$	-1263	0.0015	1.92
HNO_2	49	-4880	0.5	1.30
HCHO	$3 \cdot 10^3$	-7216	0.2	1.64
NO	$1.2 \cdot 10^{-2}$	-1263	0.001	2.24

Constants taken from Ervens et al., 2003.

Table A-2 HO_x chemistry

Reaction	k_{298}, M^{-n} s^{-1}	E_a/R, K	Reference
(1) $O_3 + O_2^- \xrightarrow{H^+} 2O_2 + OH$	$1.5 \cdot 10^9$	2200	Sehested et al.,1983
(2) $HO_2 + HO_2 \longrightarrow O_2 + H_2O_2$	$8.3 \cdot 10^5$	2720	Bielski et al., 1985
(3) $HO_2 + O_2^- \xrightarrow{H^+} O_2 + H_2O_2$	$9.7 \cdot 10^7$	1060	Bielski et al., 1985
(4) $HO_2 + OH \longrightarrow O_2 + H_2O$	$1.0 \cdot 10^{10}$		Elliot and Buxton, 1992
(5) $OH + O_2^- \longrightarrow O_2 + OH^-$	$1.1 \cdot 10^{10}$	2120	Christensen et al., 1989
(6) $H_2O_2 + OH \longrightarrow HO_2 + H_2O$	$3.0 \cdot 10^7$	1680	Christensen et al., 1982
(7) $OH + O_3 \longrightarrow O_2 + HO_2$	$1 \cdot 10^8$		Sehested et al., 1984
(8) $O^3P + O_2 \longrightarrow O_3$	$4 \cdot 10^9$		Klaning et al.,1984

Table A-3 Nitrogen chemistry

Reaction	k_{298}, M^{-n} s^{-1}	E_a/R, K	Reference
(9) $OH + NO_2 \xrightarrow{H^+} NO_3^- + H^+$	$1.2 \cdot 10^{10}$		Wagner et al., 1980
(10) $NO_2 + O_2^- \longrightarrow NO_2^- + O_2$	$1 \cdot 10^8$		Warneck and Wurzinger, 1988
(11) $NO_2 + NO_2 \xrightarrow{H_2} HNO_2 + NO_3^- + H^+$	$8.4 \cdot 10^7$	-2900	Park and Lee, 1988
(12) $NO_2^- + OH \longrightarrow NO_2 + OH^-$	$1.1 \cdot 10^{10}$		Barker et al., 1970
(13) $NO_2^- + O_3 \longrightarrow NO_3^- + O_2$	$5 \cdot 10^5$	7000	Damschen and Martin,

			1983
(14) $HNO_2 + OH \longrightarrow NO_2 + H_2O$	$1 \cdot 10^9$	1500	Rettich, 1978
(15) $NO_3^- + O^3P \longrightarrow NO_2^- + O_2$	$2 \cdot 10^8$	1500	Mack and Bolton, 1999
(16) $OH + NO \longrightarrow NO_2^- + H^+$	$2 \cdot 10^{10}$	1500	Strehlow and Wagner,1982

Table A-4 Aqueous phase photochemistry

Reaction number	Reaction
J_1	$NO_3^- + hv \xrightarrow{H^+} NO_2 + OH$
J_2	$NO_3^- + hv \longrightarrow NO_2^- + O^3P$
J_3	$NO_2^- + hv \xrightarrow{H^+} NO + OH$
J_4	$HONO + hv \longrightarrow NO + OH$
J_5	$H_2O_2 + hv \longrightarrow 2OH$
J_6	$NO_2 + hv \longrightarrow NO + O$
J_7	$O_3 + hv \xrightarrow{H_2O} H_2O_2 + O_2$

See actinic flux part for reference

Table A-5 Dissociation equilibrium

Reaction number	Reaction	K_{eq} M	Reference
Ek1	$HO_2 \leftrightarrow H^+ + O_2^-$	$3.5 \cdot 10^{-5}$	Perrin,1982
Ek2	$HONO \leftrightarrow H^+ + NO_2^-$	$1.96 \cdot 10^{-4}$	Schwartz and White,1981

Table A-6 Steady state species

Phase	Species
Aqueous	NO_2^-, NO_3^-, OH, NO, HO_2, H_2O_2, NO_2, O_3,HONO, O^3P

$$\frac{d[NO_2^-]}{dt} = (AJ2 + Ak15 \cdot [O^3P]) \cdot [NO_3^-] + Ak10 \cdot [O_2^-] \cdot [NO_2] - (AJ3 + Ak12 \cdot [OH] + Ak13 \cdot [O_3]) \cdot [NO_2^-] = 0 \quad \text{(A-4)}$$

$$\frac{d[NO_3^-]}{dt} = Ak9 \cdot [NO_2] \cdot [OH] + Ak13 \cdot [NO_2^-] \cdot [O_3] + Ak11 \cdot [NO_2]^2 - (AJ1 + AJ2 + Ak15 \cdot [O^3P]) \cdot [NO_3^-] = 0 \quad \text{(A-5)}$$

$$\frac{d[OH]}{dt} = AJ1\cdot[NO_3^-] + AJ3\cdot[NO_2^-] + AJ4\cdot[HONO] + Ak1\cdot[O_3]\cdot[O_2^-] + 2\cdot AJ5\cdot[H_2O_2]$$
$$-\{Ak12\cdot[NO_2^-] + Ak16\cdot[NO] + Ak9\cdot[NO_2] + Ak14\cdot[HONO] + Ak5\cdot[O_2^-] + Ak4\cdot[HO_2] \quad \text{(A-6)}$$
$$+ Ak6\cdot[H_2O_2] + Ak7\cdot[O_3]\}\cdot[OH] = 0$$

$$\frac{d[NO]}{dt} = AJ3\cdot[NO_2^-] + AJ4\cdot[HONO] - Ak16\cdot[OH]\cdot[NO] = 0 \quad \text{(A-7)}$$

$$\frac{d[HO_2]}{dt} = Ak6\cdot[H_2O_2]\cdot[OH] - (Ak2\cdot[HO_2] + Ak3\cdot[O_2^-] + 2\cdot Ak4\cdot[OH])\cdot[HO_2] = 0 \quad \text{(A-8)}$$

$$\frac{d[H_2O_2]}{dt} = Ak2\cdot[HO_2]^2 + Ak3\cdot[HO_2]\cdot[O_2^-] + Ak7\cdot[OH]\cdot[O_3] - (AJ5 + Ak6\cdot[OH])\cdot[H_2O_2] = 0 \quad \text{(A-9)}$$

$$\frac{d[NO_2]}{dt} = AJ1\cdot[NO_3^-] + Ak12\cdot[NO_2^-]\cdot[OH] + Ak14\cdot[HONO]\cdot[OH] \quad \text{(A-10)}$$
$$-(Ak10\cdot[O_2^-] + Ak9\cdot[OH] + Ak11\cdot[NO_2] + AJ6)\cdot[NO_2] = 0$$

$$\frac{d[O_3]}{dt} = Ak8\cdot[O^3P]\cdot[O_2] - (Ak1\cdot[O_2^-] + AJ7 + Ak7\cdot[OH])\cdot[O_3] = 0 \quad \text{(A-11)}$$

$$\frac{d[HONO]}{dt} = Ak11\cdot[NO_2]^2 + Ak16\cdot[NO]\cdot[OH] - (AJ4 + Ak14\cdot[OH])\cdot[HONO] = 0 \quad \text{(A-12)}$$

$$\frac{d[O^3P]}{dt} = AJ2\cdot[NO_3^-] - (Ak15\cdot[NO_3^-] + Ak8\cdot[O_2])\cdot[O^3P] = 0 \quad \text{(A-13)}$$

$$[H^+]\cdot[O_2^-] - Ek1\cdot[HO_2] = 0 \quad \text{(A-14)}$$

$$[H^+]\cdot[NO_2^-] - Ek2\cdot[HONO] = 0 \quad \text{(A-15)}$$

There are numerous unknowns that must be tackled before we can routinely predict the steady state concentration and rates of these reactions. Due to the lack of ANTCI 2003 field measurement and the uncertainty of chemistry inside the quasi-liquid layer, the comprehensive multiphase chemistry is not included in this thesis.

REFERENCES

Acker., K., Mfller, D., Auel, R., Wieprecht, W., Kalag, D., 2005. Concentrations of nitrous acid, nitric acid, nitrite and nitrate in the gas and aerosol phase at a site in the emission zone during ESCOMPTE 2001 experiment. Atmospheric Research 74, 507-524.

Acker, K., Moller, D., Wieprecht, W., Meixner, F.X., Bohn, B., Gilge, S., Plass-Dulmer, C., Berresheim, H., 2006. Strong daytime production of OH from HNO_2 at a rural mountain site. Geophysical Research Letters, 33, L02809 (doi:10.1029/2005GL024643).

Alicke B., Geyer, A., Hofzumahaus, A., Holland, F., Konrad, S., Pätz, H. W., Schäfer, J., Stutz, J., Volz-Thomas, A., Platt, U., 2003. OH formation by HONO photolysis during the BERLIOZ experiment. Journal of Geophysical Research 108 (D4), 8247- 8249.

Allegrini, I., De Santis, F., Di Palo, V., Febo, A., Perrino, C., Possanzini, M., Liberti, A., 1987. Annular denuder method for sampling reactive gases and aerosols in the atmosphere. Science of the Total Environment 67, 1–16.

Anastasio, C., Galbavy, E. S., Hutterli, M. A., Burkhart, J. F., Friel, D. K., 2007. Photoformation of hydroxyl radical on snow grains at Summit, Greenland, in press, doi:10.1016/j.atmosenv.2006.12.011, Atmospheric Environment.

Anderson, P.S., Neff, W.D., 2007. Boundary layer physics over snow and ice. Atmospheric Chemistry and Physics Discussions 7, 7625-7677.

Andres-Hernandez, M.D., Notholt, J., Hjorth, J., Schrems, O., 1996. A DOAS study on the origin of nitrous acid at urban and non-urban sites. Atmospheric Environment 30, 175-180.

Appel, B.R., Winer, A.M., Tokiwa, Y., Biermann, H.W., 1990. Comparison of atmospheric nitrous acid measurements by annular denuder and optical absorption systems. Atmospheric Environment 24 (A), 611–616.

Bailey, A.E., Heard, D.E., Paul, P.H., Pilling, M.J., 1997. Collisional quenching of OH ($A\ ^2\Sigma^+$, v'=0) by N_2, O_2 and CO_2 between 204 and 294K. Implications for atmospheric measurements of OH by laser-induced fluorescence. Journal of the Chemical Society, Faraday Transactions 93(16), 2915-2920.

Bailey, A.E., Heard, D.E., Henderson., D.A., Paul, P.H., 1999. Collisional quenching of OH (A $^2\Sigma^+$, v'=0) by H_2O between 211 and 294K and the development of a unified model for quenching. Chemical Physics Letters 302, 132-138.

Barker, G.C., Fowles, P., Stringer, B., 1970. Pulse radiolytic induced transient electrical conductance in liquid solutions of NO_3^-, NO_2^- and $Fe(CN)_6^{3-}$. Transactions of the Faraday Society 66, 1509-1519.

Barney, W.S., Wingen, L.M., Lakin, M.J., Brauers, T., Stutz, J., Finlayson-Pitts, B. J., 2000. Infrared absorption cross-section measurements for nitrous acid (HONO) at room temperature. The Journal of Physical Chemistry A 104(8), 1692-1699.

Bartels-Rausch, T., Eichler, B., Zimmermann, P., Gaggeler, H.W., Ammann, M., 2002. The adsorption enthalpy of nitrogen oxides on crystalline ice. Atmospheric Chemistry & Physics*, 2*, 235-247.

Bartels-Rausch, T., Donaldson, D.J., 2006. HONO and NO_2 evolution from irradiated nitrate-doped ice and frozen nitrate solutions. Atmospheric Chemistry & Physics Discussions*,* 6, 10713-10731.

Becker, K.H., Kleffmann, J., Kurtenbach, R., Wiesen, P, 1996. Solubility of nitrous acid (HONO) in sulfuric acid solutions. The Journal of Physical Chemistry 100, 14984-14990.

Beine, H. J., Domine, F., Simpson, W., Honrath, R.E., Sparapani, R., Zhou., X. L., King, M., 2002. Snow-pile and chamber experiments during the Polar Sunrise Experiment 'Alert 2000': exploration of nitrogen chemistry. Atmospheric Environment, 36, 2707-2719.

Beine, H. J., Amoroso, A., Esposito, G., Sparapani, R., Ianniello, A., Georgiadis, T., Nardino, M., Bonasoni, P., Cristofanelli, P., Domine, F., 2005. Deposition of atmospheric nitrous acid on alkaline snow surfaces. Geophysical Research Letters 32, L10808, (doi:10.1029/2005GL022589).

Bielski, B.H. J., Cabelli, D.E., Arudi, R.L., Ross, A.B., 1985. Reactivity of HO_2/O_2^- radicals in aqueous solution. Journal of Physical and Chemical Reference Data 14, 1041-1100.

Bottenheim, J.W., Shepson, P.B., Sturges, B., 2002. Special Issue on Air/Snow/Ice Interactions in the Arctic: Results from ALERT 2000 and SUMMIT 2000. Atmospheric Environment 36 (15-16), 2467-2469.

Boxe, C.S., 2005. Nitrate photochemistry and interrelated chemical phenomena in ice: influence of the quasi-liquid layer (QLL). Doctorate dissertation, California Institute of Technology.

Bradshaw, J.D., Rodgers, M.O., Davis, D.D., 1984. Sequential two-photon laser-induced fluorescence: A new technique for detecting hydroxyl radicals. Applied Optics 23, 2134-2145.

Briegleb, B. P., Light, B., 2007. A Delta-Eddington multiple scattering parameterization for solar radiation in the sea ice component of the community climate system model. NCAR technical note.

Burley, J. D., Johnston, H. S., 1992. Ionic mechanisms for heterogeneous stratospheric reactions and ultraviolet photo absorption cross-sections for NO_2^+, HNO_3, and NO_3^- in sulfuric-acid. Geophysical Research Letters 19, (13), 1359-1362.

Butkovskaya, N., Kukui, A., Le Bras, G., 2007. HNO_3 forming channel of the HO_2 + NO reaction as a function of pressure and temperature in the ranges 72-600 Torr and 223-323 K. Journal of Physical Chemistry A, 111, 9047-9053.

Calvert, J.G., Yarwood, G., Dunker A.M., 1991. The evaluation of the mechanism of nitrous acid formation in the urban atmosphere. Research on Chemical Intermediates 20, 463-480.

Chan, W.H., Nordstrom, R.J., Galvert, J.G., Shaw, J.H., 1976. An IRFTS spectroscopic study of the kinetics and the mechanism of the reactions in the gaseous system, HONO, NO, NO_2, H_2O. Chemical Physics Letters 37, 441-446.

Christensen, H., Sehested, K., Bjergbakke, E., 1989. Radiolysis of reactor water: Reaction of hydroxyl radicals with superoxide (O_2^-). Water Chemistry Nuclear Reaction System 5, 141-144.

Christensen, H., Sehested, K., Corfitzen, H., 1982. Reactions of hydroxyl radicals with hydrogen peroxide at ambient and elevated temperatures. Journal of Physical Chemistry 86, 1588-1590.

Chu, L.; Anastasio, C., 2003. Quantum yields of hydroxyl radical and nitrogen dioxide from the photolysis of nitrate on ice. Journal of Physical Chemistry A 107, (45), 9594-9602.

Cleveland, C.B., Wiesenfeld, J.R., 1988. Electronic quenching of highly rotationally excited OH ($A^2\sum$, v'=0, 1) by H_2O. Chemical Physics Letters 144, 479-485.

Coe, H., Jones, R.L., Colin, R., Carleer, M., Harrison, R.M., Peak, J., Plane, J.M.C., Smith, N., Allan, B., Clemitshaw, K.C., Burgess, R.A., Platt, U., Etzkorn, T., Stutz, J., Pommereau, J.-P., Goutail, F., Nunes-Pinharanda, M., Simon, P., Hermans, C., Vandaele, A.-C., 1997. A comparison of differential optical absorption spectrometers for measurement of NO_2, O_3, SO_2 and HONO. In: Borrell, P.M., Borrell, P., Cvitaš , T., Kelly, K., Seiler, W. (Eds.). Proceedings of EUROTRAC Symposium'96: Transport and Transformation of Pollutants. Computational Mechanics Publications, Southampton, pp. 757–762.

Colbeck, S.C., 1989. Air movement in snow due to windpumping. Journal of Glaciology, 35 (120), 209-213.

Cox, R.A., Derwent, R. G., 1976. The ultra-violet absorption spectrum of gaseous nitrous acid. Journal of Photochemistry 6, 23-34.

Cox, R.A., 1974. The photolysis of gaseous nitrous acid. Journal of Photochemistry 3, 175-178.

Crutzen, P.J., 1970. The influence of nitrogen oxides on the atmospheric ozone content. Quarterly Journal of the Royal Meteorological Society 96, 320-325.

Cunningham, J., Waddington, E.D., 1993. Air flow and dry deposition of non-sea salt sulfate in polar firn: paleoclimatic implications. Atmospheric Environment 27A (17/18), 2943-2956.

Damschen, D.E., Martin, L.R., 1983. Aqueous aerosol oxidation of nitrous acid by O_2, O_3 and H_2O_2. Atmospheric Environment 17, 2005-2011.

Davis, D.D., Rodgers, M.O., Fischer, S.D., 1981. A Theoretical assessment of the O_3/H_2O interference problem in the detection of natural levels of OH via laser induced fluorescence. Geophysical Research Letters 8 (1), 73-76.

Davis, D.D., Eisele, F., Chen, G., Crawford, J., Huey, G., Tanner, D., Slusher, D., Mauldin, L., Oncley, S., Lenschow, D., Semmer, S., Shetter, R., Lefer, B., Arimoto, R., Hogan, A., Grube, P., Lazzara, M., Bandy, A., Thornton, D., Berresheim, H., Bingemer, H., Hutterli, M., McConnell, J., Bales, R., Dibb, J., Buhr, M., Park, J., McMurry, P., Swanson, A., Meinardi, S., and Blake, D., 2004. An overview of ISCAT 2000. Atmospheric Environment, *38* (32), 5363-5373.

Dibb, J.E., Talbot, R.W., Bergin, M.H., 1994. Soluble acidic species in air and snow at Summit, Greenland. Geophysical Research Letters 21(15), 1627-1630.

Dibb, J.E., Talbot, R.W., Munger, J.W., Jacob, D.J., Fan, S.M.,1998. Air–snow exchange of HNO_3 and NO_y at Summit, Greenland. Journal of Geophysical Research 103, 3475-3486.

Dibb, J.E., Arsenault, M., Peterson, M.C., Honrath, R.E., 2002. Fast nitrogen oxide photochemistry in Summit, Greenland snow. Atmospheric Environment 36, 2501-2511.

Dibb, J.E., Huey, L.G., Slusher, D.L., Tanner, D.J., 2004. Soluble reactive nitrogen oxides at South Pole during ISCAT 2000. Atmospheric Environment 38, 5399-5409.

Domine, F., Shepson, P.B., 2002. Air-snow interactions and atmospheric chemistry. Science 297, 1506-1510.

Domine, F., Albert, M., Huthwelker, T., Jacobi, H. W., Kokhanovsky, A. A., Lehning, M., Picard, G., Simpson, W. R., 2007. Snow physics as relevant to snow photochemistry. Atmospheric Chemistry and Physics Discussions 7, 5941-6036.

Dubowski, Y., Colussi, A.J., Hoffmann, M.R., 2001. Nitrogen dioxide release in the 302 nm band photolysis of spray-frozen aqueous nitrate solutions. Atmospheric implications. Journal of Physical Chemistry A, 105, 4928-4932.

Elliot, A. J., Buxton, G. V., 1992. Temperature dependence of the reactions $OH+O_2^-$ and $OH + HO_2$ in water up to 200°C. Journal of the Chemical Society Faraday Transactions 88, 2465-2470.

Ervens, B., George, C., Williams, J. E., Buxton, G.V., Salmon, G.A., Bydder, M., Wilkinson, F., Denener, F., Mirabel, P., and Herrmann, H., 2003. CAPRAM 2.4 (MODAC mechanism): An extended and condensed tropospheric aqueous phase

mechanism and its application. Journal of Geophysical Research, 108 (D14), 4426, (doi:10.1029/2002JD002202).

Febo, A., Perrino, C., Cortiello, M., 1993. A denuder technique for the measurement of nitrous acid in urban atmospheres. Atmospheric Environment 27, 1721-1728.

Febo, A., Perrino, C., Allegrini, I., 1996. Measurement of nitrous acid in Milan, Italy, by DOAS and diffusion denuders. Atmospheric Environment 30, 3599–3609.

Ferm, M., Sjodin, A., 1985. A sodium carbonate coated denuder for determination of nitrous acid in the atmosphere. Atmospheric Environment 19, 979–983.

Finlayson-Pitts, B.J., Pitts Jr., J.N., 1986. Atmospheric chemistry: Fundamentals and Experimental Techniques. Wiley-Interscience, New York.

Finlayson-Pitts, B.J., Pitts Jr., J.N., 2000. Chemistry of the upper and lower atmosphere-theory, experiment, and applications, pp. 273-276. Wiley, New York.

Finlayson-Pitts, B.J., Wingen, L.M., Sumner, A.L., Syomin, D., Ramazan, K.A., 2003. The heterogeneous hydrolysis of NO_2 in laboratory systems and in outdoor and indoor atmospheres: An integrated mechanism. Physical Chemistry Chemical Physics, 5 (2), 223-242.

Fischer, M.; Warneck, P., 1996. Photodecomposition of nitrite and undissociated nitrous acid in aqueous solution. Journal of Physical Chemistry 100, (48), 18749-18756.

Girardet, C., Toubin, C., 2001. Molecular atmospheric pollutant adsorption on ice: a theoretical survey. Surface Science Reports 44, 159-238.

Graedel, T. E.; Weschler, C. J., 1981. Chemistry within aqueous atmospheric aerosols and raindrops. Reviews of Geophysics**,** 19, (4), 505-539.

Grannas, A. M., Jones, A. E., Dibb, J., Ammann, M., Anastasio, C., Beine, H., Bergin, M., Bottenheim, J., Boxe, C.S., Carver, G., Crawford, J. H., Domine., F, Frey, M. M., Guzman, M.I., Heard, D., Helmig, D., Hoffmann, M. R., Honrath, R. E., Huey, L. G., Jacobi, H.-W., Klan, 30 P., McConnell, J., Sander, R., Savarino, J., Shepson, P. B., Simpson, W. R., Sodeau, J., von Glasgow, R., Weller, R., Wolff, E., and Zhu, T., 2007. An overview of snow photochemistry: evidence,

mechanisms and impacts. Atmospheric Chemistry and Physics Discussions, 7, 4165–4283.

Grenfell, T.C., Perovich, D.K., 1981. Radiation absorption coefficients of polycrystalline ice from 400 to 1400 nm. Journal of Geophysical Research 86, 7447-7450.

Hard, T.M., O'Brien, R.J., Chan, C.Y., Mehrabzadeh., A.A., 1984. Tropospheric free radical determination by FAGE. Environmental Science and Technology 18 (10), 768-777.

Hard, T.M., O'Brien, R.J., Cook, T.B., 1980. Pressure dependence of fluorescent and photolytic interferences in HO detection by laser-excited fluorescence. Journal of Applied Physics 51 (7), 3459-3464.

Harris, G.W., Carter, W.P.L., Winer, A.M., Pitts Jr., J.N., Platt, U., Perner, D., 1982. Observation of nitrous acid in the Los Angeles atmosphere and implications for predictions of ozone-precursor relationships. Environmental Science and Technology 16, 414-419.

Heland, J., Kleffmann, J., Kurtenbach, R., Wiesen, P., 2001. A new instrument to measure gaseous nitrous acid (HONO) in the atmosphere. Environmental Science and Technology*, 35*, 3207-3212.

Hellebust, S., Roddis, T., Sodeau, J.R., 2007. Potential role of the nitroacidium ion on HONO emissions from the snowpack. The Journal of Physical Chemistry A *111,* 1167-1171.

Helmig, D., Johnson, B., Oltmans, S. J., Neff, W., Eisele, F., Davis, D. D., 2007. Elevated Ozone in the Boundary-Layer at South Pole, Atmospheric Environment, in press.

Herrmann, H., Buxton, G., Salmon, A., Mirabel, P., George, C., Lelieveld, J., Denteneer, F., 2000. Model development for tropospheric aerosol and cloud chemistry (MODAC), Final report, No. ENV4-CT97-0388.

Honrath, R.E., Peterson, M.C., Guo, S., Dibb, J.E., Shepson, P.B., Campbell, B., 1999. Evidence of NO_x production within or upon ice particles in the Greenland snow pack. Geophysical Research Letters 26, 695-698.

Honrath, R.E., Peterson, M.C., Dziobak, M.P., Dibb, J.E., Arsenault, M.A., Green, S.A., 2000a. Release of NO_x from sunlight-irradiated midlatitude snow. Geophysical Research Letters, 27 (15), 2237-2240.

Honrath R.E., Guo, S., Peterson, M.C., Dziobak, M.P., Dibb, J.E., Arsenault, M.A., 2000b. Photochemical production of gas-phase NO_x from ice-crystal NO_3^-. Journal of Geophysical Research 105, 24183-24186.

Honrath, R.E., Lu, Y., Peterson, M.C., Dibb, J.E., Arsenault, M.A., Cullen, N.J., Steffen, K., 2002. Vertical fluxes of NO_x , HONO, and HNO_3 above the snowpack at Summit, Greenland. Atmospheric Environment, 36 (15-16), 2629-2640.

Houdier, S., Perrier, S., Domine, F., Grannas, A., Guimbaud, C., Shepson, P.B., Boudries, H., Bottenheim, J.W., 2002. Acetaldehyde and acetone in the snow pack near Alert during Polar Sunrise Experiment 2000. Snowpack composition, incorporation processes, and atmospheric impact. Atmospheric Environment 36, 2609-2618.

Hutterli, M.A., Rothlisberger, R., Bales, R.C., 1999. Atmosphere-to-snow-to-firn transfer studies of HCHO at Summit, Greenland. Geophysical Research Letters 26. 1691-1694.

Ianniello, A., Beine, H.J., Landis, M.S., Stevens, R.K., Esposito, G., Amoroso, A., Allegrini, I., 2007. Comparing field performances of denuder techniques in the high Arctic. Atmospheric Environment 41, 1604–1615.

Jacob, D.J., 2003. The oxidizing power of the atmosphere. Chapter of the Handbook of Weather, Climate and Water: Atmospheric Chemistry, Hydrology, and Societal Impacts. Potter, T.D., Colman, B.R., Mc-Graw Hill.

Jenkin, M.I., Cox, R.A., Williams, D.J., 1988. Laboratory study of the kinetics of formation of nitrous acid from the thermal reaction of nitrogen dioxide and water vapor. Atmospheric Environment 22, 487-498.

Johnston, H.S., Graham, R.S., 1974. Photochemistry of NO_x and HO_x compounds. Canadian Journal of Chemistry 52, 1415-1423.

Joseph, J. H.; Wiscombe, W. J.; Weinman, J. A., 1976. Delta-Eddington approximation for radiative flux-transfer. Journal of the Atmospheric Sciences 33 (12), 2452-2459.

Kagann, R.H., Maki, A.G., 1983. Infrared absorption intensities of nitrous acid (HONO) fundamental bands. Journal of Quantitative Spectroscopy & Radiative Transfer 30 (1), 37-44.

Kanda, Y., Taira, M., 1990. Chemiluminescent method for continuous monitoring of nitrous acid in ambient air. Analytical Chemistry 62, 2084-2087.

Kaspers, K.A., W. van de Wal., R.S., R. van den Broeke, M., Schwander, J., M. van Lipzig, N.P., Brenninkmeijer, C.A.M., 2004. Model Calculations of the age of firn air across the Antarctic continent. Atmospheric Chemistry and Physics 4, 1365-1380.

Kirchstetter, T.W., Harley, R.A., Littlejohn, D., 1996. Measurement of nitrous acid in motor vehicle exhaust. Environmental Science and Technology 30, 2843-2849.

Klaning, U. K., Sehested, K. and Wolff, T., 1984. Ozone formation in laser flash photolysis of oxoacids and oxoanions of Chlorine and bromine. Journal of the Chemical Society Faraday Transactions 80, 2969-2979.

Kleffmann, J., Gavriloaiei, T., Hofzumahaus, A., Holland, F., Koppmann, R., Rupp, L., Schlosser, E., Siese, M., Wahner, A., 2005. Daytime formation of nitrous acid: a major source of OH radicals in a forest. Geophysical Research Letters 32, L05818, (doi:10.1029/2005GL022524).

Kleffmann, J., Lorzer, J.C., Wiesen, P., Kern, C., Trick, S., Volkamer, R., Rodenas, M., Wirtz, K., 2006. Intercomparison of the DOAS and LOPAP techniques for the detection of nitrous acid (HONO). Atmospheric Environment 40, 3640–3652.

Lammel, G., Cape, J.N., 1996. Nitrous acid and nitrite in the atmosphere. Chemical Society Reviews 25, 361-369.

Lee, E., Kim, J., Kim, K., Yoo, S., 2001. The observation of gas contaminants within cleanroom using condensing denuder type gas monitoring system. World Clean Air & Environment Congress and Exhibition, 12th, Seoul, Republic of Korea, pp.1364-1367. Air & Waste Management Association, Pittsburgh, Pa.

Lee-Taylor, J.; Madronich, S., 2002. Calculation of actinic fluxes with a coupled atmosphere-snow radiative transfer model. Journal of Geophysical Research-Atmospheres 107, (D24), 4796, (doi:10.1029/2002JD002084).

Li, S.M., 1994. Equilibrium of particle nitrite with gas phase HONO: Tropospheric measurements in the high Arctic during polar sunrise. Journal of Geophysical Research 99, 25469-78.

Liao, W., Hecobian, A., Mastromarino, J., Tan, D., 2006a. Development of a photo-fragmentation/laser-induced fluorescence measurement of atmospheric nitrous acid (HONO). Atmospheric Environment, 40 (1), 17-26.

Liao, W., Case, A. T., Mastromarino, J., Tan, D., Dibb, J.E., 2006b. Observations of HONO by laser-induced fluorescence at the South Pole during ANTCI 2003. Geophysical Research Letters, 33, L09810, doi:10.1029/2005GL025470.

Madronich, S., Flocke, S., 1998. The role of solar radiation in atmospheric chemistry. In: Boule, P. (Ed.), Handbook of Environmental Chemistry. Springer, Heidelberg, pp. 1-26.

Masafumi, T., Yukio, K., 1990. Continuous generation system for low-concentration gaseous nitrous acid. Analytical Chemistry 62, 630-633.

McConnell, J.R., Bales, R.C., Stewart, R.W., Thompson., A.M., Albert, M.R., and Ramos., R., 1998. Physically based modeling of atmosphere-to-snow-to-firn transfer of H_2O_2 at South Pole. Journal of Geophysical Research 103, D9, 10561-10570.

McDermid, I.S., Laudenslager, J.B., 1982. Radiative lifetimes and quenching rate coefficients for directly excited rotational levels of OH ($A^2\sum^+$, v'=0). The Journal of Chemical Physics 76, 1824-1831.

Michalowski, B. A., Francisco, J. S., Li, S. M., Barrie, L. A., Bottenheim, J. W., Shepson, P. B., 2000. A computer model study of multiphase chemistry in the Arctic boundary layer during polar sunrise. Journal of Geophysical Research-Atmospheres 105(D12), 15131-15145.

Neuweiler I., Attinger, S., Kinzelbach, W., 2001. Macrodispersion in a radially diverging flow field with finite Peclet numbers 1. Perturbation theory approach. Water Resources Research, 37, 2, 481-493.

Ning, C.L., Pfab, J., 1997. Generation and 355 nm laser photodissociation of nitrous acid (HONO) and HONO water clusters. The Journal of Physical Chemistry A 101, 6008-6014.

Pagsberg, P., Bjergbakke, E., Ratajczak E., Sillesen, A., 1997. Kinetics of the gas phase reaction OH + NO(+M)→HONO(+M) and the determination of the UV absorption cross sections of HONO. Chemical Physics Letters 272, 383-390.

Park, J.Y. and Lee, Y. N., 1988. Solubility and decomposition kinetics of nitrous acid in aqueous solution. Journal of Physical Chemistry 92, 6294-6302.

Perovich, D.K., Govoni, J.W., 1991. Absorption coefficients of ice from 250 to 400 nm. Geophysical Research Letters 18, 1233-1235.

Perrino, C., De Santis, F., Febo, A., 1990. Criteria for the choice of a denuder sampling technique devoted to the measurement of atmospheric nitrous and nitric acids. Atmospheric Environment 24A, 617–626.

Pitts Jr., J.N., Bierman, H.W., Atkinson, A., Winer, A.M., 1994. Atmospheric implications of simultaneous nighttime measurements of NO_3 radicals and HONO. Geophysical Research Letters 11, 557-560.

Platt, U., 1994. Differential optical absorption spectroscopy (DOAS). Air Monitoring by Spectroscopic Techniques, M. W. Sigrist, (Ed.), pp. 27-84. Wiley, New York.

Poruthoor, S.K., Dasgupta, P.K., 1995. Continuous automated measurement of gaseous nitrous and nitric acids and particulate nitrite and nitrate. Environmental Science and Technology 29 (6), 1534-15341.

Prather, M., Derwent, R., Ehhalt, D., Fraser, P., Sanhueza, E., Zhou, X., 1996. Climate change 1995 in the science of climate change, contribution of working group I to the second assessment report of the intergovernmental panel on climate change; Houghton, J. T., Meira Fiho, L. G., Callander, B. A., Harris, N., Guttenberg, A., Maskell, K., Eds, pp. 86-103. Cambridge University Press: New York.

Ramazan, K.A., Syomin, D., Finlayson-Pitts, B.J., 2004. The photochemical production of HONO during the heterogeneous hydrolysis of NO_2. Physical Chemistry Chemical Physics 6, 3836-3843.

Rasmussen, T.R., Brauer, M., Kjærgaard, S., 1995. Effects of nitrous acid exposure on human mucous membranes. American Journal of Respiratory and Critical Care Medicine 151, 1504-1511.

Reisinger, A.R., 2000. Observations of HNO_2 in the polluted winter atmosphere: possible heterogeneous production on aerosols. Atmospheric Environment 34, 3865-3874.

Rettich, T.R., 1978. Some photochemical reactions of aqueous nitric acid. Dissertation Abstracts International 38, 5968.

Riordan, E., Minogue, N., Healy, D., O'Driscoll, P., Sodeau, J. R. ,2005. Spectroscopic and optimization modeling study of nitrous acid in aqueous solution. Journal of Physical Chemistry A, 109, 779-786.

Robinson, D.A., Dewey, K.F., Heim, P.R., 1993. Global snow cover monitoring: An update. Bulletin of American Meteorological Society 74, 1689-1696.

Rodgers, M.O., 1986. Development and application of a photofragmentation/laser-induced fluorescence detection system for atmospheric nitrous acid. Ph.D. thesis, Georgia Institute of Technology.

Sander, S.P., Friedl, R.R., Ravishankara, A.R., Golden, D.M., Kolb, C.E., Kurylo, M.J., Molina, M.J., Moortgat, G.K., Keller-Rudek, H., Finlayson-Pitts, B.J., Wine, P.H., Huie, R.E., Orkin, V.L., 2006. Chemical kinetics and photochemical data for use in atmospheric studies. JPL Publication L06-2.

Schilling, R. J., Harris, S.L., 2004. Applied Numerical Methods for Engineers using Matlab and C. pp. 398-340, China Machine Press, Beijing.

Schwartz, S. E., 1986. Mass transport considerations pertinent to aqueous phase reactions of gases in liquid water clouds, in W. Jaeschke (ed.). Chemistry of Multiphase Atmospheric Systems, NATO ASI Series, Vol. 6, Springer, Berlin, pp. 415-471.

Sehested, K., Holcman, J. and Hart, E.J., 1983. Rate constants and products of the reactions e_{aq}^-, O_2^- and H with ozone in aqueous solution. Journal of Physical Chemistry 87, 1951-1954.

Sehested, K., Holcman, J., Bjergbakke, E. and Hart, E.J., 1984. A pulse radiolytic study of the reaction of $OH + O_3$ in aqueous medium. Journal of Physical Chemistry 88, 4144-4147.

Shan, J.H., Wategaonkar, S.J., Vasudev, R., 1989. Vibrational state-dependence of HONO's Ã state lifetime. Chemical Physics Letters 158, 317-320.

Shan, J.H., Wategaonkar, S.J., Vasudev, R., 1989. State-selected dissociation of cis HONO ($\tilde{A}\ ^1A''$): effect of intramolecular hydrogen bonding. Chemical Physics Letters 160, 614-617.

Shimizu H. 1970. *A*ir Permeability of Deposited Snow. Institute of Low Temperature Science: Sapporo, Japan: Contribution No. 1053. English Translation.

Spindler, G., Hesper, J., Bruggemann, E., Dubois, R., Muller, Th., Herrmann, H., 2003. Wet annular denuder measurements of nitrous acid: laboratory study of the artifact reaction of NO_2 with S(IV) in aqueous solution and comparison with field measurements. Atmospheric Environment 37(19), 2643-2662.

Sportisse, B., Djouad, R., 2000. Some aspects of multi-time scale issues for the numerical modeling of atmospheric chemistry. Atmospheric Modeling. Series: The IMA Volumes in Mathematics and its Applications, Vol. 130. pp. 39-59. Springer, New York.

Steffens., K., Crosley., D.R., 2000. Vibrational energy transfer in OH $A^2\sum^+$ between 195 and 295K. The Journal of Chemical Physics 112 (21), 9427-9432.

Stemmler., K., Ammann., M., Donders., C., Kleffmann., J., George., C., 2006. Photosensitized reduction of nitrogen dioxide on humic acid as a source of nitrous acid. Nature 440, 195-198.

Stockwell, W.R., Calvert, J.G., 1978. The near ultraviolet absorption spectrum of gaseous HONO and N_2O_3. Journal of Photochemistry 8, 193-203.

Strehlow, H. and Wagner, I., 1982. Flash photolysis in aqueous nitrite solutions. Zeitschrift Fur Physikalische Chemie-Wiesbaden 132, 151-160.

Stutz, J., Alicke, B., Neftel, A., 2002. Nitrous acid formation in the urban atmosphere: Gradient measurements of NO_2 and HONO over grass in Milan, Italy. Journal of Geophysical Research, 107 (D22), (doi:10.1029/2001JD000390).

Svensson, R., Ljungström, E., Lindqvist, O., 1987. Kinetics of the reaction between nitrogen dioxide and water vapor. Atmospheric Environment 21, 1529-1539.

Tanner, D.J., A. Jefferson, and F.L. Eisele (1997), Selected ion chemical ionization mass spectrometric measurement of OH. Journal of Geophysical Research 102, 6415-6425.

Takenaka, N., Uede A., Maeda., Y., 1992. Acceleration of the rate of nitrite oxidation by freezing in aqueous solution. Nature 358, 736-738.

Takenaka, N., Uede A., Daimon, T., Bandow, H., Dohmaru, T., Maeda, Y., 1996. Acceleration mechanism of chemical reaction by freezing: The reaction of nitrous acid with dissolved oxygen. Journal of Physical Chemistry 100, 13874-13884.

Toon, O. B.; Mckay, C. P.; Ackerman, T. P.; Santhanam, K., 1989. Rapid calculation of radiative heating rates and photodissociation rates in inhomogeneous multiple-scattering atmospheres. Journal of Geophysical Research-Atmospheres**,** 94, (D13), 16287-16301.

Toyota, K., McConnell, J. C., 2005. One-dimensional modeling of air-snowpack interactions and bromine activation in the springtime Arctic air, oral presentation at 2005 AGU Fall Meeting, San Francisco, CA, USA, 5-9 December, 2005.

Trick, S., 2004. Formation of nitrous acid on urban surfaces-a physical-chemical perspective. Ph. D thesis, Ruperto Carola University.

Tuazon, E.C., Winer, A.M., Braham, R.A., Pitts, J.N., Jr., 1980. Atmospheric measurements of trace pollutants by kilometer pathlength FTIR spectroscopy. Advanced Environmental Science & Technology, pp. 260-300. Wiley, New York.

Vasudev, R., Zare, R.N., Dixon, R.N., 1983. Dynamics of photodissociation of HONO at 369nm: motional anisotropy and internal state distribution of the OH fragment. Chemical Physics Letters 96, 399-402.

Vasudev, R., Zare, R.N., Dixon, R.N., 1984. State-selected photodissociation dynamics: complete characterization of the OH fragment ejected by the HONO Ã state. The Journal of Chemical Physics 80, 4863-4878.

Waddington, E.D., Cunningham, J., Harder, S.L., 1996. The effects of snow ventilation on chemical concentrations, In Wolff, E.W. and R.C. Bales (Ed.). Chemical Exchange Between the Atmosphere and Polar Snow, NATO ASI Series I, "Global Environmental Change" Vol. 43, Springer Verlag, Berlin, 403-451.

Wagner, I., Strehlow, H. and Busse, G., 1980. Flash photolysis of nitrate ions in aqueous solution. Zeitschrift Fur Physikalische Chemie-Wiesbaden 123, 1-33.

Waldner, P. A., Schneebeli., M., Schultze-Zimmermann, U., Fluhler, H., 2004. Effect of snow structure on water flow and solute transport. Hydrological Processes 18, 1271-1290.

Warneck, P., Wurzinger, C., 1988. Product quantum yields for the 305-nm photodecomposition of NO_3^- in aqueous-solution. Journal of Physical Chemistry 92, (22), 6278-6283.

Warren. S.G., Brandt, R.E., Hinton, R.O'R, 1998. Effect of surface roughness on bidirectional reflectance of Antarctic snow. Journal of Geophysical Research 103, 25789-25807.

Williams, J.E., Dentener, F.J., van den Berg, A. R., 2002. The influence of cloud chemistry on HO_x and NO_x in the moderately polluted marine boundary layer: a 1-D modeling study. Atmospheric Chemistry and Physics, 2, 39-54.

Winer, A. M., Biermann, H.W., 1994. Long pathlength differential optical absorption spectroscopy (DOAS) measurements of gaseous HONO, NO_2, and HCHO in the California South Coast Air Basin. Research on Chemical Intermediates 20, 423-445.

Wingen, L.M., Barney, W.S., Lakin, M.J., Brauers, T., Finlayson-Pitts, B.J., 2000. A unique method for laboratory quantification of gaseous nitrous acid (HONO) using the reaction $HONO + HCl \rightarrow ClNO + H_2O$. The Journal of Physical Chemistry A 104 (2), 329-335.

Yang, J., Honrath, R.E., Peterson, M.C., Dibb, J.E., Sumner, A.L., Shepson, P.B., Frey, M., Jacobi, H.-W., Swanson, A., Blake, N., 2002. Impact of snow pack photochemistry on HO_x levels at Summit, Greenland. Atmospheric Environment 36, 2523-2534.

Zellner, R.; Exner, M.; Herrmann, H., 1990. Absolute OH quantum yields in the laser photolysis of nitrate, nitrite and dissolved H_2O_2 at 308 and 351 nm in the temperature-range 278-353 K. Journal of Atmospheric Chemistry 10, (4), 411-425.

Zhang, G., Slanina, S., Brad Boring, C., Jongejan, P.A.C., Dasgupta, P.K., 2003. Continuous wet denuder measurements of atmospheric nitric and nitrous acids during the 1999 Atlanta Supersite. Atmospheric Environment 37 (9-10), 1351-1364.

Zhou, X., Civerolo, K., Dai, H., Huang, G., Schwab, J., Demerjian, K., 2002a. Summertime nitrous acid chemistry in the atmospheric boundary layer at a rural site in New York State. Journal of Geophysical Research 107, 4590, (doi:10.1029/2001JD001539).

Zhou, X., He, Y., Huang, G., Thornberry, T. D., Carroll, M. A., Bertman, S. B., 2002b. Photochemical production of nitrous acid on glass sample manifold surface. Geophysical Research Letters 29 (doi:10.1029/2002GL015080).

Zhou, X., Beine, H.J., Honrath, R.E., Fuentes, J.D., Simpson, W., Shepson, P.B., Bottenheim, J.W., 2001. Snow pack photochemical production of HONO: A major source of OH in the Arctic boundary layer in springtime. Geophysical Research Letters 28, 4087-4090.

Zhou, X., Qiao, H.C., Deng, G.H., Civerolo, K., 1999. A method for the measurement of atmospheric HONO based on DNPH derivatization and HPLC analysis. Environmental Science and Technology 33, 3672–3679.

VITA

Wei Liao

Wei Liao was born in Shaanxi, China. He attended Xi'an No. 1 middle school from 1992 to 1997, received a B.S. in chemistry from Peking University, Beijing in 2001 before coming to Georgia Tech to pursue a doctorate in Atmospheric Science. The topic of his thesis is the development of a laser-induced fluorescence (LIF) technique for in situ nitrous acid (HONO) measurements and air-snowpack modeling of atmospheric nitrous acid (HONO). He has two papers published in the core journals of geophysical field and two papers in manuscript. He presented four times at the American Geophysical Union annual meetings. He participated in NSF sponsored Antarctic Tropospheric Chemistry Investigation (ANTCI) in 2003 and NASA sponsored Intercontinental Chemical Transport Experiment - North America (INTEX-NA) in 2004 and 2006. In 2005 he was honored to receive the group achievement award by NASA. In the spare time, he enjoys photography, traveling and watching Georgia Tech basketball and football.